

**Chromospheric and coronal activity:  
Analysing optical spectra  
of M dwarfs**

**Dissertation  
zur Erlangung des Doktorgrades  
des Fachbereichs Physik  
der Universität Hamburg**

vorgelegt von

**Birgit Fuhrmeister**

geboren in Hamburg

**Hamburg  
2005**

Gutachter der Dissertation: Prof. J.H.M.M. Schmitt  
Prof. C.I. Short

Gutachter der Disputation: Prof. J.H.M.M. Schmitt  
Prof. P.H. Hauschildt

Datum der Disputation: 7.10.2005

Vorsitzender des Prüfungsausschusses: Dr. habil. F.-J. Zickgraf

Vorsitzender des Promotionsausschusses: Prof. G. Huber

Dekan des Fachbereichs Physik: Prof. G. Huber



# Zusammenfassung

Unter stellarer Aktivität werden eine Reihe von Phänomenen in den unterschiedlichen Atmosphärenschichten zusammengefasst, die eng mit dem Magnetfeld des einzelnen Sterns verbunden sind. Da eine direkte Auflösung der Sternoberfläche, wie uns dies bei der Sonne möglich ist, für aktive Sterne noch in ferner Zukunft liegt, können diese Phänomene im Normalfall nicht direkt beobachtet werden. Es können aber aus der Spektralanalyse indirekt Informationen über die Aktivität eines Sterns gewonnen werden.

Die vorliegende Arbeit beschäftigt sich mit koronaler und chromosphärischer Aktivität von mittleren und späten M Sternen und deren Nachweis und Analyse in UVES Echelle-Spektren von 3030 bis 3880 und 4580 bis 6680 Å.

Dabei widmet sich der erste Teil der Arbeit dem Nachweis der verbotenen koronalen Fe XIII Linie bei 3388 Å. Das mehrere Millionen Kelvin heiße koronale Gas wird normalerweise – und am leichtesten – im Röntgenbereich beobachtet. Es ist nun die Idee, solchen Röntgendaten Beobachtungen im Optischen gegenüberzustellen, um von der wesentlich besseren spektrale Auflösung, die im optischen Spektralbereich und nahen Ultravioletten erzielt werden kann, und dem Vorteil bodengebundener Beobachtungen zu profitieren. Eine Schwierigkeit dabei ist die Detektion der verbotenen Linie vor dem photosphärischen und chromosphärischen Hintergrund des Sterns. Diese Linie kann jedoch auf LHS 2076 (Spektraltyp M5.5) während eines *Flares* und auf CN Leo (M5.5) zweifelsfrei nachgewiesen werden. Des Weiteren wird die zeitliche Variabilität der Linie für CN Leo untersucht.

Der zweite Teil der Arbeit beschäftigt sich mit chromosphärischer Aktivität, die sich zum Teil in hunderterten von Emissionslinien oder Emissionskernen besonders im nahen Ultravioletten manifestiert. Diese wurden in der vorliegenden Arbeit für einen Satz von 21 M und L Zwergen identifiziert. Stärkste Linien im betrachteten Spektralbereich sind die Balmer Linien, das Na I D Dublett, die He I D<sub>3</sub> Linie und einige Fe I Linien, die in fast allen hier vorliegenden Spektren gefunden werden können. Die Emissionslinien können in Stärke, Breite und Zentralwellenlänge während eines *Flares* variieren, dabei können sie sich extrem verstärken, so dass neue Linien im Spektrum auftauchen. Ihre Stärke kann sich aber auch außerhalb von *Flares* verändern. Welche Rückschlüsse aus den zeitlichen Veränderungen der Emissionslinien gezogen werden können, wird für einen *Flare* auf dem M9 Zwerg DENIS 104814.7-395606.1 analysiert, sowie für einen langen Ausbruch auf LHS 2034 (M6), bei dem das Hauptaugenmerk auf Linienasymmetrien der Balmer Serie und der Helium Linien liegt.

Wichtige Hinweise auf die Vorgänge in der Atmosphäre des Sterns können dabei nicht nur direkt aus den Linienveränderungen gewonnen, sondern auch durch numerische Simulationen von Sternatmosphären gezogen werden. So beschäftigt sich ein wesentlicher Bestandteil des zweiten Teiles dieser Arbeit mit der Simulation von chromosphärischen Emissionslinien mit Hilfe des Sternatmosphärencodes PHOENIX, der es ermöglicht, neben dem photosphärischen Teil der Atmosphäre eine Chromosphäre mit empirisch festgelegtem Temperaturverlauf zu berechnen. Solche Modellatmosphären wurden für 5 M Zwerge außerhalb von *Flares* konstruiert. Modellrechnungen für LHS 2034 während des beobachteten *Flares* ergeben relativ hohe Füllfaktoren. Für alle diese Modelle wurde ein starker Einfluß von NLTE Rechnungen auf die Linienstärke festgestellt. Falls man Sauerstoff, Stickstoff und Schwefel im LTE berechnet wird verglichen mit NLTE Rechnungen sogar die Stärke der Wasserstofflinien beeinflusst. Da diese Elemente starke Linien im Lyman Kontinuum haben, wird die Ionisationsbalance von Wasserstoff beeinflusst, falls die Stärke dieser Linien durch LTE Rechnungen überschätzt wird.

---

# Abstract

The term “stellar activity” describes a collection of transient phenomena in the outer layers of the stellar atmosphere, which are strongly connected to the star’s magnetic field. In contrast to the Sun, where observations of high spatial resolution exist, we will not be able to directly resolve the surface of active stars in the near future. Therefore an analysis of the spectroscopic features of these stars is the only method available to gain information about their activity phenomena.

The present thesis deals with the chromospheric and coronal activity of mid- to late-type M dwarfs and some early L dwarfs. It is based on UVES echelle spectra in the wavelength range from 3030 to 3880 and 4580 to 6680 Å.

The first part of this thesis is dedicated to coronal activity, specifically to the forbidden coronal Fe XIII line at 3388 Å. The up to several million Kelvin hot gas of stellar coronae is normally – and easiest – observed at X-ray wavelengths. The idea is to contrast the X-ray data with optical observations, which have the advantage of much better wavelength resolution in the optical and near UV, and the possibility of ground-based observations. One difficulty for the detection of the Fe XIII line lies in the relatively high photospheric and chromospheric background flux in the respective wavelength range. Nevertheless, a detection was possible for LHS 2076 (M5.5) during a short duration flare and for CN Leo (M5.5) that exhibited the line permanently but with some variability.

The second part of the thesis addresses chromospheric activity. Chromospheres of M dwarfs can exhibit hundreds of emission lines and emission cores in absorption lines especially in the near UV. These lines have been identified in the course of this work for 21 M and L dwarfs. The strongest lines belong to transitions of the Balmer series, the Na I D doublet, He I D<sub>3</sub>, and Fe I, which show up in nearly all stars of the sample. The chromospheric lines can vary with time even in quiescent state. During flares their FWHM and central wavelength can change and the lines normally become much stronger; even many new emission lines can occur. The chromospheric line activity is analysed for a flare on the old M9 dwarf DENIS 104814.7-395606.1 as well as for a long duration flare on LHS 2034 (M6), where the main focus lies on large red wing asymmetries of the Balmer and Helium lines.

Besides interpreting line variations directly, valuable information can be gained via the construction of semi-empirical model atmospheres. Therefore an essential constituent of the second part of this thesis deals with the simulation of chromospheres using the stellar atmosphere code PHOENIX. The models consist of a photosphere in radiative equilibrium, a chromosphere and part of the transition region with a given temperature rise versus column mass. Chromospheric models were constructed to fit the observed quiescent spectra of 5 M dwarfs, covering a substantial part of the M dwarf regime. Additionally, a grid of models was computed for the flaring state of LHS 2034, indicating a rather high filling factor. For all models a strong influence of NLTE calculations on the line formation and a lot of crosstalk between different NLTE species have been found. If oxygen, nitrogen and sulfur are computed in LTE, the strength of the hydrogen lines is altered compared to NLTE computations. Many strong lines of these elements are located in the Lyman continuum and therefore can change the ionisation balance of hydrogen, if the strength of these lines is overpredicted due to LTE calculations.



# Contents

<b>1</b>	<b>Introduction</b>	<b>1</b>
1.1	Stellar Activity . . . . .	1
1.1.1	M dwarfs and their activity . . . . .	2
1.1.2	Magnetic field generation . . . . .	4
1.1.3	Chromospheres . . . . .	6
1.1.4	Coronae . . . . .	9
1.2	The stellar atmosphere code PHOENIX . . . . .	10
1.2.1	Line formation and different approximations . . . . .	11
1.3	Outline . . . . .	13
<b>2</b>	<b>Fe XIII coronal line emission in cool M dwarfs</b>	<b>17</b>
<b>3</b>	<b>Analysis of a huge flare on DENIS 104814.7-395606.1</b>	<b>33</b>
<b>4</b>	<b>Modeling M-dwarf chromospheres with PHOENIX</b>	<b>43</b>
<b>5</b>	<b>Detection of red line asymmetries in LHS 2034</b>	<b>47</b>
<b>6</b>	<b>PHOENIX model chromospheres of mid- to late-type M dwarfs</b>	<b>59</b>
<b>7</b>	<b>Influence of NLTE calculation on the hydrogen lines</b>	<b>75</b>
<b>8</b>	<b>Summary and outlook</b>	<b>85</b>
8.1	Summary . . . . .	85
8.2	Outlook . . . . .	86
<b>A</b>	<b>How to compute a PHOENIX chromosphere</b>	<b>89</b>
A.1	Starting with a photosphere . . . . .	89
A.2	Attaching the chromospheric temperature rise . . . . .	90
A.3	Model iteration . . . . .	91
A.4	Output of various radiative transfer variables . . . . .	92
	<b>Acknowledgements</b>	<b>93</b>



# Chapter 1

## Introduction

### 1.1 Stellar Activity

Stellar activity is the collective term for the zoo of transient phenomena present in the atmospheres of stars, such like *spots*, *flares*, *prominences*, *mottles*, *spiculae*, etc.. Many of these structures like *mottles* and *spiculae* are only known from the Sun – a rather inactive star, but due to its vicinity the best studied case. The names are historically grown, e. g. filaments and prominences are the same phenomena, seen on the Sun's disc and on the limb, respectively. Though astronomers have learned a lot about activity in the recent years, the details of the activity driving mechanisms are still not well understood.

One thing in common for all the activity phenomena is the connection to the magnetic field of the star which in turn is strongly connected to convection. Therefore, activity can be found only in stars with outer convection zones, which are referred to as late-type stars. In the Hertzsprung-Russell diagram (see Fig. 1.1) these stars are indicated as F, G, K, and M stars with respect to their effective temperature. M dwarfs are located at the very cool end of the main sequence. Objects of even lower effective temperature than M stars are called L and T dwarfs. Though the early L subtypes may be very low mass stars, later subtypes of L and T dwarfs are brown dwarfs, which are only capable of deuterium burning. Also individual objects among the late subtypes of the M dwarfs (very late-type M dwarfs) may fall into the brown dwarf regime depending on the age of the object. Activity is also found for objects at this hydrogen burning border and (seldom) beyond.

The level of activity depends on the age and rotational velocity of the star and for many stars

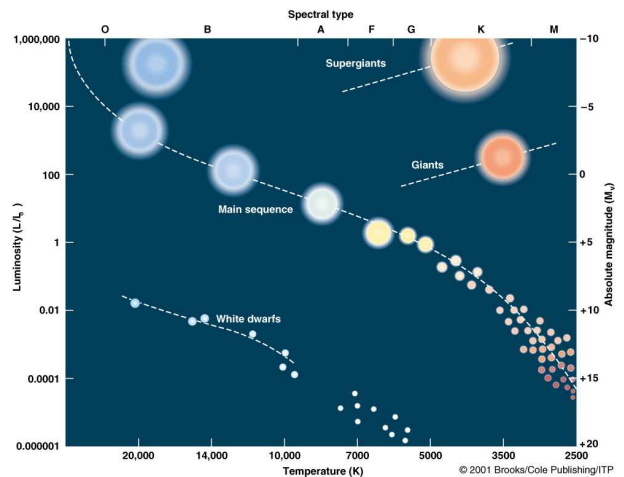


Figure 1.1: The Hertzsprung-Russell diagram. The M dwarfs can be found at the cool end of the main sequence. As is indicated in the diagram they are the most numerous type of stars. L and T dwarfs are not indicated in this diagram. Taken from Hartmann & Impey (1994).

varies during a magnetic cycle. Therefore, many different activity levels can be studied in different stars, which can be compared to the activity of the Sun, and may help to better understand the activity driving mechanisms. Also, this allows us to study indirectly the activity level of the Sun in the past. Since the solar activity seems to influence the Earth's climate, this is not only of astrophysical interest. High energy particles ejected by the Sun during flares and the strength of the solar wind are thought to have an impact on the heating or cooling of the Earth's atmosphere. One theory involves the galactic cosmic ray flux, which varies inversely with solar activity and modulates

the Earth's cloud cover. If clouds cool or heat the Earth's atmosphere depends on the clouds altitude, the droplet size and other factors, but high clouds are thought to tend to heat, while low clouds tend to cool. Recently a correlation between cosmic ray flux and the global coverage with low clouds have been found. This would imply less low clouds during times of high solar activity and thus less cooling, but since the physical mechanism linking the cosmic ray flux to cloud production is not yet understood this theory is still very controversial (Marsh & Svensmark 2003). Accordingly there is an ongoing debate, whether the increase in solar activity, which is observed for the last decades, contributes to the global warming, and if so, how large the influence is (Friis-Christensen & Lassen 1991). Historically, there is a striking agreement between phases of enhanced magnetic activity of the Sun and warmer periods on Earth. For example, the warm period from 1000 to 1300 AC, during which the Vikings settled in Greenland, coincides with enhanced solar activity traced by the production rate of C14. Furthermore, the so called "little ice age" in Europe roughly coincides with the Maunder Minimum. During the Maunder Minimum, lasting from 1645 to 1715, Sunspot activity was absent or strongly suppressed (Eddy 1976).

Besides studying solar-like stars more extreme cases of activity found among M dwarfs can help to test the current theories of activity driving mechanisms. Comprehending extreme cases helps to ascertain whether the underlying physics of a certain phenomenon is really understood. Therefore, understanding the most active M dwarfs will after all lead to a better understanding of the activity of the Sun.

This thesis deals with the chromospheric and coronal activity in M dwarfs with known high activity levels. This introductory chapter gives a short overview about M dwarfs, their activity, its possible driving mechanisms and the computation of stellar model atmospheres, which help to interpret the available data.

### 1.1.1 M dwarfs and their activity

M dwarfs dominate the number density of stars in the Galaxy and they generally tend to be rather active, which can be shown from several activity

tracers. These belong to different parts of the atmosphere of the star, the photosphere, the chromosphere and the corona. The photosphere is the region, where most of the visible light originates. For the Sun it is the surface we can see in white light. The chromosphere and corona are outer parts of the stellar atmosphere and will be explained in more detail in sections 1.1.3 and 1.1.4.

#### Photospheric activity

One photospheric activity tracer is the number of dark spots on the stars surface. Though spots can be detected on other stars than the Sun for example by periodic brightness variations and Doppler imaging, the theory of spot forming mechanisms relies heavily on highly spatially resolved observations of the Sun. However, for more active stars, spot configurations like polar spots are possible, which are never observed for the Sun.

Spots occur where magnetic flux tubes break through the photosphere. The strong magnetic fields severely hamper the underlying convection by preventing the overturning motion. This results in a lower energy input, in a lower temperature and accordingly in lower luminosity. Modern spot models favour a description with a bundle of thin flux tubes over one large flux tube. Since in addition to the temperature the density is reduced in the flux tube compared to the surroundings also the opacity is reduced and we see to deeper geometrical depths (the so called Wilson depression).

#### Chromospheric activity

Chromospheric activity is traditionally measured using the  $H_{\alpha}$  emission of the star. For M dwarfs the  $H_{\alpha}$  line is seen either in strong absorption (dM) or in emission (dMe). An example of both cases is shown in Fig. 1.2. Both indicate chromospheric activity (Giampapa & Liebert 1986), since the photospheres of M dwarfs are too cool to significantly populate the  $n=2$  level of hydrogen. This implies that M dwarfs without a chromosphere would exhibit only a very weak  $H_{\alpha}$  line. M dwarfs with weak chromospheres start to increase the population of the  $n=2$  level of hydrogen and the line goes into absorption, since it is still photoionisation dominated by the photosphere. Increasing activity

first deepens this absorption line; a further increase of activity drives the line into emission, though. This is explained by the increasing electron density, causing the line to become collisionally controlled. As all the stars in the sample considered here are very active, they all exhibit the  $H_\alpha$  line in emission. Chromospheric model calculations are capable of reproducing this trend with strong  $H_\alpha$  absorption for weak chromospheres, and  $H_\alpha$  emission for strong chromospheres. Stronger chromospheres are characterised by their location at larger depth in the atmosphere and accordingly an onset of the transition region at higher pressure (e. g. Andretta et al. 1997; Cram & Mullan 1979). The fraction of M dwarfs showing  $H_\alpha$  in emission increases with later spectral type and reaches 100 % at spectral type about M7 (Gizis et al. 2000).

Other tracers of chromospheric activity are for example the Ca II H and K line and other emission lines in the optical and ultraviolet. Since M dwarfs have effective temperatures between about 4000 and 2000 K, their black body emission peaks in the red and infrared. Therefore, their photospheric emission is already rather faint in the blue part of the spectrum and hundreds of prominent chromospheric emission lines are found especially at the blue end of the optical band. Also many ultraviolet lines are due to chromospheric or transition region emission. These emission lines can be used for tracing activity, inferring a temperature structure and learning about possible heating mechanisms. Besides changes in line flux or central wavelength, also the line shape yields information; for example many transition region lines in the far ultraviolet (FUV) show a broad asymmetric component, which is interpreted as evidence for micro-flare heating (Pagano et al. 2000). Since M dwarfs are intrinsically rather faint and even fainter at blue wavelength, high resolution spectroscopy is only possible using large telescopes. This is the only possibility to gain information about the chromospheres of M dwarfs, though. Since M dwarfs have radii between about 0.5 and 0.1  $R_\odot$ , we will not be able to resolve the surface of any M dwarf in the near future. Direct spatially resolved observations of their chromospheres as for the Sun are therefore not possible.

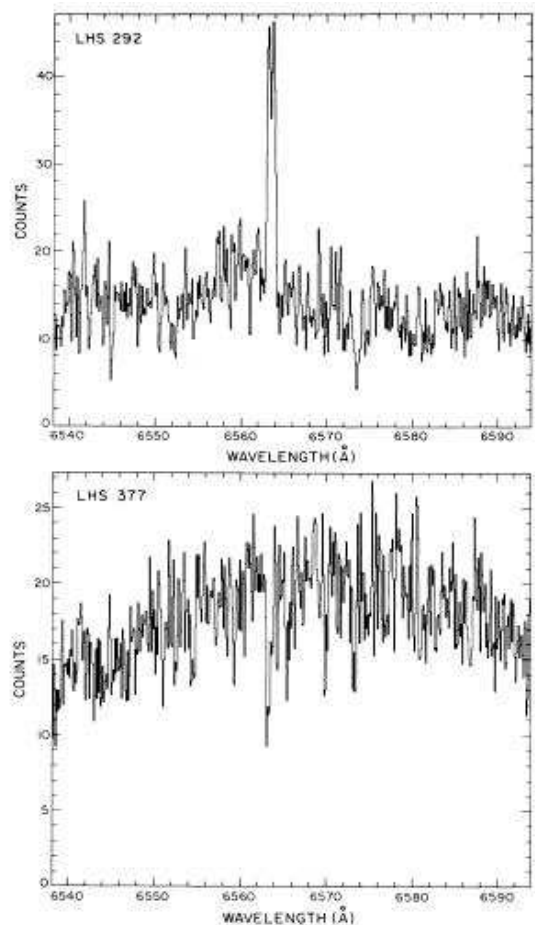


Figure 1.2: Example of the  $H_\alpha$  line in M dwarfs. While LHS 292 shows the  $H_\alpha$  line in emission, LHS 377 shows it in absorption. Taken from Giampapa & Liebert (1986).

### Coronal activity

Coronal activity tracers are the ratio of X-ray luminosity to bolometric luminosity and the flare frequency. The flare frequencies of M dwarfs are much higher compared to the Sun. While large flares with X-ray flux increases of a factor 10 and more are rare, flares with intermediate flux increases of factor 2 to 3 can be found on a timescale of a few hours for the most active M dwarfs (Robrade & Schmitt 2005). It has been proposed, that the small X-ray flux changes found on timescales on minutes are a superposition of a large number of small flares with a power law distribution (Güdel et al. 2003). If the number of small flares is large enough they can contribute a significant amount of

coronal heating. A micro flare heating mechanism for the corona is also discussed for the Sun.

Moreover, flares on M dwarfs can easily be 100 times more energetic than on the Sun and they can last for days, while long duration flares on the Sun last only for some hours. During such flares M dwarfs can exhibit coronal plasma with temperatures of 15 to 60 million Kelvin (MK), and even during quiescent state their coronal plasma is about 6 to 7 million Kelvin hot (Robrade & Schmitt 2005). On the Sun, plasma temperatures in the corona are normally 1 to 2 MK. Since under normal coronal conditions magnetic field and plasma are co-moving, the complex loop structure of the magnetic field can be revealed directly by observations of high spatial resolution. Such observations are carried out by the SOHO and TRACE satellites for the Sun.

For M dwarfs many flares can also be observed at optical wavelength in emission lines and in the continuum. The latter are called white light flares and are rare for the Sun.

### The stellar boundary

M dwarf masses range from about 0.5 to 0.08 solar masses at the sub-stellar boundary. In the very late-type M dwarf regime stars as well as brown dwarfs can be found. Since sub-stellar objects are brightest when they are born, the brown dwarfs must be younger than the stars with the same spectral type. There are indications that the activity of these objects is related primarily to the temperature and only secondary to mass and age and that the lower temperature objects have weaker chromospheres. Thus a strong  $H_\alpha$  late-type emitter in the field is more likely to be older and have higher temperature than to be younger and sub-stellar (Gizis et al. 2000).

The activity of M9 dwarfs and later seems to drop drastically despite the high observed rotational velocities in these objects (Mohanty & Basri 2003). This can be seen in the declining ratio of the  $H_\alpha$  to bolometric luminosity as well as in the increasing number of objects with no  $H_\alpha$  emission line at all. Furthermore, these objects seem to spend fewer time in flaring state (Gizis et al. 2000). Therefore the activity-rotation relation known from solar type stars as well as the activity-age relation

seems to break down with sub-stellar objects. One possible cause for reduced chromospheric activity may be the high resistivity of the cool mostly neutral atmospheres of these objects (Mohanty & Basri 2003). Nevertheless, there are reports of few very late-type objects with high persistent activity levels. Examples of these puzzling class of objects are 2MASS J1315309-264951, PC 0025+0447, and 2MASS J1237392+652615. Moreover, even objects without a detectable level of quiescent activity can exhibit transient activity events. Accordingly, there are numerous reports of detections of  $H_\alpha$  flare events even down to the L and T dwarf regime (e. g. Liebert et al. 2003; Burgasser et al. 2002).

There are also detections of X-ray emitting brown dwarfs, out of which very few seem to exhibit persistent emission. For the Pleiades the first detection could be achieved by Briggs & Pye (2004). For the older brown dwarf Gl 569Bab non-variable emission could be detected by Stelzer (2004), but this emission may be connected to the afterglow of a flare. However, in general the X-ray emission from ultra-cool dwarfs seem to follow the declining trend in  $H_\alpha$  emission.

As another type of activity tracer also radio emission was detected during flares and quiescence for very late-type M and L dwarfs (Berger et al. 2005). Radio emission is thought to originate as gyrosynchrotron radiation in magnetic fields, as bremsstrahlung, or in case of polarised radio bursts also by electron cyclotron masers. Burgasser & Putman (2005) carried out a radio survey for seven M and L dwarfs and found quiescent radio emission for LHS 3003 and DENIS 1048-3956, the latter exhibiting also a spectacular radio flare. Both objects are also subject to this thesis, with DENIS 1048-3956 exhibiting a strong flare in chromospheric emission lines.

On the other hand, IR variability found in brown dwarfs is normally not ascribed to activity induced spots like for more early-type stars. Instead it is ascribed to inhomogenities in dust clouds that form in the cool atmospheres of these objects (Gelino et al. 2002).

### 1.1.2 Magnetic field generation

One common driving mechanism for all activity phenomena, apart from chromospheric emission

lines in the internetwork regions, is the magnetic field of the star. Magnetic fields can also be measured directly. For example, for the M dwarfs Gl 729 and EV Lac Johns-Krull & Valenti (1996) found a magnetic field of 2600 and 3800 G, respectively and a filling factor of about 50 percent. For the Sun it is possible to measure the magnetic field spatially resolved and to determine its evolution over time. It turns out that the magnetic field changes polarity following a 22 year cycle, called the Hale cycle, since it was discovered by George Hale in 1925 (Hale & Nicholson 1925). This rules out a primordial origin of the solar magnetic field and points to a more dynamic scenario.

### The $\alpha\Omega$ -dynamo

For solar-like stars with an outer convection zone and an inner radiative zone, the standard model for generating the magnetic fields found in these stars is called the  $\alpha\Omega$ -dynamo. In a raw sketch of this scenario one starts from a weak poloidal magnetic field that may be primordial. Differential rotation winds the magnetic field lines up, creating a toroidal field (the  $\Omega$ -effect). These magnetic field lines are stored in the overshoot region below the convection zone before they are brought up through the convection zone and get twisted by the Coriolis force. In this way a poloidal field can be generated (the  $\alpha$ -effect) regenerating the initial situation but with reversed polarity. This scenario can explain the about 22 years long magnetic cycle of the Sun and was first proposed by Babcock (1961).

Magnetic flux tubes can be brought up easily through the convection zone since they experience magnetic buoyancy, as the gas pressure is lowered inside them compared to outside due to additional magnetic pressure inside the tube. If the tube is in thermal equilibrium with its surroundings, also the density is lower inside and therefore the tube will rise. Nevertheless, magnetic flux tubes can be stored in the overshoot region below the convection zone. There the temperature gradient is sub-adiabatic, i. e., when the flux tube rises adiabatically it becomes cooler than the surroundings. This effect can stabilise the flux tube, if the magnetic field along with the magnetic pressure is smaller than a certain threshold (Moreno-Inserti et al. 1992; Stix 2004).

### Dynamos in M dwarfs

M dwarfs are expected to become fully convective at about M3/M4. Therefore the  $\alpha\Omega$ -dynamo process proposed for solar like stars should be inefficient as they have no radiative core and no overshoot region where the magnetic field can be stored. However, no transition in the activity around this spectral type has ever been noticed. On the contrary, M5 to M7 dwarfs can be extraordinarily active.

Currently there are two possible explanations for this. Either the  $\alpha\Omega$ -dynamo is smoothly replaced by some other dynamo mechanism or the overshoot region at the bottom of the convection zone plays not as important a role in the  $\alpha\Omega$ -dynamo as is currently presumed. As a replacement dynamo mechanism, a turbulent dynamo is under discussion as proposed by Durney et al. (1993). The main problem with a turbulent dynamo is, though, that it produces small-scale magnetic fields which can hardly account for the high activity in M dwarfs. On the other hand, 3D magnetohydrodynamic simulations indicate that convection zones may offer a pumping mechanism that transport magnetic flux to deep layers of the convection zone where it can be stored by the same mechanism (instead of the overshoot layer) (Dorch & Nordlund 2001). A similar explanation is proposed by Schrijver & Zwaan (2000) who argue that the rising velocity of the magnetic field is so small in the high density environment in deep layers of M dwarfs that the differential rotation can act long enough to strengthen the magnetic field.

Another possibility is that the transition to fully convective stars does not occur at spectral type M3/M4. Mullan & MacDonald (2001) proposed that a magnetic field hinders the convection and thus allows stars down to  $0.1 M_{\odot}$  to sustain a radiative core. This would place the transition roughly at the end of the main sequence, where indeed indications for a general decline of activity are observed. While M dwarfs spend at least about seven percent of the time in flaring state, for L dwarfs this is only about one percent. The larger puzzle in this context, though, are the few L and T dwarfs exhibiting high persistent activity levels, giving maybe evidence of a currently unknown emission line generating mechanism (Liebert et al. 2003).

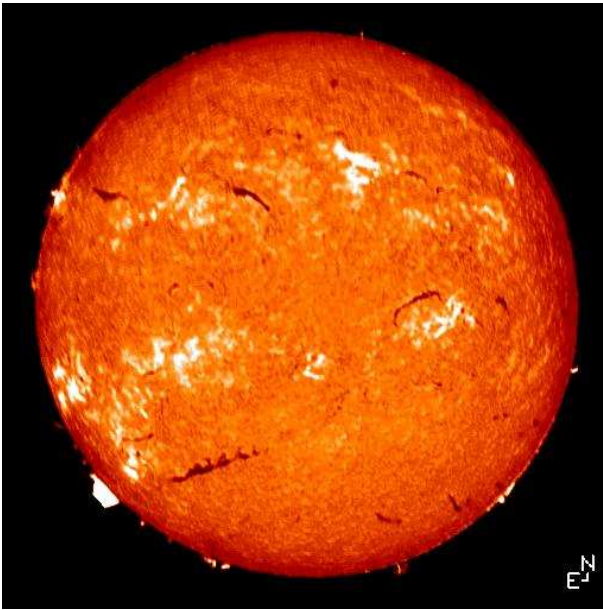


Figure 1.3: Image of the Sun's chromosphere taken in the  $H_\alpha$  line from the Kiepenheuer Institut in February 2000 (<http://www.kis.uni-freiburg.de>).

### 1.1.3 Chromospheres

The chromosphere is a thin layer between the photosphere of the star and the corona. On the Sun it is normally largely outshone by the photosphere, but can be seen for a short time during total eclipses as a reddish rim, which is the origin of its name from the Greek word  $\chi\rho\omicron\mu\omicron\varsigma$ , meaning colour. In former days total solar eclipses were the only way for chromospheric observations. Nowadays it is observed normally in chromospheric emission lines using narrow filters. This is possible, since most of the flux in the core of these lines is produced in the chromosphere and not in the photosphere. For the Sun the most prominent chromospheric lines in the optical are  $H_\alpha$  and the Ca II H and K lines.

An image of the Sun's chromosphere taken with an  $H_\alpha$  filter is shown in Fig. 1.3. Besides the limb darkening some typical chromospheric structures can be seen. On the disc there are dark filaments, which actually are the same as the prominences, which are hovering over the limb, but seen 'from above'. These structures are relatively cool clouds supported by the magnetic field above the photosphere. On the disc, also bright plages can be seen, which are a typical component of active re-

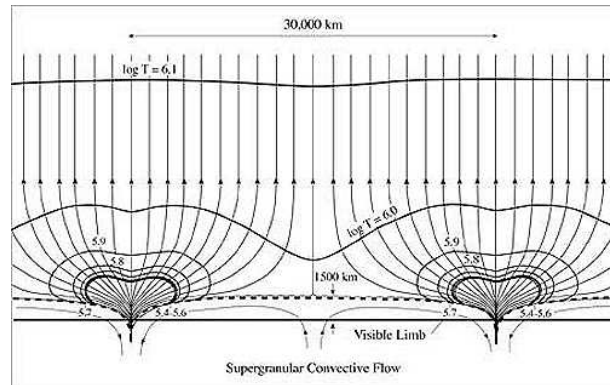


Figure 1.4: Schematic view of the transition region and the magnetic canopy, reproduced from Lang (2001).

gions and overlay the so-called faculae in the photosphere. Another chromospheric feature, which is faint in  $H_\alpha$  filter observations, but easily seen using a Ca II K filter, is the chromospheric network, that covers the whole Sun outside active regions. In Fig. 1.3 the magnetic network can be best seen in the western equatorially region. The chromospheric network coincides with the supergranular pattern found in the photosphere. These two at first glance independent features are connected via the magnetic field. The deep supergranular convection cells enhance vertical magnetic flux tubes at their rims. In fact, in the lower chromosphere the area between the network patches is nearly free of strong magnetic fields. Along the patches where the flux tubes reside there are small bright mottles found that build up the network. These bright mottles seem to be the same as the spiculae seen in limb observations. Spiculae are jets of rising gas that can rise about 10 000 kilometres above the photosphere. In the upper (internetwork) chromosphere the magnetic field spreads out horizontally which is called the magnetic canopy. A schematic illustration of the supergranules and the formation of the magnetic canopy is shown in Fig. 1.4.

Between the chromosphere and the corona an even shallower layer can be found, which is called transition region. It links the chromosphere to the at least one million Kelvin hot corona. The borders of the transition region are not well defined. The lower border can be defined at about 8000 K,

where the temperature gradient steepens dramatically or at about 20 000 K, where hydrogen is mostly ionised. The dominant heat transport mechanism in the transition region is heat conduction down from the corona. It is the only layer in the Sun's atmosphere, where heat conduction plays a major role.

### Classical semi-empirical models

In the classical chromospheric scenario the transition between photosphere and chromosphere is marked by a temperature minimum and an attached temperature rise in the chromosphere. This chromospheric layer is thought to be about 2000 km thick for the Sun. In the upper chromosphere, at about 7000 K a temperature plateau is found and from about 8000 K the temperature gradient is steepening dramatically since hydrogen is no efficient cooling agent any more.

An often cited classical chromospheric model for the average quiet Sun is the VAL C model by Vernazza et al. (1981) (see Fig. 1.5). Vernazza et al. also calculated models for distinct regions on the Sun, ranging from weak activity in the internetwork regions to higher activity in the bright network. The one-dimensional ansatz used in these models is a reasonable approximation for the internetwork regions, since the horizontal scale is much larger than the vertical (see Fig. 1.4). In the network itself that has a horizontal extension comparable to the vertical extent, this approximation should be less good.

Since the temperature is rising outwards in the chromosphere, an additional heating mechanism is required there. The basic concept for the non-magnetic chromosphere are acoustic waves. They are triggered in the convection zone and travel outwards into the thinning medium, where they are steepening into shock waves, which heat the medium. This theory has been challenged recently for the Sun by Fossum & Carlsson (2005), since observations of high frequency waves in conjunction with simulations indicate, that their energy flux is too low by a factor of at least 10 to balance the radiative losses of the solar chromosphere. While in the upper chromosphere heating may take place through magnetic energy, the heating of the lower chromosphere in the internetwork regions is totally

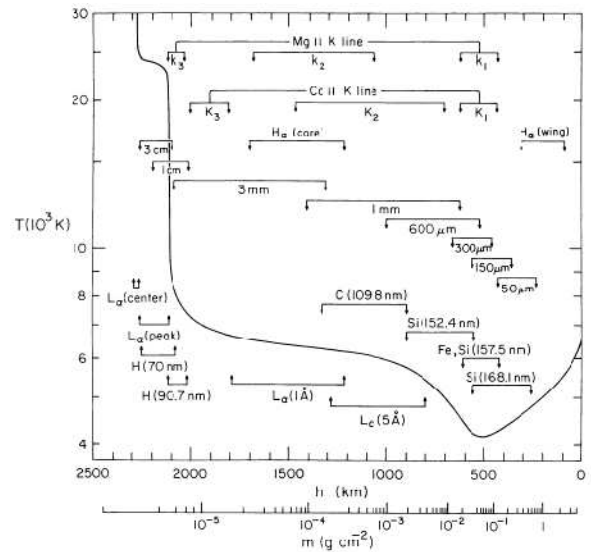


Figure 1.5: The temperature distribution for the averaged quiet Sun chromosphere as found by Vernazza et al. (1981). Indicated are also the approximate formation depths of the various lines and continua used for the derivation of the model.

puzzling if there is no significant contribution by the acoustic waves.

In the chromospheric magnetic network and above the magnetic canopy additional heating is provided by the magnetic field. Since the coronae of late-type stars are probably exclusively heated by magnetic mechanisms, these will be described in section 1.1.4.

Semi-empirical modelling can give insights into the problem independent from the particular heating mechanism. This means that atmospheric computer models are calculated with a given temperature structure, which is altered until the theoretical spectrum fits the data well. The inferred temperature structure in turn constrains the possible heating mechanisms. For the Sun semi-empirical temperature stratification models mainly based on emission lines and continuum emission, were obtained by Vernazza et al. (1981, 1976, 1973) and have been improved by Fontenla et al. (1990).

### CO in the chromosphere

One crucial assumption for the classical models is that the chromospheric medium can be described quasi-statically and that the fluctuations are small, which means it is appropriate to average spatially and over time. This approximation is problematic at least for the Sun where in limb observations CO molecules are found in the high photosphere and lower chromosphere above the classical temperature minimum (e.g. Uitenbroek et al. 1994; Ayres & Rabin 1996). The existence of CO molecules imply a gas temperature as low as about 3700 K, whereas in classical chromospheric temperature models the temperature minimum is located at about 4200 to 4400 K. Furthermore, CO-based models favour an outwardly temperature decrease in contradiction to the classical chromospheric models (Wiedemann et al. 1994). This may be explained in terms of a thermal bifurcation in the chromosphere, where hot plasma would be embedded in large-scale structures of lower temperature.

### Hydrodynamic models

Another explanation involves a more dynamic behaviour of the chromosphere. Acoustic waves are generated in the convection zone by turbulent motions and travel in all directions. Since the density in the chromosphere decreases, the outward propagating acoustic waves steepen into shock waves, which contribute to the heating of the lower chromosphere. This means that the chromosphere is a highly non-static place, with an averaged gas temperature that is not increasing with height but has transient hot episodes associated with the shockwaves (Uitenbroek 2000). In this scenario the chromosphere is not hot, but dominated by relatively cool plasma in which temporally extreme temperature peaks are embedded.

One-dimensional hydrodynamic models capable of NLTE treatment for hydrogen and calcium have been used successfully to reproduce the temporal behaviour of the calcium bright grains (Carlsson & Stein 1997). In these models the piston initiated waves steepen into shocks at about 600 km height and are separated by periods of about 3 minutes. Therefore, the models show one shock at a time and show no increase in the mean gas tem-

perature for the chromosphere (Carlsson & Stein 1995). Calcium bright grains are found in internetwork regions and are small structures that brighten for about one minute and reappear after 2-4 minutes. Observations with high temporal and spectral resolution reveal a brightening in the line wings that propagates towards the line core. Since one observes layers higher in the atmosphere closer to the line core, this behaviour can be interpreted as a source moving upwards in the atmosphere. Since the explanation of calcium bright grains involves shock waves, they seem to be places, where substantially mechanical heating takes place.

### Hydrodynamic vs. classical models

The discussion whether the non-magnetic part of the chromosphere of the Sun may be described by well stratified models with a temperature rise and only weak temperature fluctuations or by strong shocks and therefore large temperature fluctuations has been going on for years (Ayres 2002; Wilhelm & Kalkofen 2003). This already makes clear that even for the well-studied case of the Sun and the relatively well-behaved non-magnetic chromosphere the heating mechanisms are not well understood. Three-dimensional dynamical computations of the Sun's chromosphere, where the waves are initiated by convective motion are promising but presently lack a realistic radiative transport (e.g. Wedemeyer et al. 2004). And again, recent measurements indicate, that such waves may not be the dominant heating mechanism in the lower chromosphere (Fossum & Carlsson 2005).

### Chromospheric models for M dwarfs

Since we cannot resolve the surface of M dwarfs and the temporal resolution is low the approach of this thesis is to follow the classical semi-empirical concept for the Sun. Historically, early chromospheric modelling for M dwarfs with prescribed temperature structures was carried out by Cram & Mullan (1979) and Giampapa et al. (1982). The latter constructed semi-empirical chromospheres extending to temperatures of 20 000 K using the Ca II K and the H $\alpha$  line. They found that the Ca II K line is most sensitive to the amount of chromospheric material in the lower chromosphere, while

the  $H_\alpha$  line is sensitive to the characteristics of the upper chromosphere. More recently two major paper series about M dwarf chromospheric models can be found. One makes use of the stellar atmosphere code Pandora (Avrett & Loeser 1984) and includes semi-empirical chromospheric modelling of AD Leo (Mauas & Falchi 1994). Two important papers in this series are Mauas (2000) and Falchi & Mauas (1998), where the authors investigate the influence of partial versus complete frequency redistribution for the Lyman lines. They also find that the Na D lines can substitute the Ca II K since they give also information about the atmospheric structure around the temperature minimum. The other paper series makes use of the stellar atmosphere code MULTI (Carlsson 1986) and includes modelling of the chromosphere of AU Mic (Houdebine & Doyle 1994) and of AD Leo besides four other M dwarfs with low to high activity levels (Short & Doyle 1998).

#### 1.1.4 Coronae

The Corona is the outer part of a stellar atmosphere. Like the chromosphere, historically it was observable for the Sun only during total eclipses. Nowadays one can use a coronagraph that provides an artificial eclipse. Furthermore, there is the possibility of X-ray observations. Since X-rays cannot penetrate the Earth's atmosphere, satellites are needed making X-ray astronomy a relatively young field. During the last years space missions like *SOHO* and *TRACE* have revealed the highly structured geometry of the hot plasma for the Sun. This plasma is magnetically trapped in coronal loops and associated with active regions. For other late-type stars recent satellites like *XMM-Newton* and *Chandra* have found ubiquitous X-ray emission and have made X-ray spectroscopy possible. The X-ray and extreme UV emission lines are produced by the hot, optically thin coronal plasma, which consists of highly ionised ions. Nevertheless, some forbidden coronal emission lines also appear in the optical and near infrared. Historically these optical forbidden lines were actually the first ones discovered and identified (e. g. Edlén 1945). Among the strong emission lines for the Sun, the Fe XIII line at 3388 Å is the bluest one. Therefore it is the best candidate to be observed against the faint photo-

spheric background in M dwarfs for studying coronal emission in the optical.

#### Heating mechanisms

Like the chromosphere, the corona needs additional heating which is thought to be provided by magnetic heating mechanisms. The plethora of possible magnetic heating mechanisms can be divided into alternating current and direct current mechanisms which are both eventually driven by the turbulence motions in the convection zone. The alternating current mechanisms involve different types of magneto-hydrodynamic waves generated by fast turbulent velocity fluctuations in the upper convection zone. The direct current mechanisms are due to slow convective motions that build up magnetic structures containing large amounts of energy, which is released via magnetic reconnection. The latter is also called micro-flare or nano-flare heating and is thought to be a very important heating mechanism for the corona (Narain & Ulmschneider 1996). A schematic illustration of the different stages leading to such a micro-flare event can be seen in Fig. 1.6. While the photospheric footpoints of coronal loops are moved by the slow convective motions, the magnetic field lines are embraided. When two regions with substantially antiparallel field configurations are pushed together a current sheet forms between them. The current sheet may be regarded as a discontinuity between two antiparallel fields and it is called a neutral sheet, if the magnetic field is vanishing in the third direction perpendicular to the current sheet. In such a current sheet, magnetic reconnection may take place. This requires magnetic diffusion and thus implies the breakdown of the non-resistive regime described by the *ideal magneto-hydrodynamics* that has its name from the infinite i. e. ideal conductivity.

The plasma then moves into the current sheet vertical to the field lines and moves out of the reconnection area along the field lines. Magnetic diffusion is necessary in a small region allowing plasma and magnetic field to move independently of each other. Then the magnetic field lines reconnect and are carried out of the reconnection region by the outflowing plasma. Thus the field ends up with a more simple geometry and energy is re-

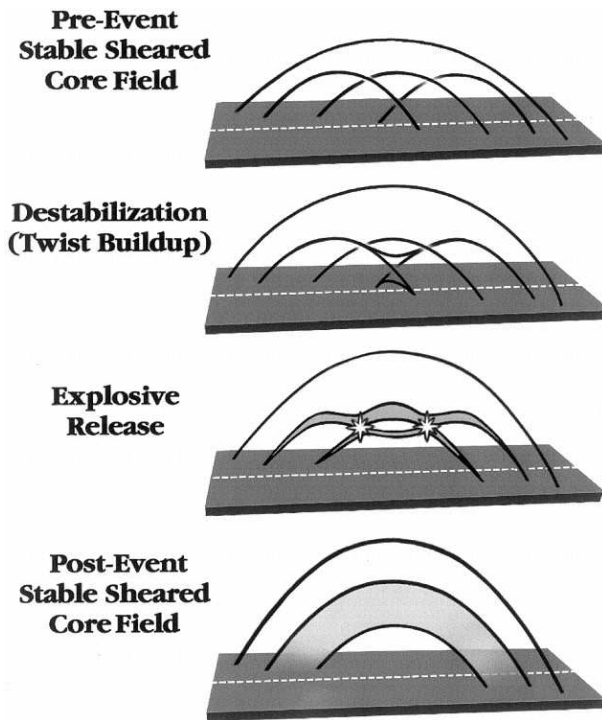


Figure 1.6: Schematic picture of a loop geometry that leads to reconnection events. From top to bottom: Stable loop structures are embraided by foot-point motions leading to magnetic energy stored in the loops. This energy can be released by reconnection leading to a simpler geometry. (Image taken from Moore et al. (1999).)

leased. An extensive discussion of reconnection with an emphasis on the historic development of this theory can be found in Haigh et al. (2005).

## 1.2 The stellar atmosphere code PHOENIX

In Fig. 1.7 an example of a typical short wavelength range in the blue part of a M dwarf spectrum is given. Clearly photospheric absorption lines and chromospheric emission lines are found next to each other, and even photospheric absorption lines with chromospheric emission cores are seen. For disentangling the complex line pattern a stellar atmosphere code can be used for calculating theoretical spectra, which can be compared to the observed spectra. In the course of this work the stellar at-

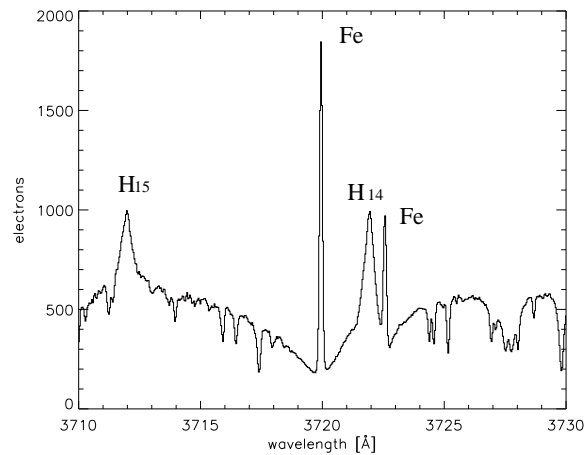


Figure 1.7: Example of a short wavelength interval in the blue part of the spectrum of AD Leo (M3.5). Notice, that the two high members of the Balmer line series are broader than other emission lines.

mosphere code PHOENIX (Hauschildt et al. 1999) has been used.

PHOENIX uses a given atmospheric structure to self-consistently solve the hydrostatic equations, the radiative transfer equations and the rate equations. Normally also a temperature correction is applied. The general iteration scheme for one iteration for a chromospheric model is shown in Fig. 1.8. The following section gives an overview about chromospheric modelling and some technical details. More information on the construction of the individual chromospheres can be found in chapters 6, 5, and in the Appendix.

### Construction of chromospheric models

The chromosphere models are constructed in two steps. First a photospheric model in radiative equilibrium is computed for the considered star. This photospheric model is characterised by the effective temperature, surface gravity and chemical composition. In the course of this work only solar chemical composition was considered - for the photospheres as well as for the chromospheres.

In a second step an arbitrary temperature rise is attached to the photosphere representing the unknown heating mechanisms. Consequently the atmosphere cannot be in radiative equilibrium any-

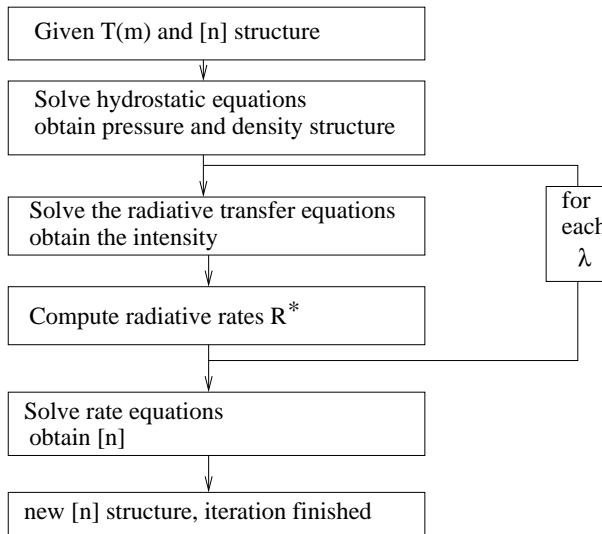


Figure 1.8: Flow chart of one PHOENIX iteration for a chromosphere model without temperature correction. The temperature is given on a column mass grid  $m$ , while  $n$  denotes the level population numbers.

more and no temperature correction is applied. In this second step the temperature structure is given on a column mass grid on which the hydrostatic equations are solved. Moreover in the second step generally 10 iterations are applied to the atmospheric structure for allowing the coupled NLTE rate equations and the radiative transfer equations to converge. This is normally enough to converge the spectrum in the considered wavelength range to about 10 percent flux variation in strong lines and to better than 1 percent otherwise.

In contrast to the photosphere, where only three parameters characterise the model, the given temperature structure defines the free parameters of the chromospheric model, which are the following: column mass at the temperature minimum, column mass at the onset of the transition region, temperature at the onset of the transition region, temperature gradient in the transition region, temperature at the top of the model, and the turbulent velocity in units of the sound velocity. With that many parameters, the question of the uniqueness of the solution arises immediately. Of course, this problem is less severe if many lines are used for the construction of the model.

For models with a chromosphere NLTE computations turned out to be of great importance. Therefore, the next subsection deals with different approaches for calculating the level populations.

### 1.2.1 Line formation and different approximations

Absorption lines with emission cores reflect the temperature stratification in the star's atmosphere for classical semi-empirical models. Since the line absorption coefficient is largest near line centre the optical depth reaches unity higher in the atmosphere than for wavelengths in the line wings. Therefore the line centre is formed in higher regions of the atmosphere than the wings and since the source function declines outwards in the photosphere an absorption line is formed. If the atmosphere has a chromosphere above the photosphere, a temperature minimum exists leading to a temperature rise further out. As a result the source function changes its slope at the temperature minimum forming an emission core in the absorption line.

This already illustrates that the formation of the chromospheric emission lines is somewhat more complicated than the formation of coronal emission lines, which form in an entirely optically thin medium, or the formation of pure absorption lines in the photosphere. For the line formation the occupation numbers of the different levels in the atoms are an essential ingredient. These can be computed using different approximations.

#### Coronal approximation

In the corona the level population is normally computed using the *coronal approximation*. This approximation assumes that the exclusively radiative depopulation of a level is balanced exclusively by collisional excitation from the ground state. This approximation breaks down in the higher pressure medium of the chromosphere where at least some of the lines are optically thick.

#### LTE approximation

Another approximation for the level population is the *local thermodynamic equilibrium* (LTE)

approximation often used for modelling photospheres. This does not imply that the whole stellar atmosphere is in thermodynamic equilibrium – which clearly is not the case, otherwise stars would be blackbody radiators. Instead each small volume element of the atmosphere of the star is assumed to be governed by its temperature which may be different from the temperature of another small volume element of the star's atmosphere. This allows the atmosphere of the star to be non-isothermal and transport energy. The level population in this case is given by the Saha-Boltzmann-distribution as follows:

$$\frac{n_{r+1,u}}{n_{r,l}} = \frac{2}{N_e} \frac{g_{r+1,u}}{g_{r,l}} \left( \frac{2\pi m_e k T}{h^2} \right)^{3/2} e^{-\chi/kT},$$

where  $\frac{n_{r+1,u}}{n_{r,l}}$  is the population density ratio for the ionisation stage  $r$ , the upper level  $u$  and the lower level  $l$ . Moreover  $N_e$  is the electron density,  $m_e$  the electron mass,  $k$  the Boltzmann constant,  $h$  the Planck constant,  $T$  the temperature,  $g_{r+1,u}$  and  $g_{r,l}$  the statistical weights for the level and  $\chi$  the energy between the two levels (including ionisation energy).

### NLTE approximation

The LTE approximation is a good assumption, if there are enough absorption events to thermalize the photons before they travel over a distance, where significant temperature changes occur. Therefore, in the higher atmosphere, where a significant portion of the photons can escape, the LTE approximation must break down. In this case the level population cannot be computed by the Saha-Boltzmann-distribution anymore. In the non-LTE (NLTE) case the level population can be obtained via *statistical equilibrium*, assuming that the level population is constant with time. This leads to the rate equation, where the radiative and collisional excitation rates are balanced by the (radiative and collisional) de-excitation rates for a certain level population density  $n_i$ :

$$\sum_{j<i} n_j (R_{ji} + C_{ji}) + \sum_{j>i} n_j \left( \frac{n_i^*}{n_j^*} \right) (R_{ji} + C_{ji}) - n_i \sum_{j<i} \left( \frac{n_j^*}{n_i^*} \right) (R_{ji} + C_{ji}) - n_i \sum_{j>i} (R_{ij} + C_{ij}) = 0$$

with  $n_i^*$  denoting LTE occupation numbers,  $R_{ji}$  the radiative rates and  $C_{ji}$  the collisional rates. This system of equations can be closed using the conservation of the number of particles and charge conservation. They are solved in PHOENIX using a formulation with an approximate rate operator and an operator splitting method similar to the  $\Lambda$ -iteration method commonly used for solving the radiative transfer equations (Hauschildt 1993).

### Departure coefficients

Once the occupation numbers have been obtained, one may be interested in the departure of the system from LTE. This is quantified by the *departure coefficients*  $b_i = \frac{n_i}{n_i^*}$ . By other authors (e. g. Vernazza et al.) another definition of the departure coefficients is used:  $b_l = (n_l/n_l^*)/(n_k/n_k^*)$ , where the index  $k$  denotes the continuum. In the case of LTE we have  $b_i = 1$ . For chromospheric models for the Sun the departure coefficients are small, for example for hydrogen  $b_i$  ranges from  $\approx 0.1$  to 100 in the chromosphere (Vernazza et al. 1981). In M dwarfs the departure from LTE is much more severe. As for the Sun the levels are underpopulated at the temperature minimum with the  $b_i$ s going down as far as  $10^{-15}$  (note that this cannot be directly compared to the Vernazza et al. departure coefficients due to the different definitions). An example of the departure coefficients for an M dwarf model for hydrogen can be found in Fig. 1.9. While deep in the photosphere the departure coefficients are nearly equal to one, they decrease in the higher photosphere. When approaching the temperature minimum, the departure coefficients reach their minimum as well. The steep temperature increase in the transition region is reflected in a similar steep increase in the departure coefficients. Higher levels generally exhibit weaker departure from LTE, indicating an enhanced collisional influence on the level population. Therefore, it is extremely important to calculate the level populations in NLTE.

Even NLTE may be a poor approximation if the idea of a chromosphere heated by acoustic shock waves is true, because the statistical equilibrium assumes an instantaneous adjustment of the occupation numbers to the local thermodynamic and radiation state. There are radiation-hydrodynamic sim-

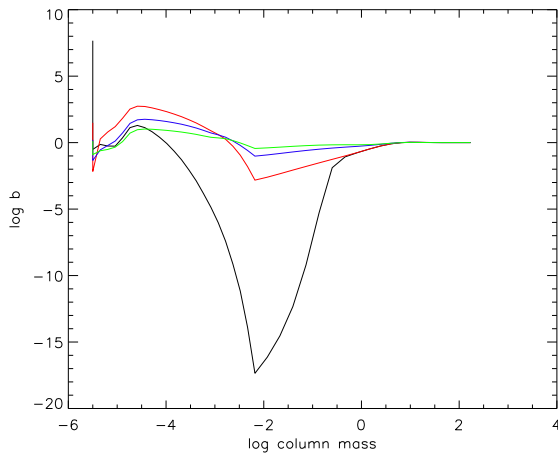


Figure 1.9: Departure coefficients  $b_n$  for hydrogen vs. columns mass for an M dwarf chromospheric model. Black is for the level  $n=1$ , red for  $n=2$ , blue for  $n=3$  and green for  $n=4$ . The sharp peak in the departure coefficients at  $\log$  column mass = -2 is caused by the temperature minimum. The nearly vertical rise at about  $\log$  column mass = -5.5 is caused by the onset of the transition region.

ulations for the Sun suggesting that the hydrogen ionisation has not enough time to reach its equilibrium in the high chromosphere (Carlsson & Stein 2002).

### 1.3 Outline

The present thesis deals with chromospheric and coronal activity as observed in a sample of 24 late-type stars and brown dwarfs. The sample densely covers the M dwarf regime from M3.5 to M9 and additionally includes one M1 star and three L3 dwarfs. All stars of the sample are known to be active and the majority are strong X-ray emitters. The L3 dwarfs are known to be either rapid rotators or to show  $H_\alpha$  emission.

The observations were carried out with the VLT Kueyen telescope equipped with the UVES echelle spectrograph in winter 2001 (monochroic mode) and in March 2002 (dichroic mode). Since two of the objects were binary stars whose spectra could not be disentangled and one object was underexposed the actual sample consists of 21 objects,

whereof three are early L dwarfs. Further informations about the observations and data analysis can be found in chapter 2.

The spectra of the whole sample are dominated by molecule bands in the red range and by chromospheric emission lines in the blue range. Since most of these emission lines have not been identified so far in the spectra of M dwarfs, an extensive line list for each object was produced in the course of this work, stating central wavelength, equivalent width, FWHM and the identification for each line. This line list is available online at CDS under <http://cdsweb.u-strasbg.fr/>. Some remarks on individual stars and a more detailed discussion of the identifications can be found in the appendix A of chapter 6.

At the beginning of the activity analysis a search for the forbidden coronal Fe XIII line at 3388.1 Å was carried out. For other stars than the Sun thermal emission of the hot corona was detected only at X-ray/EUV wavelengths and thus observable only from space, until the Fe XIII line was found in the active M5.5 star CN Leo (Schmitt & Wichmann 2001). Since X-ray observations suffer from rather low resolution compared to optical spectroscopy, ground based observations of the coronal plasma are highly desirable. This work led to a clear detection of the Fe XIII line during a flare on LHS 2076. Also variability of the line in CN Leo were found. A comprehensive discussion of all the analysis regarding the Fe XIII line can be found in chapter 2, which also describes the consequences of the non-detection of other coronal forbidden lines in this wavelength range.

Since all other emission lines seen in the spectral sample are chromospheric lines, the focus of the further analysis lies on the chromospheric activity of individual stars in the sample. In chapter 3 the influence of a flare on the spectrum of the old M9 dwarf DENIS 104814.7-395606.1 is discussed. Line shifts to bluer wavelength were discovered in several lines indicating mass motions during the flare. The lines were fitted with Gaussians treating central wavelength, amplitude and FWHM as free parameters.

The conclusions from such an approach on the atmospheric structure of the chromosphere are very limited. Therefore, semi-empirical chromosphere

models calculated with PHOENIX are used for further interpretation of the M dwarfs spectra. In chapter 4 general characteristics of the chromospheric models are discussed as well as several problems which arose during the model construction. After some improvements on the treatment of the turbulent pressure were done, the chromospheric models were applied to the spectra of the decay phase of a flare on the M6 dwarfs LHS 2034. They helped to interpret line asymmetries in the red wing of the hydrogen and helium lines that occurred during the flare. In chapter 5 these asymmetries are interpreted as downflows in the upper chromosphere of LHS 2034.

Moreover, model chromospheres were constructed for the quiescent emission of five M dwarfs with  $T_{\text{eff}}$  ranging from 3200 K down to 2500 K. One result of this study is that the M dwarf spectra can all be fitted with models consisting of two linear temperature distributions for the chromosphere and transition region, respectively. Thus there seems to be no principal difference between the heating mechanisms of mid-type and late-type M dwarfs. Another result is that the NLTE vs. LTE treatment of carbon, nitrogen, and oxygen influences the electron pressure and consequently the level population of other elements. The results from this study are summarised in chapter 6.

After the importance of NLTE calculations became apparent for the M dwarfs a detailed study of this phenomenon was carried out for the case of the Sun. Taking the classical VAL C model from Vernazza et al. (1981) and recomputing it with different sets of NLTE species showed the influence of crosstalk between different elements. As a consequence LTE calculations of nitrogen, oxygen, sulfur, and argon lead to an over-photoionisation of hydrogen and thus to totally unrealistic hydrogen emission. This points once again to the importance of NLTE calculations. An extensive discussion of this subject can be found in chapter 7.

Finally, a summary can be found in chapter 8 as well as an outlook to future possible work.

## References

- Avrett, E. H. & Loeser, R. 1984, in *Methods in Radiative Transfer*, 341–379
- Ayres, T. R. 2002, *ApJ*, 575, 1104
- Ayres, T. R. & Rabin, D. 1996, *ApJ*, 460, 1042
- Babcock, H. W. 1961, *ApJ*, 133, 572
- Berger, E., Rutledge, R. E., Reid, I. N., et al. 2005, *ApJ*, 627, 960
- Briggs, K. R. & Pye, J. P. 2004, *MNRAS*, 353, 673
- Burgasser, A. J., Liebert, J., Kirkpatrick, J. D., & Gizis, J. E. 2002, *AJ*, 123, 2744
- Burgasser, A. J. & Putman, M. E. 2005, *ApJ*, 626, 486
- Carlsson, M. 1986, Uppsala Observatory Internal Report no. 33
- Carlsson, M. & Stein, R. F. 1995, *ApJ*, 440, L29
- Carlsson, M. & Stein, R. F. 1997, *ApJ*, 481, 500
- Carlsson, M. & Stein, R. F. 2002, *ApJ*, 572, 626
- Cram, L. E. & Mullan, D. J. 1979, *ApJ*, 234, 579
- Dorch, S. B. F. & Nordlund, Å. 2001, *A&A*, 365, 562
- Durney, B. R., De Young, D. S., & Roxburgh, I. W. 1993, *Sol. Phys.*, 145, 207
- Eddy, J. A. 1976, *Science*, 192, 1189
- Edlén, B. 1945, *MNRAS*, 105, 323
- Falchi, A. & Mauas, P. J. D. 1998, *A&A*, 336, 281
- Fontenla, J. M., Avrett, E. H., & Loeser, R. 1990, *ApJ*, 355, 700
- Fossum, A. & Carlsson, M. 2005, *Nature*, 435, 919
- Friis-Christensen, E. & Lassen, K. 1991, *Science*, 254, 698
- Güdel, M., Audard, M., Kashyap, V. L., Drake, J. J., & Guinan, E. F. 2003, *ApJ*, 582, 423
- Gelino, C. R., Marley, M. S., Holtzman, J. A., Ackerman, A. S., & Lodders, K. 2002, *ApJ*, 577, 433
- Andretta, V., Doyle, J. G., & Byrne, P. B. 1997, *A&A*, 322, 266

- Giampapa, M. S. & Liebert, J. 1986, *ApJ*, 305, 784
- Giampapa, M. S., Worden, S. P., & Linsky, J. L. 1982, *ApJ*, 258, 740
- Gizis, J. E., Monet, D. G., Reid, I. N., et al. 2000, *AJ*, 120, 1085
- Haigh, J. D., Lockwood, M., & Giampapa, M. S., eds. 2005, *The sun, solar analogs and the climate*
- Hale, G. E. & Nicholson, S. B. 1925, *ApJ*, 62, 270
- Hartmann, W. K. & Impey, C. 1994, *Astronomy : the cosmic journey* (Belmont, Calif. : Wadsworth Pub., c1994. 5th ed.)
- Hauschildt, P. H. 1993, *JQSRT*, 3, 301
- Hauschildt, P. H., Allard, F., & Baron, E. 1999, *ApJ*, 512, 377
- Houdebine, E. R. & Doyle, J. G. 1994, *A&A*, 289, 185
- Johns-Krull, C. M. & Valenti, J. A. 1996, *ApJ*, 459, L95+
- Lang, K. R. 2001, *The Cambridge Encyclopedia of the Sun* (The Cambridge Encyclopedia of the Sun, by Kenneth R. Lang. Cambridge University Press, 2001, 268 pp.)
- Liebert, J., Kirkpatrick, J. D., Cruz, K. L., et al. 2003, *AJ*, 125, 343
- Marsh, N. & Svensmark, H. 2003, *Space Science Reviews*, 107, 317
- Mauas, P. J. D. 2000, *ApJ*, 539, 858
- Mauas, P. J. D. & Falchi, A. 1994, *A&A*, 281, 129
- Mohanty, S. & Basri, G. 2003, *ApJ*, 583, 451
- Moore, R. L., Falconer, D. A., Porter, J. G., & Suess, S. T. 1999, *ApJ*, 526, 505
- Moreno-Insertis, F., Schuessler, M., & Ferriz-Mas, A. 1992, *A&A*, 264, 686
- Mullan, D. J. & MacDonald, J. 2001, *ApJ*, 559, 353
- Narain, U. & Ulmschneider, P. 1996, *Space Science Reviews*, 75, 453
- Pagano, I., Linsky, J. L., Carkner, L., et al. 2000, *ApJ*, 532, 497
- Robrade, J. & Schmitt, J. H. M. M. 2005, *A&A*, 435, 1073
- Schmitt, J. H. M. M. & Wichmann, R. 2001, *Nature*, 412, 508
- Schrijver, C. J. & Zwaan, C. 2000, *Solar and stellar magnetic activity (Solar and stellar magnetic activity / Carolus J. Schrijver, Cornelius Zwaan. New York : Cambridge University Press, 2000. (Cambridge astrophysics series ; 34))*
- Short, C. I. & Doyle, J. G. 1998, *A&A*, 336, 613
- Stelzer, B. 2004, *ApJ*, 615, L153
- Stix, M. 2004, *The sun : an introduction* (The sun : an introduction, 2nd ed., by Michael Stix. Astronomy and astrophysics library, Berlin: Springer, 2004. ISBN: 3540207414)
- Uitenbroek, H. 2000, *ApJ*, 536, 481
- Uitenbroek, H., Noyes, R. W., & Rabin, D. 1994, *ApJ*, 432, L67
- Vernazza, J. E., Avrett, E. H., & Loeser, R. 1973, *ApJ*, 184, 605
- Vernazza, J. E., Avrett, E. H., & Loeser, R. 1976, *ApJS*, 30, 1
- Vernazza, J. E., Avrett, E. H., & Loeser, R. 1981, *ApJS*, 45, 635
- Wedemeyer, S., Freytag, B., Steffen, M., Ludwig, H.-G., & Holweger, H. 2004, *A&A*, 414, 1121
- Wiedemann, G., Ayres, T. R., Jennings, D. E., & Saar, S. H. 1994, *ApJ*, 423, 806
- Wilhelm, K. & Kalkofen, W. 2003, *A&A*, 408, 1137



## **Chapter 2**

# **Fe XIII coronal line emission in cool M dwarfs**

**B. Fuhrmeister, J. H. H. M. Schmitt and R. Wichmann**  
*Astronomy & Astrophysics*, 417, 701 (2004)



A&A 417, 701–713 (2004)  
DOI: 10.1051/0004-6361:20034464  
© ESO 2004

**Astronomy  
&  
Astrophysics**

## Fe XIII coronal line emission in cool M dwarfs<sup>★</sup>

B. Fuhrmeister, J. H. M. M. Schmitt, and R. Wichmann

Hamburger Sternwarte, University of Hamburg, Gojenbergsweg 112, 21029 Hamburg, Germany

Received 7 October 2003 / Accepted 17 December 2003

**Abstract.** We report on a search for the Fe XIII forbidden coronal line at 3388.1 Å in a sample of 15 M-type dwarf stars covering the whole spectral class as well as different levels of activity. A clear detection was achieved for LHS 2076 during a major flare and for CN Leo, where the line had been discovered before. For some other stars the situation is not quite clear. For CN Leo we investigated the timing behaviour of the Fe XIII line and report a high level of variability on a timescale of hours which we ascribe to microflare heating.

**Key words.** stars: activity – stars: coronae – stars: late-type

### 1. Introduction

The solar corona can be studied at extremely high spatial and spectral resolution over almost the entire range of the electromagnetic spectrum. With typical coronal plasma temperatures of a few million degrees the bulk of the Sun's coronal energy losses is emitted in the X-ray range, the energy losses at shorter and longer wavelengths being considerably smaller. Therefore observations of the solar corona in the optical are quite difficult because of the faintness of the corona compared to the photosphere in this wavelength range. This problem can be overcome at least for observations above the solar limb if the photospheric light is blocked, e.g. by the Moon during an eclipse or – artificially – by a coronagraph. Optical observations of the solar corona carried out in that fashion were the first to reveal the true nature of the corona as a hot plasma with temperatures much higher than the underlying chromosphere or photosphere. However, the solar corona could only be observed off the limb in the optical, and only through satellite-based imaging observations of the corona at X-ray and EUV wavelengths the corona at large could be observed and studied.

The existence of coronae similar to that of the Sun around essentially all late-type main sequence stars with outer convection zones has been established by extensive X-ray studies (e.g. Schmitt 1997). As is the case for the Sun, the bulk of the energy losses for stellar coronae also occurs in the X-ray range, and consequently this spectral band is the most natural one for the study of stellar coronae. However, coronal emission from stars can also be observed in the radio range (e.g. Berger 2002 or Güdel 2002) and in the optical (Schmitt & Wichmann 2001). Coronal observations at those latter wavebands are

extremely difficult since the coronal emissions are much fainter, and especially in the optical, the weak coronal emission has to be detected above the usually much brighter optical photospheric emission. The most promising candidates to search for optical coronal emission are clearly late-type M dwarf stars, which can be as X-ray bright as or even X-ray brighter than the Sun, but whose photospheric emission is rather faint in particular at near UV wavelengths. The detection of coronal emission in the optical was recently accomplished for the active M-star CN Leo, where Schmitt & Wichmann (2001) were able to detect the Fe XIII forbidden coronal line at 3388.1 Å. This successful detection of coronal emission in one star raises the question to what extent such detections are possible for other cool stars as well or whether CN Leo is a unique and singular case.

In this paper we will discuss the problems of detecting the 3388.1 Å forbidden coronal line in a small sample of late-type stars and present an analysis of the temporal variability of this line in the “proto-type” CN Leo. Our paper is structured as follows: In Sect. 2 we describe the VLT data used for our analyses and the sample of investigated stars. In Sect. 3 an overview over the spectral range under investigation is given, while in Sect. 4 we deal with the rotational velocity of the analyzed stars. In Sect. 5 the results of our search for the Fe XIII line for individual stars are presented and the timing behavior of the line for CN Leo is discussed in Sect. 6. Section 7 deals with the X-ray to Fe XIII line ratio for CN Leo and LHS 2076. In Sect. 8 we describe the results of our search for other forbidden coronal lines in CN Leo.

### 2. Observations and data analysis

The observations reported in this paper were obtained in visitor mode with ESO's Kueyen telescope at Paranal equipped with the Ultraviolet-Visual Echelle Spectrograph (UVES) from

Send offprint requests to: B. Fuhrmeister,  
e-mail: bfuhrmeister@hs.uni-hamburg.de

<sup>★</sup> Based on observations collected at the European Southern Observatory, Paranal, Chile, 68.D-0166A.

**Table 1.** Basic observations parameters of the observed stars.

name	other name	spectral type	$\log L_X^1$	observations	Ti II lines	highest Balmer line
LHS 1827	GJ 229A	M 1	27.13 <sup>a</sup>	2002-03-15 4 spectra 1200s	absorption	–
LHS 428		M 3e	28.75 <sup>a</sup>	2002-03-15 2 spectra 1200s	absorption	H <sub>18</sub>
LHS 6158		M 3.5	28.76 <sup>c</sup>	2002-03-15 2 spectra 2400s	weak absorption	H <sub>18</sub>
LHS 5167	AD Leo	M 3.5	28.92 <sup>a</sup>	2002-03-13 3 spectra 1800s 2002-03-16 2 spectra 1200s	emission	H <sub>18</sub>
HD 196982	AT Mic	M 4.5	29.55 <sup>c</sup>	2002-03-16 2 spectra 2400s	emission	H <sub>20</sub>
LHS 1943	YZ CMi	M 4.5e	28.67 <sup>b</sup>	2002-03-13 3 spectra 3600s	emission	H <sub>24</sub>
LHS 2664	FN Vir	M 4.5	27.92 <sup>b</sup>	2002-03-13 3 spectra 3600s	weak emission	H <sub>18</sub>
LHS 324	GL Vir	M 5	27.65 <sup>a</sup>	2002-03-13 3 spectra 3600s 2002-03-16 2 spectra 2400s	weak emission	H <sub>19</sub>
LHS 36	CN Leo	M 5.5	27.78 <sup>a</sup>	2002-03-13 6 spectra 7200s 2002-03-14 4 spectra 4800s 2002-03-15 6 spectra 7200s 2002-03-16 6 spectra 7200s 2001-01-06 1 spectrum 3120s	emission	H <sub>24</sub>
LHS 2076	EI Cnc	M 5.5	27.60 <sup>a</sup>	2002-03-15 4 spectra 4800s 2002-03-16 1 spectrum 1200s	–	H <sub>18</sub>
LHS 49	Prox Cen	M 5.5	27.26 <sup>a</sup>	2001-02-02 1 spectrum 3120s	weak emission	H <sub>18</sub>
LHS 10	UV Cet	M 5.5	27.31 <sup>a</sup>	2000-12-17 1 spectrum 3120s	emission	H <sub>18</sub>
LHS 248	DX Cnc	M 6	26.60 <sup>a</sup>	2002-03-16 3 spectra 3600s	–	H <sub>11</sub>
LHS 2034	AZ Cnc	M 6	28.89 <sup>c</sup>	2002-03-14 6 spectra 6000s 2002-03-16 2 spectra 2400s	emission	H <sub>17</sub>
LHS 292		M 6.5		2001-02-02 1 spectrum 3120s	–	H <sub>15</sub>

<sup>1</sup> In erg s<sup>-1</sup>.<sup>a</sup> Schmitt et al. (1995).<sup>b</sup> Delfosse et al. (1998).<sup>c</sup> Hüensch et al. (1999).<sup>d</sup> Schmitt & Liefke (2002) X-ray luminosity is variable.

March, 13th to 16th in 2002, with the exception of UV Ceti, Prox Cen, LHS 292 and one of the CN Leo spectra, which were observed in service mode during the winter season 2000/2001. For the March 2002 run the instrument was operated in a dichroic mode, yielding 33 echelle orders in the blue arm (spectral coverage from 3030 to 3880 Å) and 39 orders in the red arm (spectral coverage from 4580 to 6680 Å). For the runs in the winter 2000/2001 a monochroic setup was used, providing us only with the blue part of the spectrum. In the dichroic setup the red part of the spectrum is recorded on two separate CCDs; therefore there is a spectral gap from ~5640 to 5740 Å, resulting from a spatial gap between the two CCDs. As a consequence of the various instrumental constraints we cannot observe the lines from H<sub>3</sub> up to H<sub>8</sub> of the Balmer series, nor do we cover the Ca II H and K lines. The typical resolution of our spectra is ~45 000, typical exposures times were 20 min except for the brighter among our sample stars. Normally for each star three exposures were taken in sequence in order to facilitate the recognition of cosmics, again with the exception of the four spectra of CN Leo, UV Ceti, Prox Cen and LHS 292 taken during the winter season 2000/2001.

A list of the observed stars and the available spectra for each star is provided in Table 1, giving the observation dates and total exposure times. Moreover we provide some basic parameters of the sample stars, including the highest detected Balmer line in our data as an estimator of activity. Note that during the March 2002 run CN Leo was observed nightly to carry out an investigation of its chromospheric and coronal variability.

All data were reduced using IRAF, including flat-fielding, order definition and scattered light subtraction. The wavelength calibration was carried out using Thorium-Argon spectra with an accuracy of ~0.03 Å in the blue arm and ~0.05 Å in the red arm. In addition there are photometric data from the UVES exposure meter taken for engineering purposes and therefore not flux calibrated. Still, these data were useful to assess whether the star was observed during quiescence or during a major flare.

The spectral line fits were carried out with the CORA fit program (Ness & Wichmann 2002). This software tool was originally developed for analyzing high resolution X-ray spectra, but the fit algorithms employed by CORA are also well suited for the modeling of well-defined chromospheric and coronal emission lines. The program provides an accurate error

analysis. All fits were carried out using Gaussian line profiles after shifting the wavelength to the stars' rest frame.

### 3. Detection of the Fe XIII line

The prime target of our observing program was the spectral region around 3388 Å. The specific transition under consideration is  $3s^2 3p^2 \ ^3P_2 - ^1D_2$ . Flower & Pineau des Forets (1973) give a detailed discussion of the atomic physics of Fe XIII and provide level population calculations for a range of temperatures and densities, considering direct excitation due to collisions with electrons and protons and indirect excitation of allowed transitions via collisions with electrons followed by radiative decay and find rather low dependence on temperature.

In order to give an overview of the nature and quality of our spectra, we show (in Fig. 1) the spectral range between 3370 Å–3390 Å for most of our program stars. LHS 292 is not shown since its spectrum is very similar to DX Cnc, and LHS 428 and LHS 6158 are not shown since they are both double stars with very complicated spectra that could not be disentangled and were therefore excluded from the analysis. The spectra shown in Fig. 1 are sorted by decreasing spectral type. One notes a distinct sequence from “early” M dwarfs to “late” M dwarfs. In the “early” M dwarfs like Gl 229A and AD Leo one still recognizes a clear photospheric spectrum in the range 3370 Å–3390 Å with some additional chromospheric emission lines, while in the later type M dwarfs like CN Leo and the (flaring) LHS 2034 an almost pure emission line spectrum appears; these latter spectra are obviously dominated by the stellar chromospheres rather than their photospheres.

The Fe XIII line at 3388.1 Å detected in CN Leo by Schmitt & Wichmann (2001) is – unfortunately – blended with a Ti II chromospheric line at 3387.846 Å. This particular Ti II line and other emission lines from the same multiplet are present in all recorded spectra besides the non-flare spectra of LHS 2034 and LHS 2076 and the spectrum of DX Cnc. In GL 229A Ti II appears to be present in absorption.

The stars earlier than M 4.5 have a rather high pseudo-continuum in the considered wavelength range which is clearly dominated by overlapping absorption lines. This continuum strongly decreases for the spectral types M 3.5–M 4.5 stars by a factor of ten, accompanied by the vanishing of the strong absorption features in this regime. Consequently, a detection of the Fe XIII line should be much easier for spectral types later than M 4.5. Therefore the most promising search for coronal line emission can be made for stars in the spectral range M 4.5–M 6 since for later stars even the normally strong chromospheric Ti II emission lines cannot be detected any more.

### 4. Determination of rotational velocities

A critical issue for the successful separation of the chromospheric Ti II emission line at 3387.846 Å and the coronal Fe XIII emission line at 3388.1 Å are the intrinsic line broadening profiles of these lines. The wavelength difference between those lines ( $\approx 0.26$  Å) corresponds to a velocity of  $\approx 23$  km s<sup>-1</sup>,

easily within the reach of thermal and rotational velocities. Obviously, the thermal broadening profiles differ substantially because of the different origins of these lines, and rapid rotation is expected at least for the more active stars. Since we clearly need accurate values for  $v \sin i$  for disentangling the Ti II and Fe XIII emission lines, we decided to measure it for some of our program stars. In order to determine  $v \sin i$  we used 18 of the red arm orders that show no strong emission lines either from the star or from terrestrial airglow. As a template we decided to use CN Leo since CN Leo is known to rotate very slowly ( $v \sin i < 2.9$  km s<sup>-1</sup>, Delfosse et al. 1998). The measured spectrum of CN Leo was spun up with rotational velocities from 3 up to 45 km s<sup>-1</sup>. The best fit value for the rotation velocity  $v \sin i$  of the spun up template and the star under study was determined with a  $\chi^2$ -test for every order used. The final rotational velocity was determined by averaging the values obtained in the different orders. We mostly used only the red part of the spectrum since in the blue part of the spectrum it is rather difficult to find larger regions unaffected by emission lines. We tried to avoid this problem of the blue spectra by using only very narrow spectral ranges ( $\sim 10$  Å) of every aperture, yet the issues of which lines are in emission, which show emission cores and which are purely in absorption are very different for each program star. Therefore the template has to be very similar to the test star and the used wavelength intervals have to be determined individually but even then the scatter for the wavelength intervals is bigger than in the red arm. Therefore we determined the rotational velocity for only three stars in the blue arm. For these stars we used Prox Cen as template since its spectrum is very similar to these stars. CN Leo could not be used as template because it is much more active than the measured stars. The rotational velocities determined in this fashion are listed in Table 2. In general, the values determined by us agree with previously determined ones found in the literature with the exception of GL Vir, where we find a substantially larger rotational velocity both in the red and blue arm than Delfosse et al. (1998). A careful visual inspection and comparison of the spectra of GL Vir with those obtained for FN Vir and AD Leo shows a very high similarity to the faster rotating spectrum. Moreover we used a template star very similar to GL Vir in spectral type while Delfosse et al. used a synthetic K0III spectrum. Therefore we do favor our (larger) rotational velocity.

For the double star UV Cet we measure a rotational velocity of  $25.9 \pm 8.6$  km s<sup>-1</sup> which agrees with the value found by Mohanty & Basri (2003) for UV Cet B. Since UV Cet A has a similar rotation velocity (G. Basri, private communication) it cannot be decided from the rotational velocity which component of UV Cet dominates our spectrum.

### 5. Observations of individual stars

Since the spectral properties of our sample stars are very different we applied specific methods for the individual stars for a detection or non-detection of the Fe XIII line. These are discussed in detail below.

704

B. Fuhrmeister et al.: Fe XIII in cool M stars

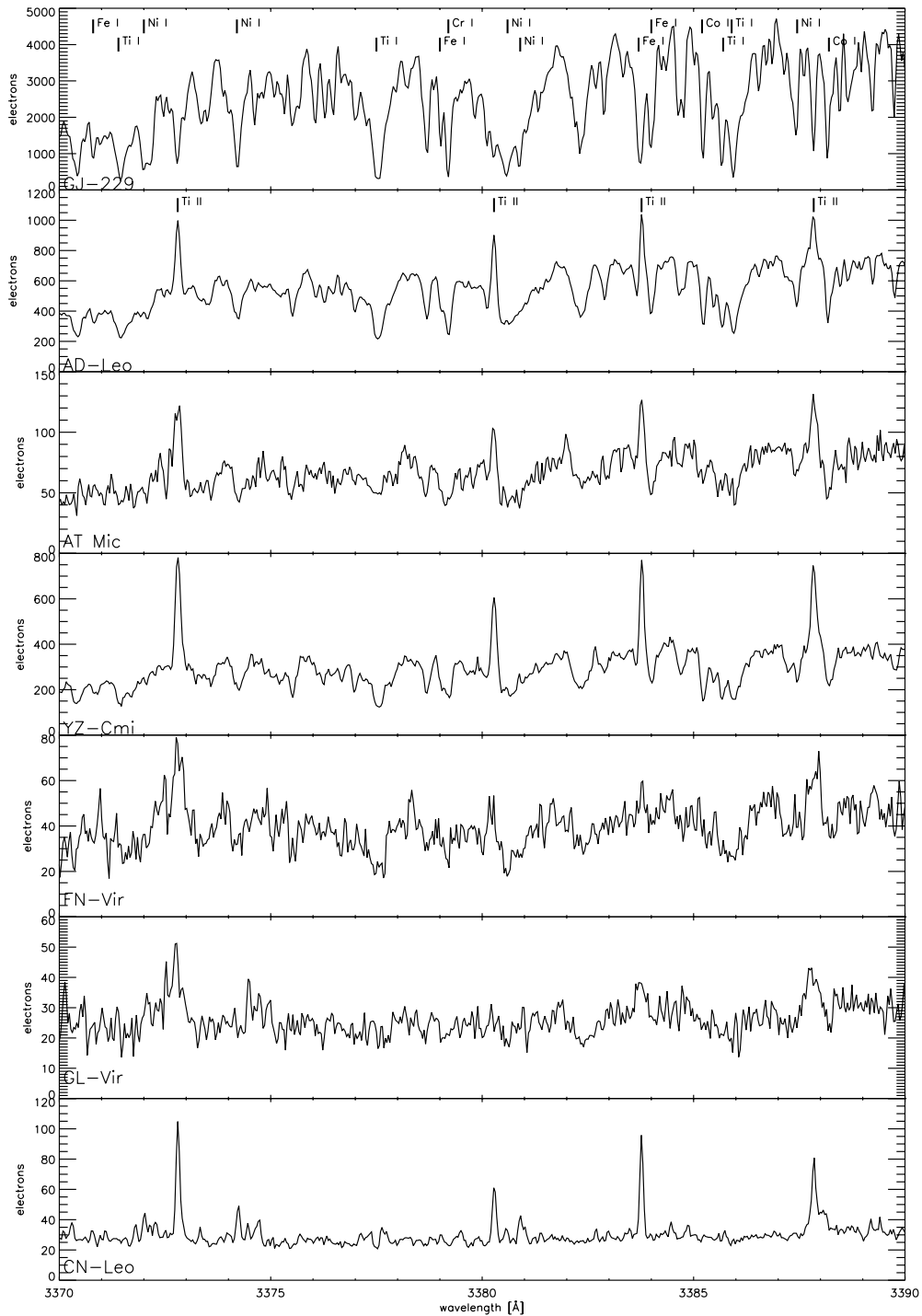


**Fig. 1.** The considered wavelength range of selected program stars. Some strong absorption lines are identified in the top spectrum. The Ti II emission lines are marked in the spectrum of Ad Leo.

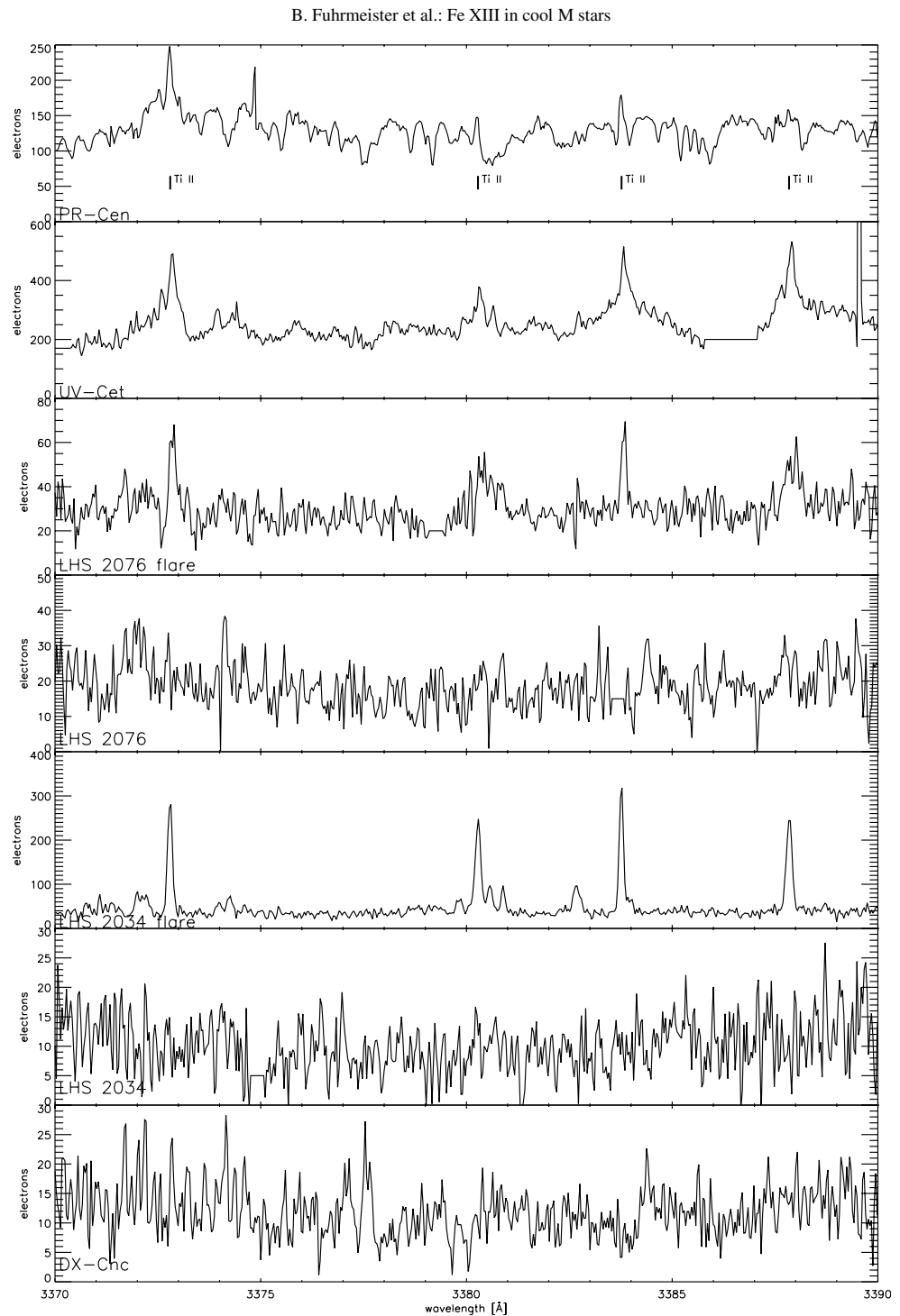


**Fig. 1.** continued. For LHS 2034 and LHS 2076 the spectra are shown during flare and during quiescent state. Note that these four spectra and the spectrum of UV Cet are not averaged spectra and therefore some remaining cosmoics were replaced manually by a straight line.

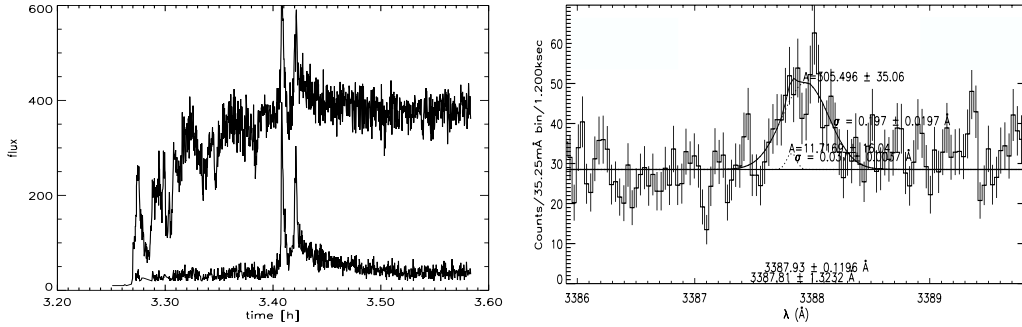


**Fig. 2.** To the left the light curve of the flux of LHS 2076 on March, 15th, corresponding to a single spectrum. On the  $x$ -axis the universal time is given. The flux is in arbitrary units since the photometer is used for engineering purposes. The upper light curve corresponds to the red arm of the spectra, while the lower light curve corresponds to the blue arm and is scaled relative to the red flux for convenience. Two short duration flares can be seen in both the red and the blue arm of the photometer following each other rapidly. To the right the spectrum of LHS 2076 during the flare around 3388 Å showing a broad emission feature at 3387.92 Å.

**Table 2.** Rotational velocities for (some of) our program stars. LHS 428 is omitted because it is a double star and could not be separated. LHS 6158 even seems to be a triple system. GJ 229A is saturated in the red arm. Prox Cen was used as template for UV Cet, FN Vir and GL Vir in the blue arm. All measurements in  $\text{km s}^{-1}$ .

star	$v \sin i$		literature
	red arm	blue arm	
AD Leo	$7.6 \pm 1.2$		$6.2 \pm 0.8^1$
AT Mic	$11.7 \pm 0.9$		
YZ CMi	$6.7 \pm 0.6$		$7.0 \pm 2.0^2, 6.5 \pm 1.1^1$
FN Vir	$17.4 \pm 1.4$	$13.1 \pm 3.7$	$16.8 \pm 2.1^1$
GL Vir	$15.3 \pm 0.8$	$16.0 \pm 2.0$	$9.2 \pm 1.9^1$
UV Cet B			$32.5 \pm 2.0^2$
UV Cet A	–	$25.9 \pm 8.6$	
DX Cnc	$8.9 \pm 0.8$		$11.0 \pm 2.0^2, 8.1 \pm 1.1^1$
LHS 2034	$7.9 \pm 2.8$		

<sup>1</sup> Delfosse et al. (1998).

<sup>2</sup> Mohanty & Basri (2003).

### 5.1. CN Leo

We report a clear detection of the Fe XIII line for CN Leo, which is also found to be variable on a timescale of hours, as will be discussed in Sect. 6. Thus the Fe XIII line detection of Schmitt & Wichmann (2001) is fully confirmed.

### 5.2. LHS 2076

A clear detection of the Fe XIII 3388.1 Å emission line has been obtained during a flare on LHS 2076. LHS 2076 is a double star known for its flare activity and separated by  $3''.4$  with both components being late-type (Pettersen 1985). Our spectrum refers to one system component with some minor contribution from the second star. During the last of the four exposures on March, 15th a double-peaked flare can be recognized in the photometer light curve as shown in Fig. 2.

Outside the flare interval no significant Ti II emission is detectable in the spectra. The emission line properties of the flare spectrum are listed in Table 3. The emission feature at 3387 Å is quite broad and was fitted with a double line component with amplitude, central wavelength and  $FWHM$  for both components as free parameters. The other Ti II lines were fitted as single lines with all three parameters ( $\lambda_{\text{cen}}$ ,  $A$  and  $\sigma$ ) free. Inspecting the properties of these three Ti II lines (cf., Table 3) one finds that the fitted half widths of all three lines agree very well with each other as expected for lines from the same multiplet. The half width of the narrow component of the 3387 Å line also agrees well with the half widths of the three Ti II lines while the half width of the broad component is more than three times larger. We therefore conclude that the narrow component of the broad emission feature at 3387 Å must be the fourth Ti II line in the multiplet, while the broad component has to be identified with the Fe XIII line. Further evidence for this interpretation can be found from the lines' amplitudes. Atomic data available through the NIST atomic spectra database<sup>1</sup> for these lines predict equal relative intensities for the two lines at 3372.80 and 3383.77 Å and equal relative intensities for the two lines at 3380.28 and 3387.84 Å lowered by a factor of four compared to the former two lines. According to Table 3 the amplitudes of the 3372.80 and 3383.77 Å line agree to within the errors and the two other lines are weaker. Therefore the broad component cannot be attributed to Ti II since its amplitude is more than twice as large as that of the 3372.80 or 3383.77 Å lines. On the other hand, both amplitudes and half widths fit perfectly if the broad emission component is identified with the Fe XIII line; also, the fitted half widths agree very well with the half width determined for the Fe XIII line in the CN Leo time series (see Sect. 6). The central wavelength of the absolute line position is a bit on the blue side but well within the  $2\text{-}\sigma$  error, while the absolute positions of the three single fit Ti II lines seem to be slightly redshifted (but only to within  $1\text{-}\sigma$  error each). The 3387.84 Å Ti II line unfortunately has a large error in its central wavelength. Given this situation, we cannot draw

<sup>1</sup> Available via [http://physics.nist.gov/cgi-bin/AtData/main\\_asd](http://physics.nist.gov/cgi-bin/AtData/main_asd)

**Table 3.** Properties of the Ti II and the Fe XIII line during the flare on LHS 2076. Given are the amplitude (in electrons), the central wavelength and half width  $\sigma$  of each line for the best fit. For the 3380.28 Å line no error estimation for the half width was possible due to the low signal to noise ratio.

	Ti II (3372.80 Å)	Ti II (3380.28 Å)	Ti II (3383.77 Å)	Ti II (3387.84 Å)	Fe XIII (3388.1 Å)
amplitude	134.3 ± 19.2	67.3 ± 17.3	115.1 ± 17.3	11.7 ± 16.0	305.5 ± 35.1
central $\lambda$	3372.85 ± 0.05	3380.33 ± 0.15	3383.81 ± 0.04	3387.81 ± 1.3	3387.93 ± 0.1
$\sigma$	0.06 ± 0.01	0.06	0.05 ± 0.01	0.04 ± 0.01	0.20 ± 0.02

any meaningful conclusions about possible wavelength shifts and remark that during a flare line shifts frequently occur due to mass motions.

### 5.3. GL Vir

The continuum for GL Vir is low as for CN Leo, but unlike CN Leo the Ti II at 3380 Å line is barely detectable. Nevertheless there is a broad emission line at  $3387.81 \pm 0.14$  Å with a half width of 0.15 Å and an amplitude of  $141.7 \pm 28.9$  counts. If this emission is attributed to the Ti II line, the measured amplitude would contradict the atomic data, which predicts the same intensity as for the 3380 Å line (which is not seen at all, cf. Fig. 1). If, on the other hand, this feature is identified with the Fe XIII line, it is clearly blue shifted. Since the star is in a quiescent state (as can be seen from the light curve, which is not shown here) it is unlikely that a blue shift is caused by mass motions. However, the blue shift could alternatively be caused by absorption at the red wing of the Fe XIII line due to a Co I line at 3388.17 Å which is also seen in other spectra (see Fig. 1). More evidence for an interpretation involving the Fe XIII line can be gained from the amplitude of the 3383.71 Å line of  $65 \pm 15$  counts. The 3387 Å Ti II line should have a smaller amplitude according to the atomic data and the measured spectra of CN Leo. On the other hand, the half widths of the 3383.71 Å line ( $0.13 \pm 0.02$  Å) and of the 3387.81 Å line ( $0.15 \pm 0.01$ ) are consistent with each other. The Ti II line at 3372.73 Å is unfortunately too deformed to allow any conclusions on its half width or amplitude. Therefore the question arises whether the half widths of the two lines at 3383.71 Å and 3387.81 Å can be caused by rotation. The rotation velocity  $v \sin i$  for GL Vir was measured by Delfosse et al. (1998) as  $9.2 \pm 1.9$  km s<sup>-1</sup>, while we determined  $15.3 \pm 0.8$  km s<sup>-1</sup> (see Sect. 4). Thus, if our rotational velocity is correct, the half widths  $\sigma$  can be explained by rotational broadening, however, if  $v \sin i = 9.2$  km s<sup>-1</sup>, the measured half width is a somewhat too large to be explained by the rotation. So the data of GL Vir are not unambiguous.

### 5.4. LHS 2034

The flare star LHS 2034 was observed during a longer flare on March, 14th, lasting over half an hour as can be seen from the light curve of the photometer (not shown here). While only the very strongest chromospheric emission lines can be seen in quiescence, a multitude of emission lines becomes visible in the spectrum taken during flare maximum. Indeed, the flare spectrum of LHS 2034 is very similar to the spectrum

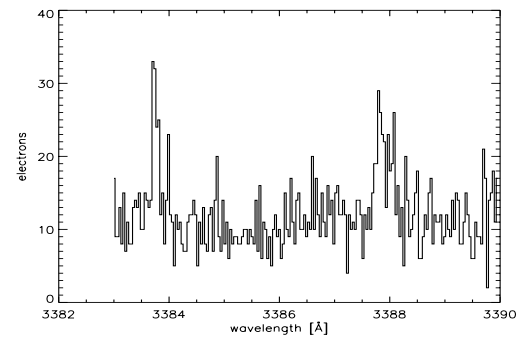


**Fig. 3.** Spectrum of CN Leo with a signal to noise ratio artificially reduced to that of DX Cnc. But despite the low signal to noise ratio clearly the Ti II and Fe XIII lines can be recognized.

of CN Leo with a rather flat continuum without strong absorption lines and dominated by strong chromospheric emission lines. Surprisingly, however, we did not find any evidence for Fe XIII emission in this spectrum. The same analysis procedure as applied for LHS 2076 was used for the flare spectrum of LHS 2034. All four Ti II lines are found to have about the same *FWHM* as expected but also the same amplitude contrary to expectation from atomic data and what was found for CN Leo and LHS 2076. This fact remains unexplained. In particular, we cannot attribute – as in LHS 2076 – the excess emission to Fe XIII, since this would contradict the measured *FWHM*. Obviously, efficient chromospheric heating of LHS 2034 does occur during the flare, but the corona is either not hot enough or too hot for producing a detectable Fe XIII line flux.

### 5.5. DX Cnc and LHS 292

These two stars and LHS 2034 are the latest-type stars in the sample and have a very low signal to noise ratio (which applies for the quiescent spectrum for LHS 2034 as well) which can cause the non detection of Fe XIII. In order to answer this question we took the spectrum of CN Leo as a template and reduced it to the lower signal to noise ratio found in our DX Cnc and the quiescent LHS 2034 spectra. The results of this exercise for DX Cnc are shown in Fig. 3. Clearly the Ti II and Fe XIII lines can be recognized in this example. Carrying out a larger number of such simulations we found that the Fe XIII need not always be recognisable, but the Ti II line should always be found in lower SNR spectra. Thus the level of activity in these stars must be lower making the persistent presence of the Fe XIII line unlikely.

**Table 4.** Properties of the Ti II of UV Cet measured with CORA using a broad and a narrow component simultaneously. Given are always the values for the narrow (first) and the broad component (second).

	Ti II (3372.80 Å)	Ti II (3380.28 Å)	Ti II (3383.77 Å)	Ti II (3387.84 Å)
amplitude	380 and 2416	329 and 1394	662 and 4665	520 and 5393
central $\lambda$	3372.80	3380.31	3383.82	3387.88
$\sigma$	0.04 and 0.23	0.05 and 0.30	0.07 and 0.53	0.05 and 0.46

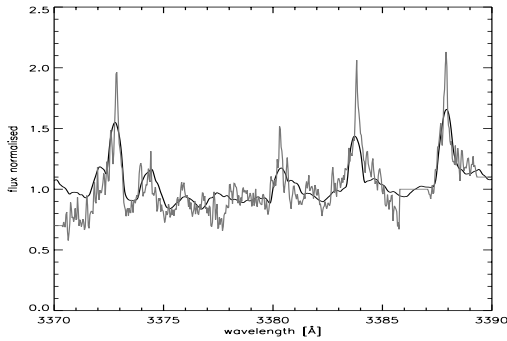


**Fig. 4.** The spectrum of UV Cet 3388.1 Å (grey) in comparison to the spectrum of CN Leo (black) broadened artificially to the rotational velocity of UV Cet.

### 5.6. UV Cet

UV Cet is a binary flare star well known from the radio to X-ray band (Stepanov et al. 1995) and has been resolved in the X-ray for the first time only recently (Audard et al. 2003). Our UVES spectrum was taken with both components in the slit, but we were unable to resolve the spectra of the two stars (due to the seeing). Therefore the spectrum should be dominated by the brighter A-component. The emission lines seen in the spectrum of UV Cet seem to have superimposed a second component of narrow emission lines which are slightly redshifted. We tentatively interpret this second set of emission lines as an active chromospheric region occupying only a part of the stars surface, since it is too narrow to be ascribed to the second component of the binary system.

Searching for the Fe XIII line we compared the broad component of the spectrum of UV Cet with an artificially broadened spectrum of CN Leo (see Fig. 4). The Fe XIII line disappears in the broadened spectrum since it becomes totally blended with the Ti II line at 3387.84 Å. Therefore a detection of the Fe XIII line in the UV Cet spectrum can only be obtained through indirect reasoning as follows: first, the broadened spectrum of CN Leo fits very well to the UV Cet spectrum in this wavelength region, although – admittedly – in other spectral regions there is less similarity. Second, we know from CN Leo and atomic data that the flux in the Ti II line at 3387.84 Å should be less than that contained in the 3372.80 Å line, but for UV Cet we find just the opposite. In order to determine line fluxes, we fitted each spectral line simultaneously with a narrow and a broad component (see Table 4). If the broad component comes from the whole surface of the star and the narrow component from an active region, the combined amplitudes must be considered and the combined amplitude of the 3387.84 Å line is higher than the amplitude of the 3372.80 Å line thus providing

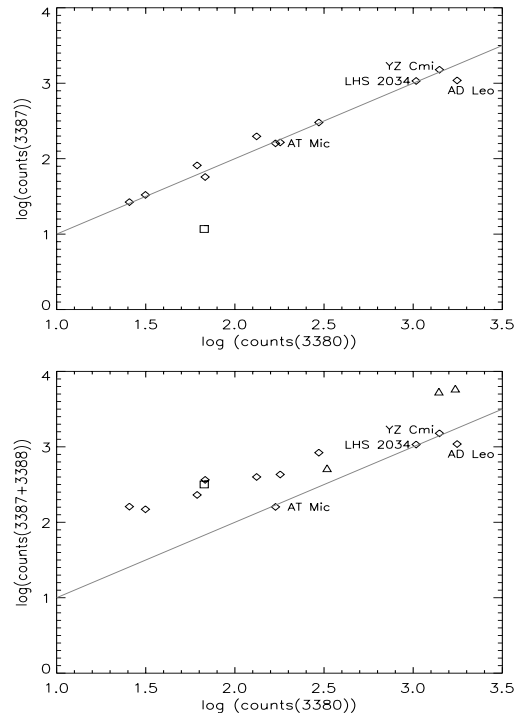


**Fig. 5.** *Top panel:* logarithm of the line flux (in electrons) of the 3387 Å line plotted versus the logarithm of the line flux of the 3380 Å line for the spectra of the CN Leo time series, LHS 2034, LHS 2076 during the flare, YZ CMi, AD Leo, AT Mic. The straight line marks the ratio of unity. The square marks the flux of LHS 2076 where the line is blended with Fe XIII and the fit cannot disentangle the two lines well. *Bottom panel:* logarithm of the combined flux of the 3387 Å and the Fe XIII line plotted versus the 3380 Å line. The triangles denote UV Cet with respect to the combined set of emission lines. Clearly AD Leo, AT Mic, YZ CMi and LHS 2034 show no Fe XIII line emission, while the UV Cet line ratios are in the regime of stars with additional Fe XIII flux (note, that the square denoting LHS 2076 has moved above the line of unity).

evidence of additional emission in the lines. The same applies for a comparison with the Ti II line at 3380.28 Å for which one expects equal flux ratios. If one plots the line ratios for the time series of CN Leo and other stars, one finds, that the UV Cet lines are the only one with a ratio that needs additional flux in the 3387.84 Å line (see Fig. 5). Given the high degree of activity on UV Cet it is suggestive to attribute this additional emission to the Fe XIII line, but given the complicated situation with the narrow and broad set of emission lines we consider the detection of Fe XIII in UV Cet as tentative.

### 5.7. AD Leo, AT Mic, YZ CMi, and FN Vir

For the other stars in our sample with spectral type M 4.5–M 6 the situation is not as clear due to the presence of two absorption lines at 3387.45 (Ni I) and 3388.17 (Co I) Å in the spectrum. This situation applies for the three stars AT Mic, YZ CMi and AD Leo: the Ti II lines at 3372, 3380 and 3383 Å have a width of about 0.05 Å whereas the line at 3387 Å shows a width of 0.1 Å. This can be due to the Fe XIII line blended by the absorption feature at 3388.17 Å, alternatively, leftover continuum may also be an explanation for the broader Ti II line since the spectra of the three stars do show many absorption lines. In order to test this hypothesis we used the spectrum of the earliest M dwarf GJ 229 as a template for the photospheric part of the spectrum applying the spun up and scaled spectrum as a “background” for the emission line fit with CORA. For the three stars AT Mic, YZ CMi and AD Leo this method yields a best fit with a narrow Ti II line of about 0.05 Å half width  $\sigma$ , consistent with the half width found for the other Ti II lines in these stars. The fitted spectra are displayed in Fig. 6. Therefore the apparent width of the 3387 Å line seems to be due to photospheric continuum and there is no need to invoke Fe XIII emission in these three stars.

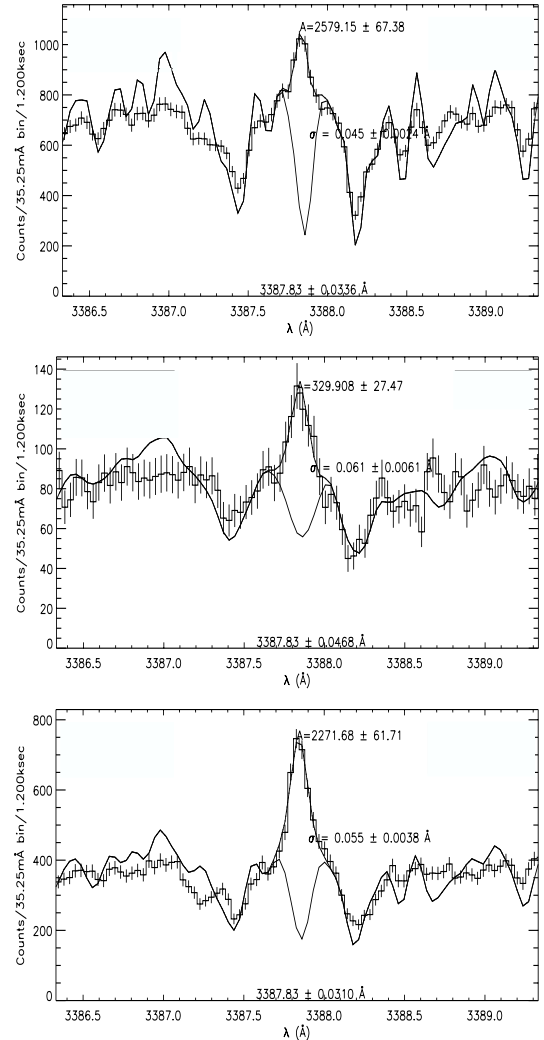
For the case of FN Vir this method cannot be used, because the template GJ 229 deviates significantly from the photospheric absorption lines seen in FN Vir. However, since the Ti II line at 3372 Å is found to have the same half width  $\sigma$  ( $0.11 \pm 0.01$  Å) as the 3387 Å line ( $0.12 \pm 0.01$  Å), there is again no need to invoke any Fe XIII emission for this star, either.

### 5.8. Proxima Centauri

For Proxima Centauri the Ti II lines are clearly seen in emission, but again the template GJ 229 deviates significantly if overlaid to the spectrum. In addition to this, the continuum is ill defined and therefore a fit of the line very difficult although especially the Ti II line at 3387 Å is clearly seen. Although the bump on the red side of the Ti II line at 3387.84 Å is somewhat suggestive of a Fe XIII emission line blended with the absorption line of Co I, this could also be due to leftover continuum. Since we were not able to obtain meaningful fits, the situation for Proxima Centauri must remain open and we must refrain from drawing any conclusions.

## 6. Timing behavior of the Fe XIII line in CN Leo

Every night during the observation run in March 2002 (with the exception of March, 14) two series of spectra were taken of CN Leo, each consisting of 3 spectra with 20 min exposure. On March, 14th only one spectral series of one hour duration was taken, one single spectrum taken about 2 h later was combined with the others to only one time series. We averaged the spectra of each series to improve the signal to noise ratio and constructed a total of 7 spectra of CN Leo. During the second spectral series on March, 16th a major flare occurred as can be seen in the photometer light curve in Fig. 7; on March, 14th CN Leo was very quiet, showing very little of the flickering seen in the light curves on the other days.

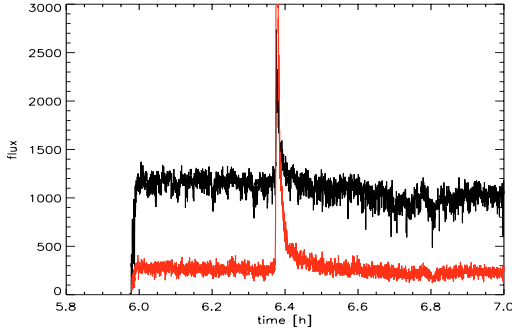


**Fig. 6.** The best fit of the 3387 Å line for the stars AD Leo, AT Mic and YZ CMi with the rotational broadened spectra of GJ 229 as background (black line).

We used the CORA line fitting program to measure the Ti II lines and the Fe XIII line fluxes as described in Sect. 5.2; a listing of our fit results can be found in Table 5. The Fe XIII line was detected in all spectra. However, for the spectrum taken on March, 16th during the flare the fit results are ambiguous. One can obtain a good fit with two narrow lines or a narrow and a broad line, where the broad line has nearly the same central wavelength like the narrow line (i.e. the Fe XIII line is blueshifted). We assume that the fit with the lineshift of the Fe XIII line is the correct one, since there is definitely a second line and a physical interpretation with two narrow lines one of which is ascribed to Fe XIII with a halfwidth  $\sigma$  of only 0.1 Å is not meaningful due to temperature broadening. Therefore a fit

**Table 5.** List of the line fluxes, central wavelength and half widths  $\sigma$  measured with CORA. Due to the signal to noise ratio the computation of the error of the half width could not be done for every line.

spectral block	Ti II (3372.80 Å)	Ti II (3380.28 Å)	Ti II (3383.77 Å)	Ti II (3387.84 Å)	Fe XIII (3388.1 Å)
2002-03-13 1st	137.7 ± 16.3	31.5 ± 9.6	83.2 ± 12.8	33.1 ± 10.4	115.6 ± 26.3
	3372.77 ± 0.05	3380.27 ± 0.04	3383.74 ± 0.04	3387.82 ± 0.02	3387.88 ± 0.17
	0.06 ± 0.01	0.03 ± 0.01	0.04 ± 0.01	0.02 ± 0.01	0.20
2002-03-13 2nd	290.1 ± 21.6	132.2 ± 16.0	215.4 ± 18.8	197.8 ± 21.6	201.0 ± 33.0
	3372.78 ± 0.04	3380.25 ± 0.04	3383.73 ± 0.03	3387.83 ± 0.03	3388.02 ± 0.09
	0.06 ± 0.01	0.05 ± 0.01	0.04 ± 0.01	0.05 ± 0.01	0.21
2002-03-14	161.5 ± 15.9	61.4 ± 12.6	122.9 ± 14.7	81.6 ± 16.2	148.8 ± 26.0
	3372.78 ± 0.03	3380.27 ± 0.05	3383.73 ± 0.04	3387.84 ± 0.05	3388.09 ± 0.26
	0.04 ± 0.01	0.05 ± 0.01	0.04 ± 0.01	0.05	0.30
2002-03-15 1st	576.4 ± 29.1	295.7 ± 23.4	490.6 ± 27.1	302.2 ± 28.1	535.1 ± 51.2
	3372.79 ± 0.03	3380.27 ± 0.03	3383.75 ± 0.03	3387.83 ± 0.03	3388.02 ± 0.09
	0.04 ± 0.01	0.04 ± 0.01	0.04 ± 0.01	0.04 ± 0.01	0.26 ± 0.02
2002-03-15 2nd	437.7 ± 24.8	179.6 ± 18.1	315.0 ± 21.8	164.5 ± 20.1	265.7 ± 39.0
	3372.80 ± 0.03	3380.27 ± 0.03	3383.76 ± 0.03	3387.82 ± 0.04	3388.19 ± 0.17
	0.04 ± 0.01	0.04 ± 0.01	0.04 ± 0.01	0.05 ± 0.01	0.30
2002-03-16 1st	205.6 ± 19.3	68.1 ± 12.5	122.8 ± 14.8	57.2 ± 14.3	307.6 ± 34.5
	3372.80 ± 0.05	3380.26 ± 0.03	3383.75 ± 0.03	3387.85 ± 0.03	3387.98 ± 0.17
	0.06 ± 0.01	0.03 ± 0.01	0.04 ± 0.01	0.03 ± 0.01	0.24 ± 0.02
2002-03-16 2nd	125.5 ± 15.3	25.6 ± 8.9	65.5 ± 10.8	26.6 ± 11.0	134.8 ± 26.6
	3372.82 ± 0.05	3380.28 ± 0.04	3383.76 ± 0.03	3387.84 ± 0.03	3387.88 ± 0.14
	0.06 ± 0.01	0.03 ± 0.01	0.02 ± 0.01	0.02 ± 0.01	0.20

**Fig. 7.** Light curve of the flux of CN Leo on March, 16th, during the second observation block but otherwise like in Fig. 2. Clearly a major flare can be seen in both the red and the blue arm of the photometer.

with two narrow lines implies that there is no Fe XIII present. This can be possible, when the Fe XIII is ionized to higher ionisation stages during the flare. This is quite unlikely though, since we find no Fe XIV emission at 5303 Å in CN Leo (see Sect. 8) even during the flare. Moreover the second emission line has to be explained otherwise. We favour therefore an interpretation with a narrow Ti II line and a broad blue shifted Fe XIII line. Line shifts are known to occur during flares, when the emitting material is raised in the atmosphere. The velocity towards the observer in the line of sight is about 20 km s<sup>-1</sup> in this case. A blueshifted Fe XIII line during the flare lines in

with the blueshift of the Fe XIII line we observed in LHS 2076 during the flare.

Although the photometer data for the spectra outside the major flare are rather constant, the corona must have undergone some variability as can be seen from Fig. 8, where the averaged spectra of each time series are shown. The Fe XIII line is most clearly seen in the spectrum of the first series taken on March, 15th, where the continuum is relatively high and the Ti II line is very intense, although in the photometer data no notable flux variability is seen besides the usual flickering. In the other spectra the line does not show that clearly, in fact the line would be undetectable if it were only a bit weaker or if one chose a higher background level. Thus even for CN Leo the Fe XIII line need not to be a persistent feature, and the high variability during quiescence is suggestive of the microflaring as proposed for the heating of stellar coronae (Kashyap et al. 2002). Also the chromospheric Ti II line shows major variability even on a timescale of hours. For example, on March 13th the amplitude of the Ti II lines increased by a factor of more than two over a time span of only two hours. Therefore also the chromosphere must have undergone rapid and large changes.

## 7. X-ray and Fe XIII line fluxes

Using the standard star HD 49798 for flux calibration, we measured absolute fluxes in the Fe XIII 3388.1 line for the stars CN Leo, GL Vir and for LHS 2076 (during the flare). Since the standard star was observed only once per night, we estimate an error in this absolute flux calibration up to a factor

B. Fuhrmeister et al.: Fe XIII in cool M stars

711

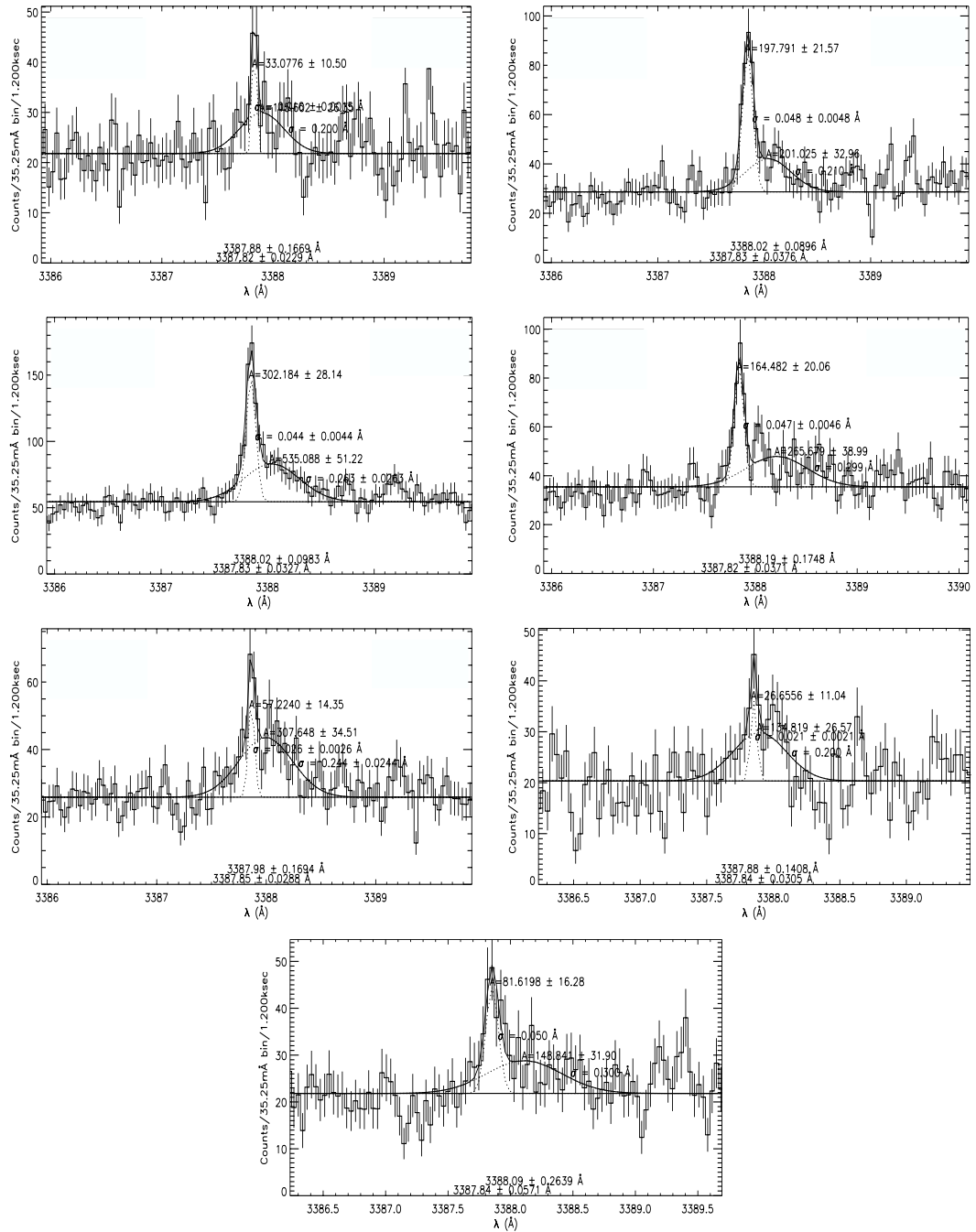


**Fig. 8.** Best fit of the Ti II line together with the Fe XIII line in the averaged spectral series. At the top the two spectra taken on March, 13th (left: start time 2.3 UT right: start time 4.2 UT), beneath the two spectra taken on March, 15th (left: start time 3.7 UT, right: start time 6.4 UT), beneath the spectra taken on March, 16th (left: start time 3.9 UT, right: start time 5.9 UT). The single spectrum at the bottom was taken on March, 14th (start time 3.1 UT). The horizontal line in each spectrum indicates the background used for the line fitting.

712

B. Fuhrmeister et al.: Fe XIII in cool M stars

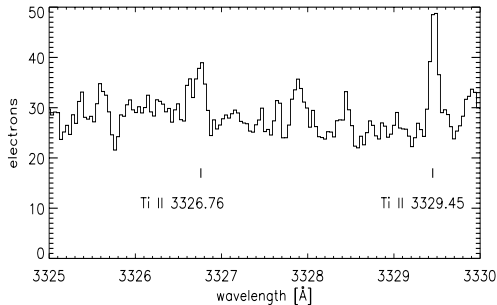


**Fig. 9.** The spectrum of CN Leo around the Ca XII line. Two Ti II lines are identified; the other faint emission features are unidentified.

of two. Broad band X-ray fluxes for these stars were obtained from broad band count rates and should have (systematic) errors of about 50%, resulting from the adopted count rate to energy flux conversion. Also note that for none of our stars do we have simultaneous optical and X-ray observations. The measured average fluxes for the one hour duration spectra of CN Leo range from  $3.2 \times 10^{-15} \text{ cm}^{-2} \text{ s}^{-1}$  in the first spectrum taken on 2002-03-13 to  $1.4 \times 10^{-14} \text{ erg cm}^{-2} \text{ s}^{-1}$  in the first spectrum on 2002-03-15. For the Fe XIII line flux of GL Vir we computed  $3.9 \times 10^{-15} \text{ erg cm}^{-2} \text{ s}^{-1}$ , and for the flare spectrum of LHS 2076 the measured flux is  $9.8 \times 10^{-15} \text{ erg cm}^{-2} \text{ s}^{-1}$ . Using distances of 2.4 pc for CN Leo 6.5 pc for GL Vir and 5.2 pc for LHS 2076 (Oppenheimer et al. 2001) these fluxes result in line luminosities of  $2.0 \times 10^{24}$  up to  $9.6 \times 10^{24} \text{ erg s}^{-1}$  for CN Leo,  $1.9 \times 10^{25} \text{ erg s}^{-1}$  for GL Vir and  $3.2 \times 10^{25} \text{ erg s}^{-1}$  for LHS 2076. Comparing these numbers with the non-simultaneously measured X-ray luminosities one then finds a ratio of broad band X-ray to line luminosity in the range 3012 to 628 for CN Leo, 235 for GL Vir and of 124 for LHS 2076.

If one takes CN Leo as a prototype showing Fe XIII emission the ratios of GL Vir and LHS 2076 are too low. However, for LHS 2076 the Fe XIII was measured during a flare, while the X-ray luminosity was measured during quiescence and is therefore presumably too low leading to an incorrect (lower) ratio. In the case of GL Vir the line was measured during quiescence and the low ratio adds therefore to the interpretation, that the line is actually the Ti II line broadened by the higher rotation rate we found for GL Vir.

### 8. Search for other forbidden coronal lines in CN Leo

After the detection of the Fe XIII line in CN Leo the question arises if there is evidence for other forbidden coronal lines. A catalog of such lines can be found e.g. in Allen (1973). Out of this we investigated the following two lines more closely: Ca XII at 3327 Å and Fe XIV at 5303 Å.

Using the CHIANTI software package (Young et al. 2003) we computed emissivity ratios for the lines mentioned above to the Fe XIII line, which are proportional to the flux ratios of the lines. All computations were done assuming solar photospheric abundances since we do not know anything specific about the coronal abundances of very low mass stars. The

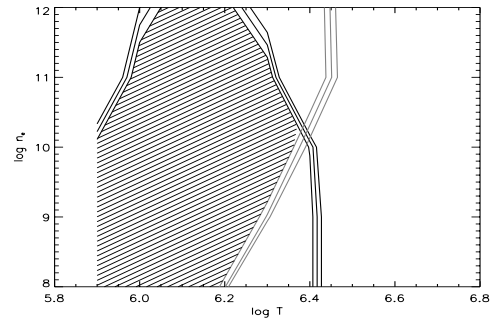


**Fig. 10.** Contour plot of the flux ratios between the Ca XII and the Fe XIII line (black) for a set of temperatures and electron densities and for the ratios of the Fe XIV and the Fe XIII line (grey). The inner line represents a ratio of 0.4, the middle line a ratio of 0.5 and the outer line a ratio of 0.6 for Ca XII and for Fe XIV the inner line represents a ratio of 5.0, the middle line a ratio of 5.5 and the outer line a ratio of 6.0. The shaded area denotes the parameter set that is in agreement with the non-detection of Ca XII and Fe XIV.

ionisation balance was computed using the ionisation ratios found by Mazzotta et al. (1998). The computed flux ratios proved to be quite sensitive on the ionisation balance whose choice can influence the computed flux ratios by more than a factor of two while the chosen abundances have less influence.

#### 8.1. Analysis of the Ca XII line

A plot of the region around the Ca XII line is shown in Fig. 9. Besides the two Ti II lines the other faint emission features are unidentified, but none of them is likely to be caused by Ca XII because the line width is too narrow for a line formed at temperatures of about  $\log T \sim 6$  for which one would expect a halfwidth of 0.2 Å. While a line consisting of 50 counts and a halfwidth of 0.2 Å can easily be hidden in the spectrum a line with 100 counts should be possible to detect. This leads to restrictions for the possible temperatures and densities. Since we measured 200 counts in the Fe XIII line at 3388 Å for CN Leo averaging all our spectra, the highest possible ratio between the two lines that is in agreement with a non-detection is about 0.5, which excludes temperatures higher than  $\log T = 6.4$  and lower than  $\log T = 6.0$ . A more detailed discussion is given in the next subsection together with the restrictions drawn from Fe XIV.

#### 8.2. Analysis of the Fe XIV line

We carefully searched for the Fe XIV line at 5303 Å. Since the line could be hidden in the molecular lines dominating this wavelength region we compared the CN Leo spectra to each other and to the LHS 2034 averaged spectrum, assuming that this star does not display the Fe XIV line. But no significant difference could be found. Therefore we conclude, that no Fe XIV emission can be seen in CN Leo.

Out of the absence of the Fe XIV and the Ca XII emission lines the possible temperatures and densities can be estimated. To be in agreement with a non-detection for the Ca XII line the

flux ratio must be lower than about 0.5 and for the Fe XIII lower than about 5.5. In Fig. 10 a contour plot of the ratio between the Ca XII and the Fe XIII and the Fe XIV and the Fe XIII line is given. From this plot one can exclude temperature lower than  $\log T = 6.0$  and higher than  $\log T = 6.2$  for low densities,  $\log T = 6.3$  for higher densities and  $\log T = 6.4$  for very high densities. Therefore the line formation of the Fe XIII line takes place around the peak formation temperature of  $\log T = 6.2$  – what would be expected from the beginning. For the densities the plot is not very restrictive. Even densities as high as  $N_e = 10^{12} \text{ cm}^{-3}$  can be possible if the temperature is close enough to the peak formation temperature.

## 9. Discussion and conclusions

Our study reveals high and rapid variability of the Fe XIII line on the two stars CN Leo and LHS 2076. While the former seems to have coronal temperatures high enough even in its quiescent state to show the Fe XIII line, the latter does not.

In addition to these two absolutely secure detections GL Vir and UV Cet may exhibit the Fe XIII line, too. For Prox Cen the situation is unclear. In the stars AD Leo, AT Mic, YZ CMi and FN Vir no Fe XIII line could be found. In the stars DX Cnc, LHS 292 and the quiescent LHS 2076 no Fe XIII line could be found as well. That may be due to the low signal to noise ratio but simulation strongly suggest that these stars are not active enough to show the Fe XIII line. Rather surprisingly no Fe XIII line could be found in the flaring LHS 2034, either. So there are at most four detections of Fe XIII in a sample of 16 or 13 stars, respectively if one does not count the two double stars LHS 428 and LHS 6158 and the template GJ 229A. This might seem not very much at first glance since all are very active stars. However, one of the the goals of the project was to observe a wide range of spectral types to determine for which stars a detection of Fe XIII is feasible at all. And if the case of LHS 2076 applies to the other stars as well and the corona is only hot enough to show the Fe XIII line during major flares we would not expect one more detection, since LHS 2034 showed a flare, too. But in contrast to the two flares on CN Leo and LHS 2076 this was a long duration flare, whose decays lasted longer than half an hour and we would expect different behavior of the spectral lines in the course of such a different type of flare.

Moreover the Fe XIII line may have been detected for some of the stars with a better signal to noise ratio. This can be estimated for AD Leo where from EUVE observations a flux at Earth of  $2.69 \times 10^{-4} \text{ photons cm}^{-2} \text{ s}^{-1}$  has been measured for the 203.83 Å line of Fe XIII (Sanz-Forcada & Micela 2002). Using atomic data from the CHIANTI database (Young et al. 2003), we compute a flux ratio of the two lines of  $\frac{F_{3388}}{F_{203}} = 0.02 \dots 0.05$  assuming coronal densities in the range of  $10^8$  up to  $10^{10} \text{ cm}^{-3}$  and temperatures in the range of 1 up to  $2 \times 10^6 \text{ K}$ . This translates into a line flux of  $5.2 \times 10^{-16} \dots 1.3 \times 10^{-15} \text{ erg cm}^{-2} \text{ s}^{-1}$  in the Fe XIII line at 3388 Å, which in turn would correspond to an amplitude of at most 26 counts in this line (for a 0.3 h integration, which is the typical exposure time for all of our spectra); clearly, such flux levels can easily be hidden in the spectrum. If the Fe XIII line at 203.83 Å is blended with other iron lines

the expected amplitude would be even less. Therefore data with much better signal to noise are required to settle this question.

CN Leo is unique in the sample when it comes to clear exhibition of the Fe XIII line in quiescent state, which we ascribe to a high level of microflaring, since the coronal line is quite variable. This variability of the corona while the photospheric flux measured with the photometer is quite constant calls for a parallel observation in X-rays with Chandra or XMM-Newton, since the coronal variability should lead to X-ray variability. This high level of variability in the basic coronal emission is surprising, but it finds its counterpart in the high level of chromospheric emission in the hydrogen emission lines of the Balmer series which are clearly seen up to H<sub>24</sub>. This is in contrast to the Sun where even in flares the Balmer lines are only excited up to H<sub>16</sub> (Švestka 1972).

Though the variability of Fe lines for the Sun was studied extensively in X-ray wavelengths by the satellites SOHO and TRACE the variability of the emission in Fe XIII lines was not studied to our knowledge, yet. However for the forbidden optical green Fe XIV line at 5303 Å there are measurements by the SOHO instrument LASCO (Large Angle Spectrometric Coronagraph) (Wood et al. 1998). Observing quiescent coronal limb structures Wood et al. found statistically significant quasi-steady brightening on timescales of at least an hour. This is about the same timescale on which we observed the fading of the Fe XIII line in CN Leo on March, 15th from a very pronounced to a barely detectable line profile, which took less than three hours.

*Acknowledgements.* We thank Dr. Jan-Uwe Ness supplying to us his CORA line fitting program and providing technical support.

## References

- Allen, C. W. 1973, University of London (The Athlone Press)  
 Audard, M., Güdel, M., & Skinner, S. L. 2003, *ApJ*, 589, 983  
 Berger, E. 2002, *ApJ*, 572, 503  
 Delfosse, X., Forveille, T., Perrier, C., & Mayor, M. 1998, *A&A*, 331, 581  
 Flower, D. R., & Pineau des Forets, G. 1973, *A&A*, 24, 181  
 Güdel, M. 2002, *ARA&A*, 40, 217  
 Hüensch, M., Schmitt, J. H. M. M., Sterzik, M. F., & Voges, W. 1999, *A&AS*, 135, 319  
 Kashyap, V. L., Drake, J. J., Güdel, M., & Audard, M. 2002, *ApJ*, 580, 1118  
 Mazzotta, P., Mazzitelli, G., Colafrancesco, S., & Vittorio, N. 1998, *A&AS*, 133, 403  
 Mohanty, S., & Basri, G. 2003, *ApJ*, 583, 451  
 Ness, J.-U., & Wichmann, R. 2002, *AN*, 323, 129  
 Oppenheimer, B. R., Golimowski, D. A., Kulkarni, S. R., et al. 2001, *AJ*, 121, 2189  
 Pettersen, B. R. 1985, *A&A*, 148, 151  
 Sanz-Forcada, J., & Micela, G. 2002, *A&A*, 394, 653  
 Schmitt, J. H. M. M. 1997, *A&A*, 318, 215  
 Schmitt, J. H. M. M., Fleming, T. A., & Giampapa, M. S. 1995, *ApJ*, 450, 392  
 Schmitt, J. H. M. M., & Liefke, C. 2002, *A&A*, 382, L9  
 Schmitt, J. H. M. M., & Wichmann, R. 2001, *Nature*, 412, 508  
 Stepanov, A. V., Fuerst, E., Krueger, A., et al. 1995, *A&A*, 299, 739  
 Švestka, Z. 1972, *ARA&A*, 10, 1  
 Wood, B. E., Karovska, M., Cook, J. W., et al. 1998, *ApJ*, 505, 432  
 Young, P. R., Del Zanna, G., Landi, E., et al. 2003, *ApJS*, 144, 135



## **Chapter 3**

# **Detection and high-resolution spectroscopy of a huge flare on the old M9 dwarf DENIS 104814.7-395606.1**

**B. Fuhrmeister and J. H. H. M. Schmitt**  
**Astronomy & Astrophysics, 420, 1079 (2004)**



A&A 420, 1079–1085 (2004)  
 DOI: 10.1051/0004-6361:20035644  
 © ESO 2004

**Astronomy  
&  
Astrophysics**

## Detection and high-resolution spectroscopy of a huge flare on the old M 9 dwarf DENIS 104814.7-395606.1<sup>★</sup>

B. Fuhrmeister and J. H. M. M. Schmitt

Hamburger Sternwarte, University of Hamburg, Gojenbergsweg 112, 21029 Hamburg, Germany

Received 7 November 2003 / Accepted 14 March 2004

**Abstract.** We report a flare on the M 9 dwarf DENIS 104814.7-395606.1, whose mass places it directly at the hydrogen burning limit. The event was observed in a spectral sequence during 1.3 h. Line shifts to bluer wavelengths were detected in  $H_{\alpha}$ ,  $H_{\beta}$ , and in the Na I D lines, indicating mass motions. In addition we detect a flux enhancement on the blue side of the two Balmer lines in the last spectrum of our series. We interpret this as rising gas cloud with a projected velocity of about  $100 \text{ km s}^{-1}$  which may lead to mass ejection. The higher Balmer lines  $H_{\gamma}$  to  $H_{\delta}$  are not seen due to our instrumental setup, but in the last spectrum there is strong evidence for  $H_{\gamma}$  being in emission.

**Key words.** stars: activity – stars: flare – stars: late-type

### 1. Introduction

DENIS 104814.7-395606.1 (hereafter DENIS 1048-39) was discovered in the DEep Near Infrared Survey (DENIS), which covered the southern sky (Epchtein 1997) in two near infrared bands ( $J$  and  $K_s$ ) and one optical band ( $I$ ). With this choice of bands DENIS is very sensitive to very low mass stars and brown dwarfs and thus excellently suited for searches for hitherto unknown low mass stellar or substellar objects in the solar vicinity. With a distance of only  $4.6 \pm 0.3 \text{ pc}$  (Neuhäuser et al. 2002) DENIS 1048-39 is extremely close to the Sun. Classified as an M 9 star, the lithium resonance line at  $6708 \text{ \AA}$  could not be detected, therefore substantial lithium depletion must have taken place (Delfosse et al. 2001). Compared to LP 944-20, which is also classified as M 9, DENIS 1048-39 should be older and more massive. Theoretical models place DENIS 1048-39 directly at the hydrogen burning boundary with an estimated mass of  $0.075$  up to  $0.09 M_{\text{Sun}}$  and an age of  $1\text{--}2 \text{ Gyr}$  (Neuhäuser et al. 2002) assuming a solar chemical composition. Thus DENIS 1048-39 may either be among the most massive brown dwarfs or among the least massive stars.

Interestingly, the  $H_{\alpha}$ -line was found to be variable (Delfosse et al. 2001), implying that DENIS 1048-39 exhibits activity despite its old age and low mass. There are only a few very late type objects showing strong and persistent  $H_{\alpha}$  emission.  $H_{\alpha}$  emission, a well established activity indicator, is not detected in the majority of these objects. Instead one observes a steep decline of the strength of  $H_{\alpha}$  emission for stars later

than spectral type M 7. This effect shows up in smaller equivalent widths (EW) of the  $H_{\alpha}$  line for these objects. However, since the  $H_{\alpha}$  line is seen against an increasingly faint photosphere for later objects, a better activity indicator is the ratio of the  $H_{\alpha}$  luminosity to the bolometric luminosity. This ratio was found to drop in only three subclasses (M 8-L 1) by one order of magnitude (Gizis et al. 2000). The same authors also found that the activity of these late type objects is primarily related to temperature and shows only a secondary dependence on mass and age. Thus strong  $H_{\alpha}$  emission does not necessarily imply youth; on the contrary, strong  $H_{\alpha}$  emitters in the field are more likely to be old.

Despite this decline in activity there are many reports of flare activity even among L dwarfs. For very late-type M dwarfs Gizis et al. (2000) estimated a flaring time fraction of about 7%, while Liebert et al. (2003) found a flare duty cycle of about 1% for L dwarfs, suggesting that there must be some ongoing magnetic activity in these dwarfs despite the absence of a persistent chromosphere or corona.

In this paper we report on a huge flare on DENIS 1048-39 detected in the  $H_{\alpha}$ ,  $H_{\beta}$ , and sodium emission lines. In Sect. 2 we describe the VLT data and their analysis, in Sect. 3 we discuss the timing behaviour of the flare.

### 2. Observations and data analysis

The observations reported in this paper were carried out with ESO's Kueyen telescope at Paranal equipped with the Ultraviolet-Visual Echelle Spectrograph (UVES) on March, 14th, 2002. Four spectra of DENIS 1048-39 were taken in sequence, each with an exposure time of 1200 s. The individual observations started at 04:12:46, 04:33:43, 04:54:40 and

Send offprint requests to: B. Fuhrmeister,  
 e-mail: bfuhrmeister@hs.uni-hamburg.de

<sup>★</sup> Based on observations collected at the European Southern Observatory, Paranal, 68.D-0166A, Chile.

1080

B. Fuhrmeister and J. H. M. M. Schmitt: Flare on DENIS 104814.7-395606.1

05:22:40 UT. The instrument was operated in dichroic mode, yielding 33 echelle orders in the blue arm (spectral coverage from 3030 to 3880 Å) and 39 orders in the red arm (spectral coverage from 4580 to 6680 Å) with a typical resolution of  $\sim 45\,000$ . The red part of the spectrum was recorded on two separate CCDs; therefore there is a spectral gap from  $\sim 5640$  to  $5740$  Å resulting from the spatial separation of the CCDs. As a consequence of the dichroic mode used we did not cover the lines from H<sub>3</sub> up to H<sub>8</sub> of the Balmer series, nor the Ca II H and K lines.

The data were reduced using IRAF. The wavelength calibration was carried out with thorium-argon spectra with an accuracy of  $\sim 0.03$  Å in the blue arm and  $\sim 0.05$  Å in the red arm.

The fitting of the spectral lines was carried out with the CORA fit program (Ness & Wichmann 2002), kindly provided to us by Dr. Jan-Uwe Ness and originally developed for analyzing high resolution X-ray spectra. The fit algorithms employed by CORA are also well suited for a modeling of all types of emission lines with count statistics. CORA uses a maximum likelihood method for the fitting of line profiles. It contains a number of tools for modeling blended lines, allowing the user to specify the number of lines to be modeled, whether the line shapes should be individually fitted or fitted with a fixed line profile, and whether the line centroids are allowed to vary freely or are fixed with respect to each other. The program also provides an accurate error analysis.

### 3. The UVES spectrum of DENIS 1048-39

#### 3.1. Emission line variability

In our UVES spectra of DENIS 1048-39 we find three prominent emission lines in the red part of the spectra, which can be clearly identified as H <sub>$\alpha$</sub> , H <sub>$\beta$</sub> , and the Na I D doublet at 5889 and 5895 Å. In Figs. 1–3 we plot the spectral region around H <sub>$\alpha$</sub> , H <sub>$\beta$</sub> , and the Na I D for the four individual spectra. In order to facilitate the comparison between the spectra we also plot the averaged spectrum as a dotted line. Note that the spectra are not (yet) shifted to the star's rest frame.

In the spectral sequence of our VLT observations a clear intensity increase as well as a blue shift of the H <sub>$\alpha$</sub>  and H <sub>$\beta$</sub>  lines is seen. In the last spectrum of our series an extremely broad emission feature appears, centered at about 6560.5 Å on the blue side of the H <sub>$\alpha$</sub>  line. A similar emission feature appears for the H <sub>$\beta$</sub>  line centered at about 4860 Å. If interpreted as Doppler shift, this would imply emission from material moving with a velocity of  $100\text{ km s}^{-1}$  towards the observer.

For the Na I D lines the flux is not constant, but no clear trend can be seen. The stellar Na I D lines are heavily blended with terrestrial airglow lines of Na I D; in addition, there are further airglow lines in this spectral region at 5888.19 Å and 5894.47 Å, well known to occur in the UVES instrument (Hanuschik 2003). The blue shift of the stellar Na I D lines can be unambiguously seen, when the stellar Na I D line peak moves out of the stationary airglow lines in the last spectrum. We therefore conclude that the recorded line shifts cannot be due to incorrect wavelength calibrations.

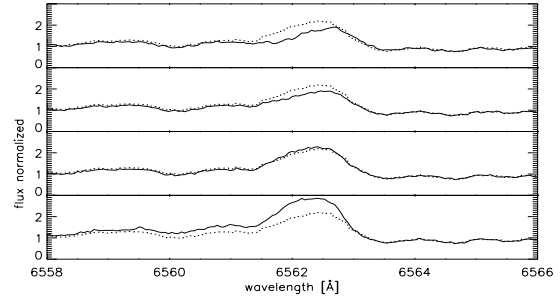


**Fig. 1.** Time series of the H <sub>$\alpha$</sub> -line first spectrum at the top, last spectrum at the bottom. The dotted spectrum is the time averaged spectrum of DENIS 1048-39. Notice the gradual increase and blue shift of the line; in the last spectrum a broad feature is seen to emerge on the blue side of the line centered on about 6560.5 Å.

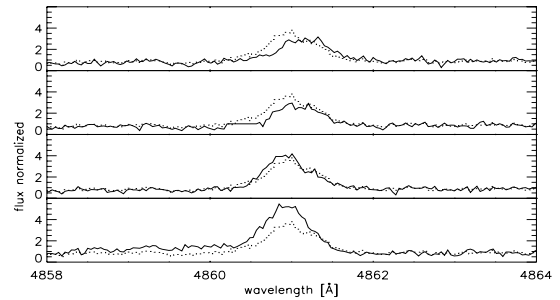


**Fig. 2.** Time series of the H <sub>$\beta$</sub> -line as in Fig. 1. Again a blue shift of the line can be seen as well as a broad emission feature at the blue side of the line in the last spectrum. In the spectra some cosmics were replaced manually by a horizontal line. The dotted line is again the time averaged spectrum.

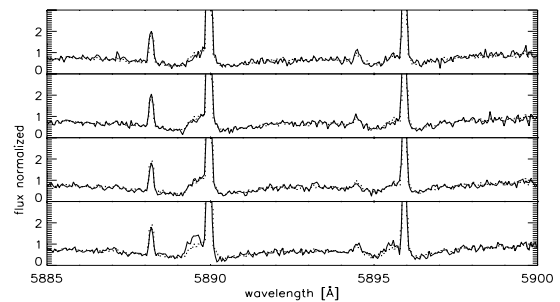


**Fig. 3.** Time series of the Na I D lines as in Fig. 1. The dotted line denotes again the time averaged spectrum. Note the blue shift that can be seen in comparison to the airglow Na I D lines especially in the last spectrum, where the peak of the stars Na I D lines moves out of the airglow lines.

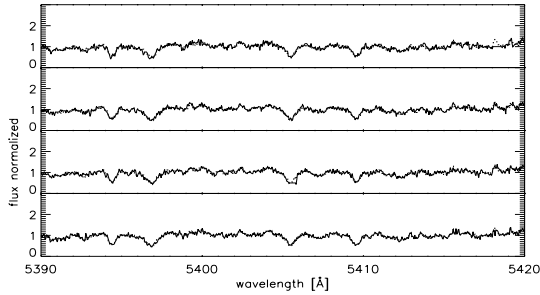
In Fig. 4 we plot the time series of the spectrum between 5390 Å–5420 Å, which is purely of photospheric origin. This spectral region obviously remains constant and thus the photospheric continuum appears to be unaffected by the flaring emission lines.

B. Fuhrmeister and J. H. M. M. Schmitt: Flare on DENIS 104814.7-395606.1

1081

**Table 1.** Properties of the Na I D lines determined from fitting the Na I D airglow line and the star's Na I D line simultaneously. Quoted are all free fit parameters and the line shift of the star's Na I D line. Due to the heavy blending the error estimation of the half width could not be done for each spectrum.

		Star	Airglow	Star	Airglow
1st spectrum	$\lambda_{\text{cen}} [\text{\AA}]$	$5890.00 \pm 0.04$	$5890.19 \pm 0.02$	$5895.96 \pm 0.03$	$5896.17 \pm 0.02$
	$\sigma [\text{\AA}]$	$0.30 \pm 0.03$	$0.05 \pm 0.01$	0.25	$0.05 \pm 0.01$
	Amplitude [electrons]	$1920 \pm 73$	$5890 \pm 85$	$1225 \pm 65$	$3665 \pm 69$
	Line shift [ $\text{km s}^{-1}$ ]	$2.5 \pm 2.0$		$1.8 \pm 1.1$	
2nd spectrum	$\lambda_{\text{cen}} [\text{\AA}]$	$5889.97 \pm 0.03$	$5890.20 \pm 0.03$	$5895.91 \pm 0.04$	$5896.16 \pm 0.02$
	$\sigma [\text{\AA}]$	$0.28 \pm 0.01$	$0.06 \pm 0.01$	$0.24 \pm 0.02$	$0.06 \pm 0.01$
	Amplitude [electrons]	$2110 \pm 74$	$5258 \pm 82$	$942 \pm 60$	$3359 \pm 66$
	Line shift [ $\text{km s}^{-1}$ ]	$1.0 \pm 1.5$		$-0.71 \pm 2.0$	
3rd spectrum	$\lambda_{\text{cen}} [\text{\AA}]$	$5889.92 \pm 0.02$	$5890.20 \pm 0.01$	$5895.86 \pm 0.05$	$5896.17 \pm 0.01$
	$\sigma [\text{\AA}]$	$0.24 \pm 0.01$	$0.06 \pm 0.01$	0.19	$0.06 \pm 0.01$
	Amplitude [electrons]	$2316 \pm 73$	$5208 \pm 81$	$811 \pm 54$	$3475 \pm 66$
	Line shift [ $\text{km s}^{-1}$ ]	$-1.5 \pm 1.0$		$-3.3 \pm 2.5$	
4th spectrum	$\lambda_{\text{cen}} [\text{\AA}]$	$5889.76 \pm 0.04$	$5890.19 \pm 0.02$	$5895.78 \pm 0.07$	$5896.17 \pm 0.02$
	$\sigma [\text{\AA}]$	$0.19 \pm 0.01$	$0.06 \pm 0.01$	$0.14 \pm 0.01$	$0.05 \pm 0.01$
	Amplitude [electrons]	$2273 \pm 62$	$5069 \pm 76$	$832 \pm 47$	$2977 \pm 60$
	Line shift [ $\text{km s}^{-1}$ ]	$-9.7 \pm 2.0$		$-7.3 \pm 3.6$	

**Fig. 4.** Timeseries of a spectral range with several metal absorption lines. Clearly these photospheric lines are not affected by the blue shift seen in the chromospheric emission lines. Two cosemics were removed manually by a horizontal line. The four pronounced absorption lines are due to Mn I (5394 Å), Fe I (5397 and 5405 Å) and Cr I (5409 Å). Again the dotted line denotes the time averaged spectrum.

### 3.2. Radial and rotational velocity

Having confirmed that the absorption lines are not affected by any blue shifts, we measured the radial velocity of the star to be  $-9.6 \pm 2.0 \text{ km s}^{-1}$  in agreement with the value of  $-10.1 \pm 0.5 \text{ km s}^{-1}$  found by Delfosse et al. (2001). All line fitting with CORA was done after shifting the spectra to the rest frame. In addition to the radial velocity we also measured the rotational velocity of DENIS 1048-39 using 7 apertures in the red arm of the spectrum without any emission and airglow lines. We used the spectrum of the M9 star LHS 2065 (taken during the same observation run) as a template and convolved it with rotational velocities from 3 up to  $40 \text{ km s}^{-1}$ . The best rotational fit of the spun-up template and DENIS 1048-39 was determined with a  $\chi^2$  test for every aperture used. The values

determined for the different apertures were then averaged to yield a final (averaged) rotational velocity of  $25.0 \pm 2 \text{ km s}^{-1}$  in good agreement with the  $v \sin(i)$ -value of  $27 \pm 5 \text{ km s}^{-1}$  found by Delfosse et al. (2001).

### 3.3. The Na I D lines

We fitted the stellar and airglow lines of Na I D simultaneously treating the central wavelength  $\lambda_{\text{cen}}$ , Gaussian  $\sigma$  and amplitude for every line as free parameters. The fit results are listed in Table 1. While the central wavelength of the airglow lines is stable as it should, our fits indicate a steady bluewards drift in the stellar Na I D lines. The line shifts were computed using 5889.950 and 5895.924 Å as reference central wavelengths; although the errors are large, the trend to bluer line centers is clearly visible.

The large amplitude for the line at 5895.924 Å in the first spectrum does not agree with the line amplitudes of the other three spectra that vary only slightly. We ascribe this to the heavy blending of the line and the faintness of the feature which makes its amplitude sensitive to noise and to the background level chosen for the fit.

### 3.4. The $H_\alpha$ and the $H_\beta$ line

The amplitudes of the  $H_\alpha$  and  $H_\beta$  lines were fitted with a single Gaussian line profile as for the Na I D lines. For the  $H_\beta$  line this seems to be a reasonably good description although the line center shows some fine structure. However, for the  $H_\alpha$  line these fits yielded only a very poor description of line profiles in UVES data. A major problem for our fits of the  $H_\alpha$  line is the background treatment, which is somewhat complicated with several unidentified broad emission and absorption features on

1082

B. Fuhrmeister and J. H. M. M. Schmitt: Flare on DENIS 104814.7-395606.1

**Table 2.** Properties of the  $H_\alpha$  and the  $H_\beta$  line. The line shift is given in  $\text{km s}^{-1}$  using  $4861.332$  and  $6562.817 \text{ \AA}$  as reference central wavelength.

		$H_\alpha$			Total	$H_\beta$
		Bump	1st comp	2nd comp		
1st spectrum	$\lambda_{\text{cen}} [\text{\AA}]$	$6561.29 \pm 0.04$	$6562.62 \pm 0.01$	$6563.07 \pm 0.01$		$4861.36 \pm 0.12$
	$\sigma [\text{\AA}]$	$0.54 \pm 0.04$	$0.34 \pm 0.01$	$0.22 \pm 0.01$		$0.31 \pm 0.02$
	Amplitude [electrons]	$7477.3 \pm 237.2$	$14094.2 \pm 259.0$	$7357.9 \pm 211.0$	$21452 \pm 334$	$4032 \pm 81$
	Line shift [ $\text{km s}^{-1}$ ]		$-9.0 \pm 0.5$	$11.6 \pm 0.5$		$1.7 \pm 7.4$
2nd spectrum	$\lambda_{\text{cen}} [\text{\AA}]$	$6561.19 \pm 0.05$	$6562.40 \pm 0.01$	$6562.96 \pm 0.01$		$4861.29 \pm 0.10$
	$\sigma [\text{\AA}]$	$0.40 \pm 0.01$	$0.42 \pm 0.01$	$0.25 \pm 0.01$		$0.26 \pm 0.02$
	Amplitude [electrons]	$8003.8 \pm 219.3$	$22086.6 \pm 301.1$	$10642.6 \pm 232.5$	$32728 \pm 380$	$3730 \pm 78$
	Line shift [ $\text{km s}^{-1}$ ]		$-19.0 \pm 0.5$	$6.5 \pm 0.5$		$-2.6 \pm 6.1$
3rd spectrum	$\lambda_{\text{cen}} [\text{\AA}]$	$6561.13 \pm 0.05$	$6562.36 \pm 0.01$	$6562.92 \pm 0.01$		$4861.15 \pm 0.10$
	$\sigma [\text{\AA}]$	$0.36 \pm 0.01$	$0.40 \pm 0.01$	$0.26 \pm 0.01$		$0.28 \pm 0.01$
	Amplitude [electrons]	$7669.0 \pm 213.6$	$33246.9 \pm 325.3$	$15394.6 \pm 261.5$	$48642 \pm 416$	$6460.9 \pm 97.2$
	Line shift [ $\text{km s}^{-1}$ ]		$-21.3 \pm 0.5$	$4.7 \pm 0.5$		$-11.2 \pm 6.1$
4th spectrum	$\lambda_{\text{cen}} [\text{\AA}]$	$6561.19 \pm 0.01$	$6562.39 \pm 0.01$	$6562.93 \pm 0.01$		$4861.14 \pm 0.02$
	$\sigma [\text{\AA}]$	$0.54 \pm 0.01$	$0.36 \pm 0.01$	$0.22 \pm 0.01$		$0.26 \pm 0.01$
	Amplitude [electrons]	$22450 \pm 288.5$	$43569.8 \pm 340.2$	$16920 \pm 253.5$	$60490 \pm 423$	$7841.0 \pm 107.1$
	Line shift [ $\text{km s}^{-1}$ ]		$-19.4 \pm 0.5$	$4.7 \pm 0.5$		$-11.8 \pm 1.2$

the blue side of the line and a slightly higher background level on the blue compared to the red side. Although there appears to be some variation in the background level we decided to use a constant background since there is no other reasonable method to treat the background problem i.e., there is no obvious gradient. We used the background value redwards of the line found in the second spectrum for our fits. Therefore the first broad emission feature at  $6561.29 \text{ \AA}$  (see Fig. 5) must be treated as an additional line feature in the fit of the  $H_\alpha$  line. The  $H_\alpha$  line also shows a strong asymmetry in the blue wing, where more and more flux appears during our spectral sequence, while the red wing of the line stays almost constant. We therefore decided to use two spectral components to describe the shape of the line core and a third component to account for the closest blue emission feature in the background. All fit components were assumed to be Gaussians and we use again central wavelength  $\lambda_{\text{cen}}$ , Gaussian  $\sigma$  and the line amplitude as free fit parameters. The results of our fits of the  $H_\alpha$  and the  $H_\beta$  line are listed in Table 2. In order to provide an example of the quality of our fits we show the fitted  $H_\alpha$  line for the first spectrum in Fig. 5. While not necessarily physical, the three components do obviously provide a good analytical description of the recorded UVES spectrum.

Since two Gaussian components are required for the fit of the core of the  $H_\alpha$  line, the question arises, why the  $H_\beta$  line behaves differently and can be fitted with a single component. Indeed, a close inspection of the line shape of the  $H_\beta$  line in the third spectrum also shows an additional red component. Therefore we tried to fit the  $H_\beta$  line with two components as well. For the third spectrum this leads to a substantial improvement of the fit resulting in similar line shifts and a similar ratio of the two components as for  $H_\alpha$  (see Fig. 6); unfortunately for the other spectra a fit with two components describing the line core does not lead to unique solutions and does not provide

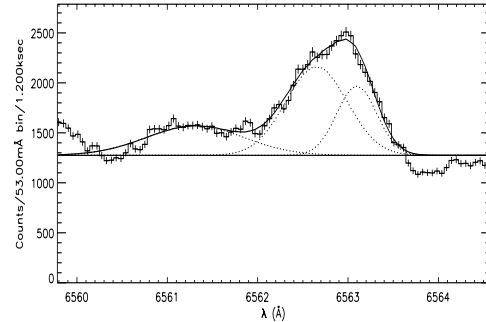


**Fig. 5.** Fit of the  $H_\alpha$  line in the first spectrum of the series. Two fit components are used for the line, while the third component accounts for the bump in the continuum blue to the line. The horizontal line is the background used for the fit. The dotted lines mark the single gaussian components used for the fit. Their free fit parameters can be found in Table 2.

significantly improved fit results. Therefore we decided to use the fits with one component for  $H_\beta$  bearing in mind that there is evidence for a second red component of the line that behaves similarly to the red component of the  $H_\alpha$  line at least for the third spectrum.

Our fit results for the  $H_\alpha$  line clearly demonstrate that the reddest line component is only weakly blue shifted during our observations, while the blue component is shifted by  $12.3 \text{ km s}^{-1}$  bluewards from its initial position during the first three spectra. In the last spectrum there are no additional line shifts observed neither for the  $H_\alpha$  line components nor for the  $H_\beta$  line, rather a substantial flux increase occurs in the blue component of the  $H_\alpha$  line and in the  $H_\beta$  line. For the  $H_\alpha$  line the ratio between the amplitude of the two components is approximately constant for the first three spectra, but in the last

B. Fuhrmeister and J. H. M. M. Schmitt: Flare on DENIS 104814.7-395606.1

1083

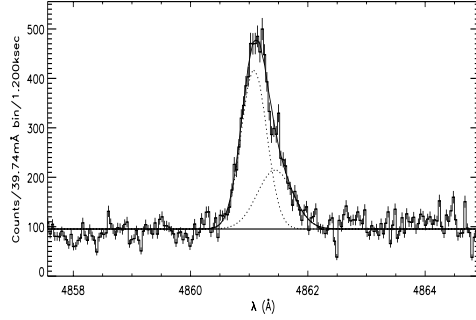


**Fig. 6.** Fit of the  $H_\beta$  line in the third spectrum of the series. Two fit components are used for the line resulting in a good fit of the line especially in the red wing. The horizontal line is the background used for the fit. The dotted lines mark the single Gaussian components.

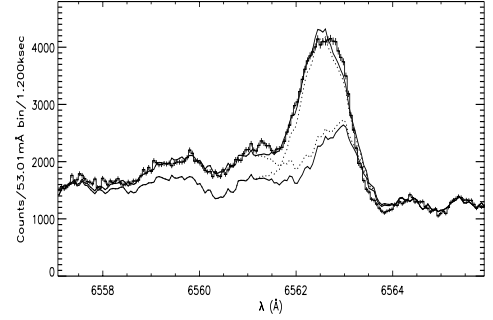


**Fig. 7.** Fit of the broad emission feature blueward of the  $H_\alpha$  line in the last spectrum of the series. The lower black line is the first spectrum of the series that was used as background. Note the flux increase between the two spectra not only in the line core but also in the broad emission feature centered at  $6560.5 \text{ \AA}$  blueward of the line. The two dotted lines are the single gaussian components used for the fit. Since the background is variable their shape does not appear to be Gaussian. Their free fit parameters can be found in Table 3.

**Table 3.** Properties of the broad emission feature bluewards of the  $H_\alpha$  and the  $H_\beta$  line in the last spectrum. The line shift is given in  $\text{km s}^{-1}$  using  $4861.332$  and  $6562.817 \text{ \AA}$  as reference central wavelength.

	$H_\alpha$	$H_\beta$
$\lambda_{\text{cen}} [\text{\AA}]$	$6560.51 \pm 0.01$	$4859.76 \pm 0.11$
$\sigma [\text{\AA}]$	$1.30 \pm 0.01$	$0.80 \pm 0.03$
Amplitude [electrons]	$27347.1 \pm 437.1$	$3645.3 \pm 104.7$
Line shift [ $\text{km s}^{-1}$ ]	$-109.9 \pm 0.5$	$-96.9 \pm 6.8$

spectrum the blue component is observed with some excess flux. We also note that the line shifts measured for the  $H_\beta$  line are consistent with the line shifts found in the Na I D lines.

In the last spectrum of our spectral series a tremendous flux increase occurs bluewards of the  $H_\alpha$  line. This increase can be seen in Fig. 1, but most clearly in Fig. 7. The “background” on the blue and red side of the  $H_\alpha$  line agrees for all spectra except for the blue side of the last spectrum in the spectral series. There a flux is detectable out to  $5 \text{ \AA}$  from line center, while blueward of  $6558 \text{ \AA}$  the two background levels are identical again.

In order to fit this additional flux in the last spectrum we used the first spectrum of the series as a background “template”. Obviously with this strategy we will not obtain meaningful results for the fit of the  $H_\alpha$  line itself, however, we merely intend to characterize the flux increase on the blue side of the  $H_\alpha$  line. For the fit we used two Gaussian components with the same free fit parameters as before. Since the fit of the  $H_\alpha$  line core is ill defined due to the background anyway we only used one Gaussian component for this core, while the other Gaussian is used to fit the broad emission component (see Fig. 7).

For the  $H_\beta$  in the last spectrum there is a similar broad emission feature of the blue side of the line as can be seen from Fig. 2. In this case the surrounding background is quite flat, therefore a fit of this broad emission line with a constant background would have been possible but for consistency reasons we fitted the broad emission feature with the first spectrum as background, too. The best fit parameters can be found in Table 3.

The line shifts of the broad emission features bluewards of the  $H_\alpha$  and the  $H_\beta$  line are not in agreement with each other due to the small error for the  $H_\alpha$  line ( $0.5 \text{ km s}^{-1}$ ). In contrast to this the error for the line shift of the broad component corresponding to the  $H_\beta$  line is quite big ( $6.8 \text{ km s}^{-1}$ ). Both errors should be considered only as formal ones since they are only statistical errors. The unusual background treatment can lead to additional systematic errors. If the errors for the  $H_\alpha$  line are as large as that of the  $H_\beta$  line, the line shifts actually agree very well.

Since absolute flux measurements were not the primary goal of this observing run, we obtained only a few measurements of standard stars. We calibrated our spectra with the standard star HD 49798, estimating the errors in the resulting fluxes to be as large as a factor of two. The measured line counts of the two main components of the  $H_\alpha$  line then translate into a flux of  $6.3 \times 10^{-14} \text{ erg cm}^{-2} \text{ s}^{-1}$ , resulting in a line luminosity of  $1.6 \times 10^{26} \text{ erg s}^{-1}$  using a distance of  $4.6 \text{ pc}$ . This is not particularly large compared to other  $H_\alpha$  line luminosities found for example for 2MASSW J0149090+295613 to be  $15.3 \times 10^{26} \text{ erg s}^{-1}$  during a flare (Liebert et al. 1999). Estimating the bolometric luminosity with  $M_J = 11.28 \text{ mag}$  (Neuhäuser et al. 2002) and  $BC = 1.95 \text{ mag}$  leads to  $L_{\text{bol}} = 1.5 \times 10^{30} \text{ erg s}^{-1}$  which yields a ratio of  $\log(L_{H_\alpha} / L_{\text{bol}}) = -4.0$ . According to Liebert et al. (2003) this would be quite high for an M9 dwarf in quiescent emission, but it is well in the range of observed  $L_{H_\alpha}$  to  $L_{\text{bol}}$  ratios for the few flaring events known for objects at the M to L spectral class transition.

### 3.5. Other Balmer lines

Due to the chosen instrumental setup we do not cover the  $H_3$  up to  $H_8$  of the Balmer series. Therefore we searched for emission lines at the position of  $H_3$  and higher Balmer series members. Unfortunately the blue part of the spectra is very noisy since the count rate is very low. We do find a faint emission

1084

B. Fuhrmeister and J. H. M. M. Schmitt: Flare on DENIS 104814.7-395606.1

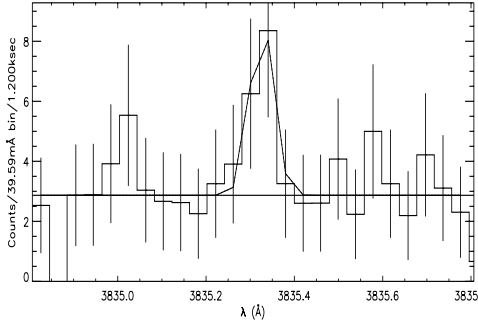


**Fig. 8.** The last spectrum in the series around 3835.386 Å. The fit shows the faint emission line of  $H_{\beta}$ . The horizontal line is the background used for the fit.

line at  $3835.31 \pm 0.04$  Å in our last spectrum, corresponding to a blue shift of  $-5.9 \pm 3.1$  km s $^{-1}$  which is less than that of the  $H_{\beta}$  line. Since  $H_{\alpha}$  and  $H_{\beta}$  differ significantly in appearance and blueshift, an interpretation of this faint line as  $H_{\beta}$  is very attractive. We found the best fit with an amplitude of  $9.1 \pm 4.0$  electrons,  $\sigma$  of  $0.02 \pm 0.01$  Å and central wavelength of  $3835.31 \pm 0.04$  Å. The line fit can be seen in Fig. 8. We also searched for higher Balmer lines. In the last spectrum an emission feature at  $3797.76 \pm 0.12$  Å corresponding to a blue shift of  $-11.0 \pm 9.5$  km s $^{-1}$  of  $H_{10}$  is found, but it is so weak that it can be due to noise. On the wavelength positions of  $H_{11}$  no emission is found.

## 4. Discussion and conclusions

### 4.1. Emission geometry

The measured half widths of the Na I D and the  $H_{\beta}$  lines always stay below 20 km s $^{-1}$ , i.e., they are smaller than the measured rotational velocity. The same applies to the two main components of the  $H_{\alpha}$  line. This suggests that the emission for the Balmer lines as well as for the Na I D lines is confined to a restricted region on the star. Since the  $H_{\alpha}$  line consists of two components and there is evidence that the  $H_{\beta}$  line consists of two components as well, the star could host even two active regions producing the observed Balmer emission. Now the question arises what the nature of these two active regions may be. There are two main possibilities: a dynamic scenario or a static scenario.

### 4.2. Static or dynamic scenario?

The dynamic scenario invokes two active regions located on the surface of the star and mass motions within these active regions. The Balmer emission comes from the chromosphere, nevertheless very close to the surface of the star. At least in one of the two regions a brightening in the Balmer lines takes place on a timescale of about 1.5 h.  $H_{\alpha}$  and  $H_{\beta}$  emitting material moves towards the observer and causes the blue shift.

The static scenario interprets the two regions as emitting gas clouds corotating in some distance to the stars surface as

was first proposed for the K0 star AB Dor by Collier Cameron & Robinson (1989). Since for one component the line shift becomes bluer this one must be rising while the other one must be about to set behind the star since its line shift is moving towards the blue. The blue shifted component must then be captured during its rise above the horizon of the star to account for the flux increase. This latter static scenario can be excluded because of the rapid rotation of the stars as follows: for an estimated radius of  $R_{\star} = 0.1 R_{\odot}$  the maximal rotation period of DENIS 1048-39 is 4.9 h. Therefore in the four consecutive spectra lasting together 80 min the star completes about a fourth of its rotation. If the emitting gas is confined in a corotating cloud, the measured velocity shift should exceed the star's rotational velocity in at least one spectrum for orbits near the equatorial plane. Moreover the flux increase cannot be explained by a cloud rotating into view because the star rotates too fast for this interpretation. A more natural explanation is therefore the scenario of active regions with mass motions at the surface of the star that brighten during the spectral series.

### 4.3. Blue-shifted Balmer emission

Let us now consider the broad emission features bluewards of the two Balmer lines seen only in the fourth spectrum. Again a dynamic or static scenario may be considered. Let us first assume a static interpretation with a corotating cloud. Since its radial velocity of about 100 km s $^{-1}$  is too high to be interpreted by a region on or near the surface of the star, the emission would have to come from a cloud at some distance to the star. Such a cloud must be confined then by magnetic loops above the surface of the star and has rotated just into the field of view. If one assumes a stellar inclination close to 90° and a cloud in the equatorial plane, one can compute its distance  $R$  from the rotation axis with  $R = \frac{vP}{2\pi}$  with  $v$  denoting the radial velocity and  $P$  the rotation period of DENIS 1048-39. We find a distance of  $R = 4 R_{\star}$  with the measured radial velocity of 100 km s $^{-1}$ , which is below the Keplerian corotation radius of  $6 R_{\star}$  like the clouds found on AB Dor in  $H_{\alpha}$  (Donati & Collier Cameron 1997) and other chromospheric lines (Brandt et al. 2001). But since the star rotates fast, the feature should be visible in more than one spectrum since for its distance of four stellar radii it can be shadowed by the star only about 10% of the time, i.e. about 30 min, thus again a dynamic interpretation appears more likely.

In the dynamical interpretation the line shift is explained in terms of material ejected by the star. Since the emission in the main body of the  $H_{\alpha}$  brightens substantially in the same spectrum it is suggestive that the broad emission feature is connected to the active region producing the  $H_{\alpha}$  line arguing further in favor of a dynamic scenario. In the context of interpreting the broad emission feature as the signature of a rising cloud the question remains unsettled whether this rise leads to mass ejection since we do not know the longitude of the cloud. Assuming again an radius of  $0.1 R_{\odot}$  we find an escape velocity of about 550 km s $^{-1}$  for a mass between 0.075 and 0.09  $M_{\odot}$  while the projected velocity of the cloud is about 100 km s $^{-1}$ .

Let us now consider the width of the emission feature. This width can be due to temperature and turbulent broadening if one thinks of a confined gas cloud rising towards the observer. A first estimate of the temperature of a  $H_{\alpha}$  emitting gas is about 10 000 K leading to a thermal broadening of  $9 \text{ km s}^{-1}$ , far less than the observed total line broadening of  $50 \text{ km s}^{-1}$ . In this scenario with a rising cloud one can estimate the height of the cloud after the twenty minutes exposure. Assuming a constant cloud velocity of the cloud and an ejection start right at the beginning of the exposure leads to a cloud height of  $1.7 R_{\star}$ . It is probable that the cloud has been decelerated during such a rise. Therefore a second interpretation of the line width is that different velocities of the cloud during deceleration are integrated over the exposure time. Moreover, the cloud may consist of more than one component with different velocities.

Besides these uncertainties in the event geometry there is no doubt that a dynamical interpretation of the spectra is needed. The last spectrum is then quite suggestively interpreted as the onset of a flare on DENIS 1048-39 as reported for AD Leo by Houdebine et al. (1990) who found a similar flux enhancement in the far blue wing of the  $H_{\gamma}$  line during a particular violent flare on AD Leo. Since these authors found projected velocities of up to  $5800 \text{ km s}^{-1}$  this event was clearly associated with a mass ejection, while this question remains unsettled for DENIS 1048-39.

#### 4.4. Summary

In conclusion, we find at least two active regions on DENIS 1048-39 contributing to the bulk of the Balmer line flux. Mass motions directed towards the observer are found

for the emission lines of the Balmer series as well as for the Na D lines. In the last spectrum of our observations the onset of a flare seems to take place, since substantial brightening and blueshifts can be seen in the lines. In addition in the  $H_{\alpha}$  and the  $H_{\beta}$  line there is a broad emission feature on the blue side of the line. This can be interpreted as a rising cloud.

Since DENIS 1048-39 seems to be located directly at the hydrogen burning limit this flare gives evidence that such events may be more ubiquitous than previously assumed. It is consistent with X-ray detections of brown dwarfs (Mokler & Stelzer 2002) and the X-ray flare event found on the similar late-type star LHS 2065 (Schmitt & Liefke 2002).

#### References

- Brandt, J. C., Heap, S. R., Walter, F. M., et al. 2001, *AJ*, 121, 2173  
 Collier Cameron, A., & Robinson, R. D. 1989, *MNRAS*, 236, 57  
 Delfosse, X., Forveille, T., Martín, E. L., et al. 2001, *A&A*, 366, L13  
 Donati, J.-F., & Collier Cameron, A. 1997, *MNRAS*, 291, 1  
 Epchtein, N. 1997, in *The Impact of Large Scale Near-IR Sky Surveys*, ed. F. Garzonet al (Kluwer: Dordrecht), *ASSL*, 210, 15  
 Gizis, J. E., Monet, D. G., Reid, I. N., et al. 2000, *AJ*, 120, 1085  
 Hanuschik, R. W. 2003, *A&A*, 407, 1157  
 Houdebine, E. R., Foing, B. H., & Rodono, M. 1990, *A&A*, 238, 249  
 Liebert, J., Kirkpatrick, J. D., Cruz, K. L., et al. 2003, *AJ*, 125, 343  
 Liebert, J., Kirkpatrick, J. D., Reid, I. N., & Fisher, M. D. 1999, *ApJ*, 519, 345  
 Mokler, F., & Stelzer, B. 2002, *A&A*, 391, 1025  
 Ness, J.-U., & Wichmann, R. 2002, *AN*, 323, 129  
 Neuhäuser, R., Guenther, E. W., Alves, J., et al. 2002, *AN*, 323, 447  
 Schmitt, J. H. M. M., & Liefke, C. 2002, *A&A*, 382, L9



## **Chapter 4**

# **Modeling M-dwarf chromospheres with PHOENIX**

**B. Fuhrmeister, J. H. H. M. Schmitt and P. H. Hauschildt**

Poster presented in Hamburg, July, 5th-9th, 2004 at conference

**Cool Stars 13**

published in

**Proc. 13th Cool Stars Workshop, Hamburg, 5–9 July 2004, F. Favata et al. eds.**

## MODELING M-DWARF CHROMOSPHERES WITH PHOENIX

B. Fuhrmeister<sup>1</sup>, J. H. M. M. Schmitt<sup>1</sup> and P. Hauschildt<sup>1</sup>

Hamburger Sternwarte - University of Hamburg, Gojenbergsweg 112, 21029 Hamburg, Germany

## ABSTRACT

We construct semi-empirical model chromospheres with the model atmosphere code PHOENIX. The models consist of a photosphere in thermal equilibrium and a parameterized temperature rise in the chromosphere and part of the transition region (TR). The photosphere chosen is our best fit to the photosphere of AD Leo, for which we have high-resolution UVES spectra in the wavelength range of 3000 to 6700 Å. We use these spectra for modeling the temperature rise as a function of column mass. Specifically, we investigate the influence of NLTE for the most important species, the influence of the temperature gradient and the influence of the temperature minimum. We present first model spectra and compare them to the averaged spectrum of AD Leo.

Key words: Stars: chromospheres – Stars: Model atmospheres

## 1. INTRODUCTION

Chromospheres of M dwarfs exhibit hundreds of emission lines in the spectral range between 3000 and 4000 Å depending on their individual activity level. Although the heating mechanisms of the chromospheres and coronae are not fully understood, we can learn more about the origin of the observed emission lines via the construction of semi-empirical chromosphere models. Semi-empirical modeling of the chromosphere was carried out quite successfully for the Sun (Vernazza et al. 1981). For M stars recent chromosphere modeling was carried out e. g. by Falchi & Mauas 1998, using the atmosphere code Pandora, or by Short & Doyle 1998, using the the atmosphere code MULTI and the atmosphere code PHOENIX for the background opacities. The lines under consideration were usually the Ly $\alpha$  line, the H $\alpha$  line, the Ca II H and K lines and a few other metal lines, but the plethora of emission lines in the near UV remained unused for the model construction so far. With the advent of the large telescopes like the VLT it is now possible to obtain high quality spectra of the faint M dwarfs in this spectral range and use them for chromosphere model construction.

## 2. OBSERVATIONS

The observations of AD Leo used as comparison data for the models were obtained in visitor mode with ESO's Kueyen telescope at Paranal equipped with the Ultraviolet-Visual Echelle Spectrograph (UVES) from March, 13th to 16th in 2002. The instrument was operated in a dichroic mode, yielding 33 echelle orders in the blue arm (spectral coverage from 3030 to 3880 Å) and 39 orders in the red arm (spectral coverage from 4580 to 6680 Å). Therefore we cannot observe the lines from H<sub>3</sub> up to H<sub>8</sub> of the Balmer series, nor do we cover the Ca II H and K lines. The typical resolution of our spectra is  $\sim 45000$ , typical exposures lasted 5 minutes. Unfortunately, the H $\alpha$  line is saturated in all of our spectra.

All data were reduced using IRAF in a standard way. The wavelength calibration was carried out using Thorium-Argon spectra with an accuracy of  $\sim 0.03\text{Å}$  in the blue arm and  $\sim 0.05\text{Å}$  in the red arm.

Since AD Leo underwent a major flare during the observations on 13th March 2002 we use one of the more inactive spectra taken on 16th March 2002 for the comparison to the models.

## 3. MODEL CONSTRUCTION

For the underlying photosphere we use a PHOENIX model (Hauschildt et al. 1999) with  $T_{\text{eff}}=3200\text{ K}$ ,  $\log g = 4.5$  and solar chemical composition, which is our best fit to the red part of the UVES spectrum of AD Leo. PHOENIX is able to reproduce cool photospheres of M dwarfs as well as hot atmospheres of e. g. Novae reasonably well (e. g. Hauschildt et al. 2003 and Hauschildt & Baron 1999) and is therefore the optimal atmosphere code for the large temperature range considered in chromospheric modeling.

The chromospheric models have compared to the photosphere models the following characteristics: They are computed in hydrostatic equilibrium on a given column mass ( $cm$ ) grid. The model includes the TR up to  $\log T=5.0$ . The temperature rise is parameterized as two linear parts as a function of  $\log cm$ . The top of the chromosphere is chosen at 8000 K (end of the first linear temperature rise). The temperature vs. column mass ( $cm$ ) gradient in the transition region is in all our models  $\log \frac{dT}{d \log cm} = 7.5$ . The temperature as a function of  $cm$  for our models can be seen in Fig. 1.

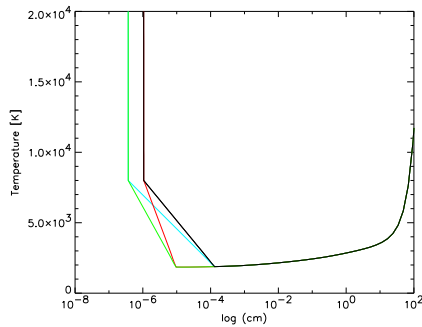


Figure 1. Temperature distribution of the different chromosphere models. The gradient in the TR is for all shown models the same. The best representation of the data is produced by the black model.

We also took into account the turbulent pressure characterized by the turbulent velocity  $\xi$  that rise for our model linear from  $2 \text{ km s}^{-1}$  in the photosphere to  $10 \text{ km s}^{-1}$  at the top of the chromosphere. Our most recent calculations suggest that a better agreement between observed spectra and models can be found treating the turbulent velocity as a fraction of the local sound velocity.

Since most of the emission lines seen in the spectrum of AD Leo are Fe I and Fe II lines we performed NLTE calculations for iron ions from Fe I to Fe X including all levels from the Kurucz line lists (Kurucz & Bell 1995). Moreover NLTE calculations were carried out for Ti I and Ti II, for Na I to Na IX and for all ions of H, He, C, N, O.

#### 4. RESULTS

Comparison between our best fit model and the observed spectrum is shown in Figs. 2 and 3. While the  $H_9$  line of the Balmer series is represented quite well, the higher Balmer lines tend to show too much flux in the models. Most of the iron lines are underpredicted. Also the Na I D lines and the He I emission lines cannot be modelled correctly at the same time by our models. This problem may be caused by the simple temperature distribution we use - an impression we get from our first experience with more complicated temperature structures that include plateaus or gradually steepening into the TR.

Since for AD Leo the Na D lines are seen as absorption lines with emission cores the minimum in the absorption line can serve as a diagnostic for the temperature minimum. This indicates that we should shift the  $T_{min}$  in our models to higher pressure (see section 5). The onset of the TR on the other hand has a major influence on the strength of the Balmer line series.

One severe problem is the high sensitivity of the line flux and the line profile on the NLTE calculations of other species. One example for the  $H_\alpha$  line can be seen in Fig. 4.

The line strength and profile is altered by the NLTE calculations of e. g. O or He. This behaviour is also found for the metal lines. For example most of the Fe I lines are severely damped by Helium NLTE calculations in comparison to He LTE calculations.

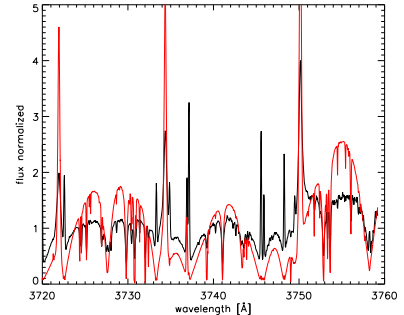


Figure 2. Comparison between the observed spectrum of AD Leo (black) and the best fit PHOENIX model (grey/red) in the spectral range around  $3740 \text{ \AA}$ . While the Balmer lines are too strong in the simulation some of the Fe lines are too faint.

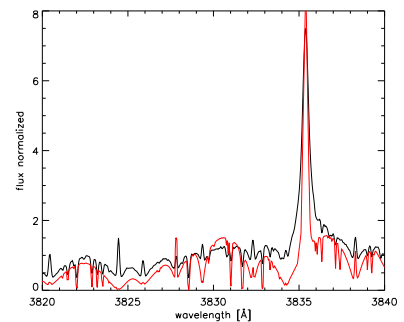


Figure 3. As Figure 2 but for the spectral range around  $3820 \text{ \AA}$ . The pronounced line is  $H_9$  which is reproduced well by the model in contrast to the Balmer lines in Figure 1.

This effect works by the influence of NLTE calculations on the electron density. NLTE calculations of one species change the electron density which in turn influences the level population of all other species and therefore the line strength and profile. The change in the electron density as a function of column mass as a result of NLTE computations can be seen in Fig. 5.

With PHOENIX it is possible to compute not only the spectrum emerging from the whole atmosphere, but to compute the spectrum of each layer of the model atmosphere. Therefore it is possible to trace the emergence of the flux to distinct layers. An example of such a multi

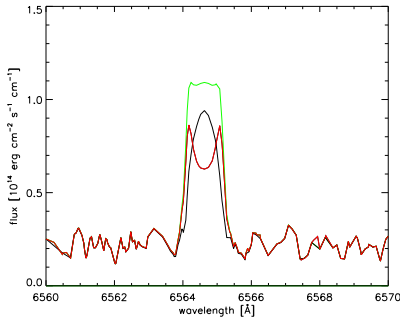


Figure 4. The influence of NLTE calculations on the  $H_\alpha$  line again for the best fit model. The line shape is significantly influenced by the number of species calculated in NLTE. Black: H, He, Fe and Ti in NLTE, light-grey/green: C and N additionally in NLTE, dark-grey/red: O and Na additionally in NLTE cause heavy self-absorption.

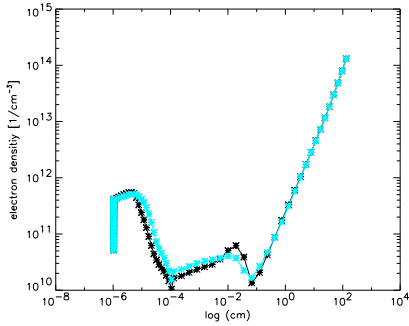


Figure 5. The influence of NLTE calculations on the electron density for the same model as in Fig. 3. Black: H, He, Fe and Ti in NLTE, grey/green: C, N, O and Na additionally in NLTE. The electron density especially in the chromospheric part of the atmosphere is crucial for the line intensities.

layer spectrum can be found in Fig. 6 for the  $H_\alpha$  line. It can be seen in which layers the emission line is formed and in which layers the  $H_\alpha$  line is formed as absorption line. There are even layers where the net flux in the line is directed inward and not outward.

## 5. OUTLOOK

Models with  $T_{min}$  at higher pressure than for the models shown here would be in better agreement with models found by using other computer codes. Moreover the diagnostic of the Na D lines points to  $T_{min}$  at higher pressure as well. Most recent calculations show that an agreement of PHOENIX models and the observed spectra is possible for higher pressure chromospheres - provided the turbulent velocity  $\xi$  is treated as a constant fraction of the locally determined sound velocity. For a linear  $\xi$  rise,  $\xi$  tends to get

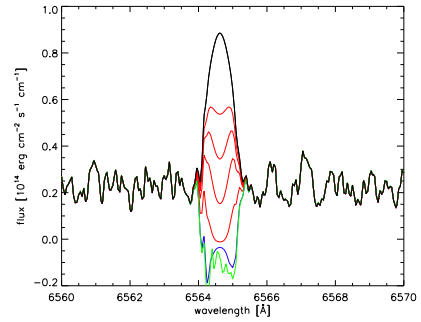


Figure 6. The origin of the  $H_\alpha$  line in the PHOENIX models. Shown is the depth dependent flux in the line. Negative flux is inward directed flux. The black line is the spectrum in the outermost layer (only H and Fe in NLTE). The emission lines with absorption cores represent the line in deeper layers with a corresponding  $T$  of 8000, 7200, 6700 and 6200 K in descending order. The dark-grey/blue spectrum with inward directed flux is formed at 5100 K. The light-grey/green one with inward directed flux is formed at the inner side of the temperature minimum at 2100 K. The line vanishes at 3100 K in the upper convection zone.

larger than the sound velocity for high pressure models. The new higher pressure chromosphere model set seems to work also for even more late-type stars and will be published in a forthcoming paper.

## ACKNOWLEDGEMENTS

Most of the model computations were performed at the Norddeutscher Verbund für Hoch- und Höchstleistungsrechnen (HLRN) B. Fuhrmeister acknowledges financial support by the Deutsche Forschungsgemeinschaft under DFG SCHM 1032/16-1.

## REFERENCES

- Allard, N. F., Allard, F., Hauschildt, P. H., Kielkopf, J. F., Machin, L., 2003, A&A, 411, L473
- Hauschildt, P. H., Allard, F., Baron, E., 1999, ApJ, 512, 377
- Hauschildt, P. H., Baron, E., 1999, JCAM, 109, 41
- Vernazza, J. E., Avrett, E. H., Loeser, R., 1981, ApJs, 45, 635
- Falchi, A., Mauas, P. J. D., 1998, A&A, 336, 281
- Kurucz, R. L., Bell, B., 1995, Kurucz CD-ROM, Cambridge
- Short, I., Doyle, J. G., 1998, A&A, 336, 613

## **Chapter 5**

# **Detection of red line asymmetries in LHS 2034**

**B. Fuhrmeister, J. H. H. M. Schmitt and P. H. Hauschildt**  
*Astronomy & Astrophysics*, 436, 677 (2005)



A&A 436, 677–686 (2005)  
 DOI: 10.1051/0004-6361:20042518  
 © ESO 2005

**Astronomy  
&  
Astrophysics**

## Detection of red line asymmetries in LHS 2034<sup>★</sup>

B. Fuhrmeister, J. H. M. M. Schmitt, and P. H. Hauschildt

Hamburger Sternwarte, University of Hamburg, Gojenbergsweg 112, 21029 Hamburg, Germany  
 e-mail: bfuhrmeister@hs.uni-hamburg.de

Received 10 December 2004 / Accepted 30 January 2005

**Abstract.** We report very pronounced line asymmetries during a long duration flare on the dM6 star LHS 2034 (AZ Cnc). While all lines of the Balmer series and all strong He I lines show these asymmetries, the metal lines do not. This can be explained with the help of PHOENIX model chromospheres considering the formation depth of the lines involved. Moreover, the asymmetries persist over about one hour changing shape and amplitude. Fitting the asymmetries with an additional broad Gaussian component leads us to the scenario of a series of downward propagating condensations that decelerate due to the higher density of the lower chromosphere. In addition, similar but weaker line asymmetries were found in LHS 2397a.

**Key words.** stars: activity – stars: flare – stars: late-type

### 1. Introduction

Stellar flares release large amounts of energy during a short time interval over a wide range of the electromagnetic spectrum. This energy is believed to result from free magnetic energy stored in the magnetic field configuration of the star and released by reconnection of magnetic field lines. Flaring is a commonly observed phenomenon in late-type stars, especially in M dwarfs, RS CVn systems, and young stars. Some dMe stars are known to increase their X-ray flux by a factor of 100 or more during flares (e.g. Favata et al. 2000). At X-ray wavelengths, energy releases in excess of  $10^{37}$  erg have been reported, e.g. for the T Tauri star Par 1724 (Preibisch et al. 1995), for Algol B (Schmitt & Favata 1999), and for the RS CVn system CF Tuc (Kürster & Schmitt 1996). While flares on more luminous stars are typically observed at UV and X-ray wavelengths, flares on dMe stars can also be observed easily at optical wavelengths (Pettersen 1991).

A flare represents a complex magnetohydrodynamic and radiative phenomenon involving large scale plasma motions. It is therefore not surprising that for some flare events on late-type stars line asymmetries have been detected. For example, Doyle et al. (1988) found broadened wings for the lines of the Balmer series during a flare of short duration on the dM4.5e star YZ CMi. While the  $H_\delta$  and  $H_\gamma$  lines showed symmetrically broadened profiles during the flare maximum, the higher lines  $H_\zeta$  and  $H_\eta$  showed flux enhancements in the red wing of the line profiles. Doyle et al. tried to fit these broad profiles with Voigt profiles and found that even two Voigt profiles would not provide acceptable fits to the shape of the line core and the wings. In contrast, two Gaussian components were found to fit

the profiles quite well. In the dM3.5e star AD Leo, Houdebine et al. (1993) also found red asymmetries in the core and in the wings of Balmer lines during a flare, which they interpreted as evidence of chromospheric downward condensations (CDC) similar to those seen on the Sun. CDCs originate in rapid evaporations of the pre-flare chromosphere which drive shocks upward and downward. The downward propagating shock then forms a condensation in its wake (Canfield et al. 1990). An example of asymmetries in the blue part of the wing was found in AT Mic by (Gunn et al. 1994) for the Balmer lines, as well as in the Ca II H and K line. These asymmetries were interpreted as upmoving material that has been heated by a particle beam from the apex of a magnetic loop.

More recently Montes et al. (1999) found line asymmetries during a long duration flare on the single, young, rapidly rotating K2 dwarf LQ Hya. Combining optical and IUE data, Montes et al. found broad wings in the Mg II lines and in the profiles of  $H_\alpha$ ,  $H_\beta$ , He I  $\lambda D_3$  line, and He I  $\lambda 6678$ , after subtraction of a quiescent template spectrum. They fitted the lines using two Gaussian components, resulting in a blueshift of the broad line component in the impulsive phase and a redshift of the broad component in the gradual phase with the shift increasing with time. They attribute these broad components to turbulence or to upward and downward mass motions. Similar broad components of emission lines have been found by Pagano et al. (2000) in AU Mic outside of flares in FUV transitions region lines, while the chromospheric lines do not show these asymmetric redshifted broad components. The origin of the broad component is identified as microflaring.

LHS 2034 (also known as AZ Cnc) is a dM6 flare star known as an X-ray emitter with  $\log L_X \approx 27.40$  during quiescence (Fleming et al. 1993). During the ROSAT all-sky observations it was caught in a long duration flare lasting for more

<sup>★</sup> Based on observations collected at the European Southern Observatory, Paranal, Chile, 68.D-0166A.

**Table 1.** Exposure time, date, and UT of the beginning of each exposure of LHS 2034.

Spectrum	Date	UT	Exposure time [s]
1st	March, 14th	01:18:40.0	1200
2nd	March, 14th	01:39:45.0	1200
3rd	March, 14th	02:00:42.0	1200
4th	March, 14th	02:22:33.0	600
5th	March, 14th	02:34:05.0	600
6th	March, 14th	02:45:36.0	600
1th	March, 16th	00:54:32.0	1200
2th	March, 16th	01:15:30.0	1200

than three hours, possibly similar to the flare that is our subject here.

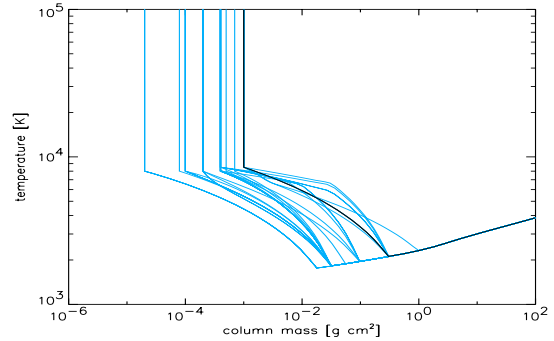
We report very strong wing asymmetries during a long duration flare on LHS 2034 and similar asymmetries in the spectrum of LHS 2397a, which are not, however, connected with a strong flare. In Sect. 2 we describe our observations, data analysis and the chromospheric models. In Sect. 3 we report on the radial and rotational velocity. In Sect. 4 we report on the emission line behavior during the long duration flare on LHS 2034. We focus on asymmetries seen comparing flaring and quiescent state. In Sect. 5 we present the results of chromosphere modelling for the decay phase of the flare on LHS 2034. A general discussion that includes a search for similar asymmetries in other stars and the weak asymmetries found in LHS 2397a and our conclusions, can be found in Sect. 6.

## 2. Observations and data analysis

The M6 dwarf LHS 2034 was observed with ESO's Kueyen telescope on Paranal equipped with the Ultraviolet-Visual Echelle Spectrograph (UVES) on March 14th and 16th, 2002 (program ID 68.D-0166A). LHS 2034 was observed for 1.5 h on March 14th and for 40 min on March 16th. A large flare occurred during the observations on March 14th. Details on the observation are listed in Table 1; the instrument setup and data reduction are described in detail by Fuhrmeister et al. (2004b). The spectra were taken in dichroic mode; as a consequence, our setup covers neither the Balmer lines from H<sub>3</sub> up to H<sub>8</sub> nor the Ca II H and K lines. The typical resolution of our spectra is  $\sim 45\,000$ .

The data were reduced using IRAF in a standard way. The wavelength calibration was carried out with ThAr spectra giving an accuracy of  $\sim 0.03\text{ \AA}$  in the blue arm and  $\sim 0.05\text{ \AA}$  in the red arm. The data was not corrected for night sky emission lines or telluric lines. In addition to the UVES spectra there are photometric data from the UVES exposuremeter, actually taken for engineering purposes and therefore not flux calibrated. Nevertheless this data can be used in a qualitative way for assessing flares.

Spectral line fitting was done with the CORA program (Ness & Wichmann 2002), kindly provided to us by Dr. J.-U. Ness and originally developed for analyzing high resolution X-ray spectra. The fit algorithms employed by CORA are also well suited to modelling all types of emission lines with

**Fig. 1.** Temperature vs. column mass distribution for the flare models on a logarithmic scale. The black line denotes the best fit model out of the grid.

count statistics. CORA uses a maximum likelihood method for fitting line profiles. The program also provides accurate error analysis.

In addition to line fitting with CORA we modelled the flaring atmosphere of LHS 2034 with the PHOENIX atmosphere code (Hauschildt et al. 1999). These models consist of (i) an underlying photosphere; (ii) a linear temperature rise vs. log column mass in the chromosphere; and (iii) transition region (TR) with different gradients. For the underlying photosphere, a model with  $T_{\text{eff}} = 2800\text{ K}$ ,  $\log g = 5.0$ , and solar chemical composition was used. The best fit of the photosphere was determined with an  $\chi^2$  technique using a model grid with  $T_{\text{eff}} = 2300\text{--}3700\text{ K}$  and  $\log g = 4.0\text{--}5.5$  in steps of  $\Delta T_{\text{eff}} = 100\text{ K}$ , and  $\Delta \log g = 0.5$ . We build the flare model spectra as a linear combination of the quiescent chromospheric spectra and the flaring chromospheric spectra, similar to the approach of Mauas & Falchi (1996). For the quiescent chromosphere, we use the last spectrum taken in the flare series, since the star is again in a more active state during our second time series. For the flaring models, we computed a grid of 42 models with the onset of the transition region at rather high pressure. The temperature vs. column mass distributions for our flare models are plotted in Fig. 1. Normally we treat only H, He, and Na I–IV in NLTE, but for the best fitting models we used a larger NLTE set. These models treat H, He, C I–III, N I–III, O I–III, Fe I–IV, Ti I–Ti II, Na I–IV, and Mg I–III in NLTE. All NLTE calculations take all those levels into account from either the Kurucz database (Kurucz & Bell 1995) or from the CHIANTI database (Young et al. 2003) for He. A detailed discussion of the model construction is given by Fuhrmeister et al. (2004a).

## 3. Radial and rotational velocity

We measured the radial velocity of LHS 2034 as  $64.2 \pm 0.6\text{ km s}^{-1}$  by determining the peak position of the cross-correlation function between the spectrum of LHS 2034 and radial velocity template spectrum of CN Leo. For CN Leo (also known as Gl 406) we determined a radial velocity of  $18.3 \pm 0.8\text{ km s}^{-1}$  by comparison to an absolute wavelength scale in good agreement with  $19.0 \pm 1.0\text{ km s}^{-1}$  found by Mohanty & Basri (2003). Our radial velocity for LHS 2034 agrees well

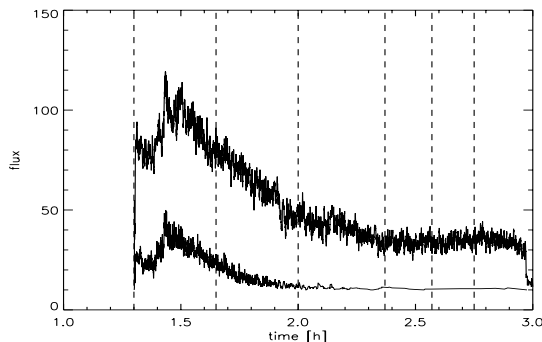


**Fig. 2.** Light curve of LHS 2034 during the observation on March 14th, 2002. The upper light curve corresponds to the red part of the spectrum, while the lower light curve corresponds to the blue part. The flare can be seen clearly in both spectral ranges. The vertical dashed lines indicate the beginning of each exposure. The flare ends at about the beginning of the third exposure.

with the  $69.8 \pm 10.0 \text{ km s}^{-1}$  determined by Reid et al. (1995). No wavelength shifts in the emission lines occur in any of our spectra of LHS 2034.

Since the radial velocity of LHS 2034 is unusually high, we also analyzed its galactic motion. According to its space velocities  $U = -60.6 \text{ km s}^{-1}$ ,  $V = -44.3 \text{ km s}^{-1}$ , and  $W = -8.3 \text{ km s}^{-1}$  (relative to the local standard of rest), it belongs kinematically to the old disk applying the criteria listed by Leggett (1992). Given the activity of LHS 2034, one expects a much younger star; however, there is no young cluster or star forming region that LHS 2034 can be attributed to in any obvious way.

We measured the rotational velocity of LHS 2034 as  $v \sin(i)$  of  $7.9 \pm 2.8 \text{ km s}^{-1}$  again using CN Leo as template (Fuhrmeister et al. 2004b). Since an estimate of the rotational velocity out of the  $FWHM$  of some of the emission lines leads to the same value, the emission seems to originate in a substantial area of the stellar surface, and not in just a few isolated regions.

#### 4. Line asymmetries on LHS 2034

##### 4.1. The long duration flare on LHS 2034

The optical light curve of the observation on 14th March 2002 shows a major long duration flare as seen in Fig. 2. We have no coverage of the onset of the flare, but we do cover the decay phase; and in the last three spectra the star is probably back to its “quiescent emission”. During the flare hundreds of emission lines appear, most of them decaying completely in the course of the first three spectra. Very few absorption lines are seen in the spectra.

The He I lines found in the flare spectrum is listed in Table 2. For further analysis we only use the He I D<sub>3</sub> line at 5875 Å, and the He I singlets at 4921 and 5015 Å, since they are the lines with the most obvious asymmetry. The He I D<sub>3</sub> transition is a multiplet consisting of six component lines at wavelengths 5875.60, 5875.614, 5875.615, 5875.63, 5875.64, and 5875.97 Å, respectively. The first five components are too

**Table 2.** List of identified He I lines in the first spectrum of LHS 2034. Column one gives the rest wavelength after Moore (1972), Col. 2 gives an indication of the level of asymmetry, and finally column three gives further comments.

Wavelength [Å]	Asymmetry	Comment
3187.743	very weak	weak line
3554.394	blended	very weak line
3613.641	blended	very weak line
3819.606	very weak	very weak line
4921.931	detected	
5015.675	detected	
5875.650	detected	two line components

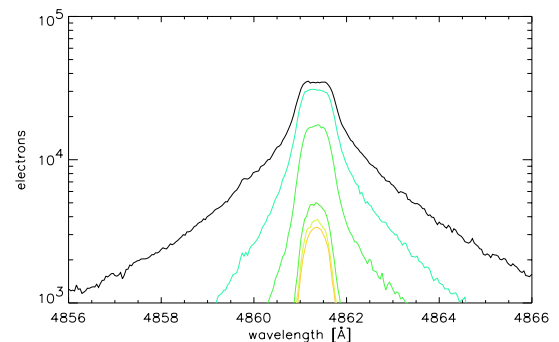


**Fig. 3.** Spectral sequence of the  $H_{\beta}$  line on a logarithmic plot. Note the large asymmetries in the second and third spectra: in the red wing there is considerably more flux than in the blue.

close together to be resolved in the spectra, but the last component can be resolved and is actually seen in the spectra.

In the first flare spectrum, the Balmer series is clearly seen up to  $H_{18}$ , while in the fifth and sixth spectrum  $H_{11}$  is the highest detected Balmer line. For the  $H_{\alpha}$  line in the first (flare) spectrum we determine an equivalent width ( $EW$ ) of 109 Å, and for the  $H_{\beta}$  line we find an  $EW$  of 149 Å. The  $H_{\beta}$  line is shown in Fig. 3, while an example of the  $H_{\alpha}$  line can be found in Fig. 6.

##### 4.2. Line symmetries and asymmetries on LHS 2034

An example of line asymmetries for the  $H_{\beta}$  line is shown in Fig. 3. The  $H_{\beta}$  line displays very broad wings in the first three spectra of the time series during the flare and no significant wings in the last three spectra taken during the constant part of the lightcurve. These unbroadened lines are highly symmetrical at first glance, while the broadened lines show additional flux in the red wings leading to much shallower slopes on the red side than on the blue side. The line fitting procedure also revealed small asymmetries in the last three spectra.

The shapes of the He lines and of the lines of the Balmer series have to be contrasted with the line shapes of metal lines that remain unbroadened. This difference is exemplified in Fig. 4, where we compare the He I D<sub>3</sub> line and the Na D lines. Obviously, the Na D lines are highly symmetrical, while the He lines are not.

680

B. Fuhrmeister et al.: Line asymmetries in LHS 2034

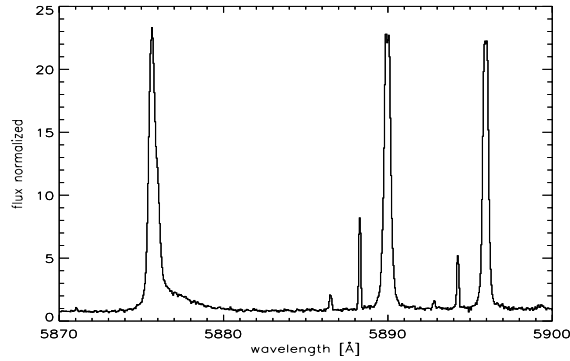


**Fig. 4.** Spectral wavelength around the He I D<sub>3</sub> line at 5875 Å and the Na D lines at 5890 and 5896 Å in the second spectrum of the series. Though the strength of the line is about the same, the He I D<sub>3</sub> line shows red wing asymmetry while the Na D lines does not. All other (narrow) emission lines seen in this part of the spectrum are known airglow lines.

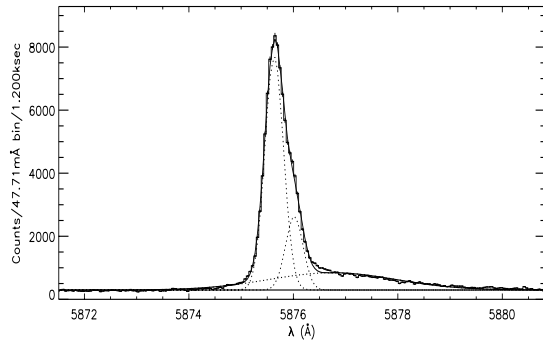


**Fig. 5.** Example of the three-component fit of the He I D<sub>3</sub> line in the second spectrum. Plotted are all three components, the resulting fit, and the data.

In order to quantitatively describe the measured line profiles we modelled the lines with up to three Gaussian components, for each we fitted the amplitude, the Gaussian  $\sigma$ , and the central wavelength as free parameters of each component. An example of the general fit quality is given in Fig. 5 for the He I D<sub>3</sub> line. Despite the low signal the quality of the fits of the high Balmer lines and blue He I lines are of comparable quality. Fits with one and two Gaussians clearly show the need for a two Gaussian fit. For example for the first spectrum and the H $\beta$  line a one-component fit resulted in  $\chi^2$  of 568, while a two-component fit resulted in  $\chi^2$  of 29 (the line is fitted rather poorly since it suffers from some self-absorption). For the H<sub>11</sub> line with a much lower  $S/N$ , a one-component fit resulted in  $\chi^2$  of 2.76, while two components lead to  $\chi^2 = 0.66$ . We did encounter difficulties in fitting the H $\alpha$  line, since it shows strong self-absorption in the line center. The peak of the Gaussian plays a large role in the fitting process so that the fit is severely hampered by self-absorption. We thus decided to exclude the data in the line center from the fitting process and fitted the amplitude of the narrow component manually. This procedure resulted in satisfactory fits as illustrated in Fig. 6. Since for the narrow component neither the wings nor the peak but only the side lobes are used for the fit, the Gaussian cannot be well

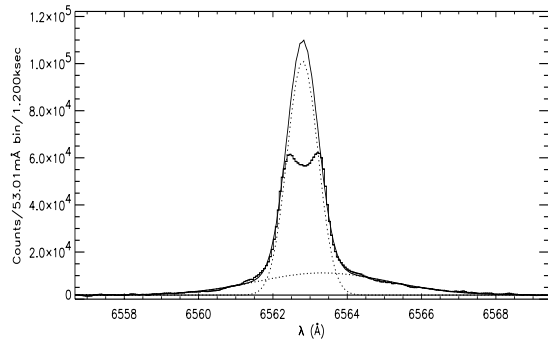


**Fig. 6.** Fit of the H $\alpha$  line with two components. The amplitude of the narrow component was fitted manually due to the severe self-absorption. The fit parameters can be found in Table 3 for Spectrum 2.

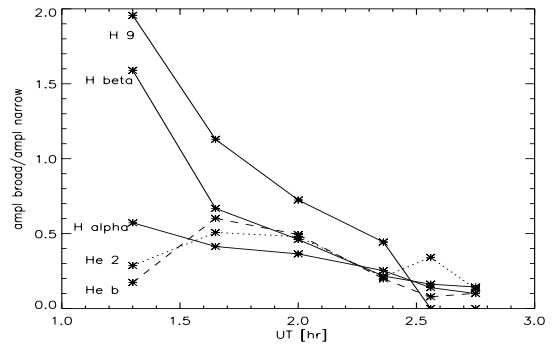


**Fig. 7.** Ratio of the amplitude of the broad line component to the narrow line component. The ratio between the main component of the He I D<sub>3</sub> line and its broad component is named “He b”, and between the main component and the second component it is named “He 2”.

constrained, and the errors of the  $FWHM$ , and especially the amplitude, are large. Fortunately, the fit parameters of the narrow component do not influence the fit parameters of the broad component too severely.

Using the procedure described above we fitted the H $\alpha$ , H $\beta$ , H $\gamma$ , H $\delta$ , H $\epsilon$ , and H $\zeta$  lines in the Balmer series and the He lines at 5875, 5015, 4921, 3819, and 3187 Å. Except for the first two spectra the He lines at 5015, 4921, 3819, and 3187 Å required only a single line due to the low signal. This similarly applies to the high Balmer lines, where H $\gamma$  and H $\delta$  lines show a broad component only in the first four spectra, while the H $\zeta$  line shows a broad component only in the first three spectra. In the sixth spectrum for H $\gamma$  the two-component fit leads to  $\chi^2$  of 0.30, while one component has a  $\chi^2 = 0.31$ . Therefore, two components do not lead to a substantial improvement of the fit. The fit parameters for the stronger lines are listed in Table 6 for He I D<sub>3</sub>, in Table 3 for the H $\alpha$  line, in Table 4 for the H $\beta$  line, and in Table 5 for the H $\gamma$  line.

Fit amplitudes of both the narrow and the broad component decay with time, but the amplitude of the broad component decays much faster than that of the narrow component (cf., in Fig. 7). For the He I D<sub>3</sub> line the ratio increases from the first to the second spectrum and then decreases as for the Balmer lines. The same applies to the ratio between the main component of the He I D<sub>3</sub> line and its weaker component at 5875.97 Å.

**Table 3.** Free fitting parameters for the  $H_\alpha$  line. The wavelength difference  $\Delta\lambda$  between the narrow component and the broad component is also given. The amplitude of the narrow component is fitted manually and so no error estimate is given for this value. Since the peak of the narrow line was not included in the fitting process, no error computation of the central wavelength was carried out. We estimate the error to be similar to the values found for the other Balmer lines. Especially the value for the narrow component seems to be quite accurate compared to the rest wavelength of 6562.817 Å of the line (Moore 1972).

sp	$A_n$ [ $10^3$ electrons]	$A_b$ [ $10^3$ electrons]	$\sigma_n$ [Å]	$\sigma_b$ [Å]	$\lambda_n$ [Å]	$\lambda_b$ [Å]	$\Delta\lambda$ [Å]
1	2150	1232 ± 2	0.40 ± 0.04	1.91 ± 0.05	6562.80	6562.81	0.01
2	1950	807 ± 1	0.41 ± 0.03	1.78 ± 0.01	6562.78	6563.30	0.52
3	1150	419 ± 1	0.40 ± 0.04	1.68 ± 0.08	6562.79	6563.65	0.86
4	350	88 ± 0.5	0.39 ± 0.04	1.59 ± 0.15	6562.79	6563.55	0.76
5	330	46 ± 0.4	0.36 ± 0.03	1.16 ± 0.16	6562.79	6563.28	0.49
6	310	31 ± 0.4	0.35 ± 0.04	1.80	6562.79	6562.85	0.06
7	510	130 ± 0.7	0.38 ± 0.04	1.62 ± 0.16	6562.82	6562.30	-0.52
8	810	319 ± 0.9	0.38 ± 0.04	1.76 ± 0.02	6562.82	6562.62	-0.20

**Table 4.** Fitting parameter for the  $H_\beta$  line. The given errors are formal ones and should be considered with caution. Sometimes no error estimates were possible. All given parameters besides  $\Delta\lambda$  were free parameters in the fit. The rest wavelength of the  $H_\beta$  line is 4861.33 Å, showing that there are no wavelength shifts in the narrow component.

sp	$A_n$ [ $10^3$ electrons]	$A_b$ [ $10^3$ electrons]	$\sigma_n$ [Å]	$\sigma_b$ [Å]	$\lambda_n$ [Å]	$\lambda_b$ [Å]	$\Delta\lambda$ [Å]
1	608 ± 1	967 ± 1	0.37 ± 0.02	1.55	4861.32 ± 0.01	4861.39 ± 0.01	0.07 ± 0.01
2	617 ± 1	412 ± 1	0.35	1.38	4861.32	4861.70	0.38
3	311 ± 1	143 ± 0.5	0.30	1.26	4861.33 ± 0.01	4861.92 ± 0.01	0.59 ± 0.01
4	80 ± 0.3	17 ± 0.2	0.26	0.94 ± 0.03	4861.33 ± 0.01	4861.78 ± 0.01	0.45 ± 0.01
5	59 ± 0.2	9 ± 0.2	0.24 ± 0.01	0.92 ± 0.02	4861.32 ± 0.08	4861.75 ± 0.04	0.43 ± 0.09
6	52 ± 0.2	7 ± 0.2	0.24	1.02 ± 0.07	4861.33 ± 0.04	4861.64 ± 0.08	0.31 ± 0.09
7	74 ± 0.3	29 ± 0.3	0.27 ± 0.01	0.85	4861.34 ± 0.04	4861.23 ± 0.01	-0.11 ± 0.04
8	143 ± 0.5	94 ± 0.5	0.29	0.98	4861.34 ± 0.01	4861.32 ± 0.04	-0.02 ± 0.04

**Table 5.** Free fitting parameters for the  $H_\gamma$  line. The wavelength difference  $\Delta\lambda$  between the narrow component and the broad component is also given. In the first spectrum here are three and in the second spectrum two additional metal lines in the direct vicinity of  $H_\gamma$  that had to be fitted simultaneously to give the correct line profile. Especially for the fitting of many lines, the errors should be treated with caution and should be considered only as formal errors.

sp	$A_n$ [electrons]	$A_b$ [electrons]	$\sigma_n$ [Å]	$\sigma_b$ [Å]	$\lambda_n$ [Å]	$\lambda_b$ [Å]	$\Delta\lambda$ [Å]
1	3316 ± 84	6489 ± 127	0.21 ± 0.01	1.15	3835.37 ± 0.06	3835.34 ± 0.09	-0.03 ± 0.11
2	2520 ± 66	2846 ± 83	0.20 ± 0.01	1.00	3835.38 ± 0.06	3835.43 ± 0.11	0.05 ± 0.13
3	671 ± 41	486 ± 48	0.16 ± 0.01	0.48 ± 0.05	3835.37 ± 0.07	3835.49 ± 0.23	0.12 ± 0.24
4	124 ± 19	55 ± 23	0.14 ± 0.01	0.40	3835.38 ± 0.08	3835.45 ± 0.27	0.07 ± 0.28
5	101 ± 13		0.17 ± 0.02		3835.37 ± 0.16		
6	75 ± 11		0.14 ± 0.01		3835.43 ± 0.13		
7	248 ± 20		0.21 ± 0.02		3835.40 ± 0.14		
8	458 ± 32	534 ± 42	0.19 ± 0.02	0.81 ± 0.08	3835.39 ± 0.09	3835.34 ± 0.29	-0.05 ± 0.30

For the narrow components of all lines, Gaussian width  $\sigma$  is almost constant or decreases only slowly. The broad component has a decreasing width  $\sigma$  as well, but in the sixth spectrum it increases again slightly; we caution, however, that this may be an artifact from our fits, because the amplitude is very small for all lines and the true error in the fit parameters may be larger than indicated by the formal errors because of the fit's non-uniqueness.

The line shifts between the narrow and broad components vary differently from line to line as can be seen in Fig. 8 for

different He and Balmer lines. While the Balmer lines have very similar line shifts in the first spectrum, their behavior deviates in the following spectra; the higher Balmer lines ( $H_9$ ,  $H_{10}$ , and  $H_{11}$ ) have a much smaller line shift in the broad component than the  $H_\alpha$  and  $H_\beta$  lines. In general, line shifts increase during the first three spectra and then start to decrease. For the He I lines, increase in the line shifts is observed only in the first two spectra. The He I D<sub>3</sub> line shows the largest line shift between its narrow and broad component for all the lines in the second spectrum.

**Table 6.** Fitting parameters for the He I D<sub>3</sub> line. In addition the wavelength difference  $\Delta\lambda$  between the narrow component and the broad component is given. The two components of the multiplet have rest wavelength of 5875.62 and 5875.99 Å showing the good quality of the multi-component fit.

sp	$A_n$ [e <sup>-</sup> ]	$A_s$ [e <sup>-</sup> ]	$A_b$ [e <sup>-</sup> ]	$\sigma_n$ [Å]	$\sigma_s$ [Å]	$\sigma_b$ [Å]	$\lambda_n$ [Å]	$\lambda_s$ [Å]	$\lambda_b$ [Å]	$\Delta\lambda$ [Å]
1	94 178 ± 361	16 357 ± 325	26 978 ± 254	0.18	0.15	0.86 ± 0.01	5875.60	5875.97	5876.03	0.43
2	59 912 ± 304	30 378 ± 266	36 065 ± 305	0.17	0.20	1.26	5875.58	5875.93	5876.72	1.14
3	24 563 ± 197	11 793 ± 175	12 126 ± 201	0.16 ± 0.01	0.20 ± 0.01	1.10 ± 0.03	5875.59 ± 0.01	5875.93	5876.62 ± 0.04	1.03
4	6698 ± 94	1411 ± 60	1326 ± 95	0.16 ± 0.01	0.13 ± 0.01	0.82 ± 0.08	5875.62	5876.00 ± 0.02	5876.52 ± 0.14	0.90
5	3886 ± 76	1327 ± 61	304 ± 46	0.15	0.14 ± 0.01	0.22 ± 0.02	5875.59 ± 0.01	5875.93 ± 0.02	5876.28 ± 0.08	0.69
6	3590 ± 71	470 ± 46	365 ± 52	0.17 ± 0.01	0.10 ± 0.01	0.26 ± 0.03	5875.61 ± 0.01	5875.98 ± 0.03	5876.24 ± 0.07	0.63
7	7666 ± 112	2653 ± 89		0.18	0.19		5875.62 ± 0.01	5875.97 ± 0.01		
8	15 437 ± 152	5765 ± 121		0.16	0.20		5875.62 ± 0.01	5875.98 ± 0.01		

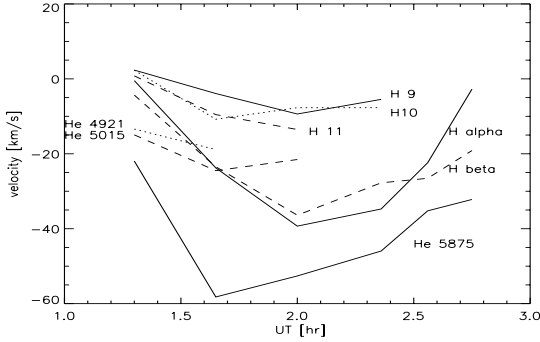


**Fig. 8.** Line shift between the narrow and the broad component of the different lines. Error should be typically about 10 km s<sup>-1</sup>.

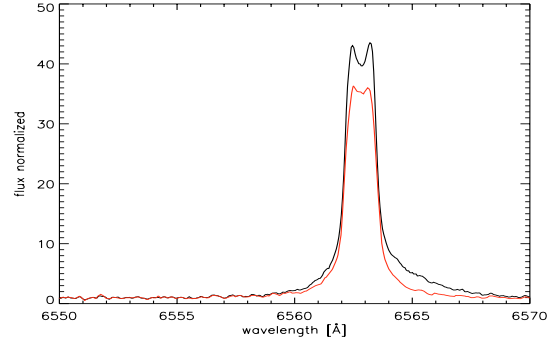


**Fig. 9.** Comparison of model (grey/red) and the first flare spectrum of LHS 2034 (black) around H<sub>α</sub>.

### 4.3. LHS 2034 in quiescence

In addition to the spectra taken during the flare on March 14th, we obtained two additional spectra taken on March 16th. The photometer showed no obvious activity at that time; nevertheless, the emission lines vary in strength. The strength of the lines is rising from the seventh to the eighth spectrum again. The lines of the Balmer series again show a broad component with the amplitude a substantial fraction of the narrow component, or even exceeding it in the case of H<sub>9</sub>. The fitted central wavelength of the broad component is blueshifted for the H<sub>α</sub> and H<sub>β</sub> lines for the seventh spectrum, whereas the fit of the H<sub>9</sub> line is reasonably good without a broad component for this spectrum, as can be seen from Tables 3–5. In the last spectrum the H<sub>9</sub> line again displays a broad line component but the line shift is consistent with zero, and the same applies to H<sub>β</sub>. Nevertheless the H<sub>α</sub> line seems to show a blueshift. Although the error of the central wavelengths could not be treated properly, it should be much smaller than the inferred wavelength shift. Table 6 shows that there is no broad component detected for the He I D<sub>3</sub> line in either of the two spectra.

## 5. Chromosphere simulations of LHS 2034

We compared our PHOENIX model chromosphere grid to the second spectrum taken during the flare where the largest asymmetries occur. This spectrum was taken in the decay phase of the flare, while the first spectrum contains part of the rise phase

of the flare. We used this second spectrum, since we computed all models in hydrostatic equilibrium, which is generally a poor approximation during the impulsive phase of a flare, but should not be too bad during the decay phase.

We use an  $\chi^2$  algorithm to find the best fit model. Since our simulations suggested from the beginning that the flare would need a rather high filling factor, we take filling factors of 0.4, 0.3, 0.2, 0.17, 0.15, 0.13, 0.1, 0.07, 0.05, 0.03, and 0.01 into account. Indeed there are some indications that larger flares involve larger areas of the star rather than higher energy particle beams (Houdebine 2003).

The quality of the fit is checked for each filling factor using the following wavelength ranges: 6561.0 to 6562.8, 4860.5 to 4862.2, 5870 to 5900, 3715 to 3755, 3818 to 3830, and 3840 to 3870 Å. The fit with the best mean  $\chi^2$  for all wavelength ranges is indicated in Fig. 1 in black and has a filling factor of 20 percent. If the last spectrum in the flare series is not the one used as quiescent spectrum but instead the eighth spectrum taken on March 16th, then the best fit model has a transition region (TR) gradient 0.5 dex higher and a filling factor of 17 percent. Therefore the influence of the variations in the quiescent chromosphere is small. In Fig. 1 the two best fit models appear identical, because the difference in the TR gradient cannot be seen.

The quality of the fit can be seen for the H<sub>α</sub> line and around the Na D lines in Figs. 9 and 10 for the best overall model. The Na D line emission is vastly underpredicted for all our models,

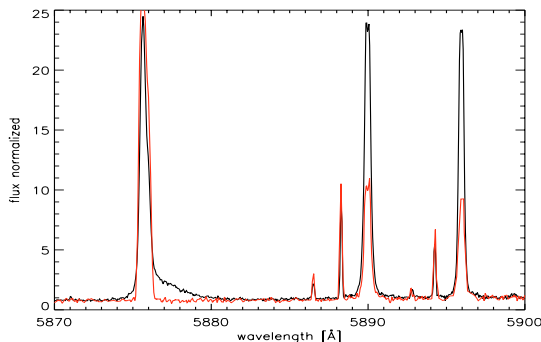


**Fig. 10.** Comparison of model (grey/red) and the first flare spectrum of LHS 2034 (black) around the Na D lines and the He I D<sub>3</sub> line. While the He line is slightly overpredicted, the Na D lines are vastly underpredicted. The narrow airglow lines are found in the model since we used a quiescent observed spectrum to mix with.

although our grid contains models with different temperature distributions in the lower chromosphere to which the Na D line emission is sensitive. Many of the Fe lines in the blue part of the spectrum are underpredicted as well, while the high Balmer lines in the same wavelength regime and the H $\beta$  line are overpredicted.

We investigated the approximate line formation depth of individual lines using spectra of each layer of the model atmosphere. Formation of the resulting spectrum in the outermost layer can be observed from layer to layer. One problem with this ansatz is that the net flux is tracked, i.e. the flux going inward is accounted for as well. We inferred from these layer spectra that the He and H lines are formed in the upper chromosphere, while the Na D lines and the wings of Fe I and Fe II and Mg I lines are formed in the middle and lower chromosphere. Therefore the phenomenon that only the H and He lines are showing line asymmetries is explained by the different formation depth of the lines. Accordingly the observed downflows must originate in a restricted area in the upper chromosphere or at least in material with similar temperatures.

Because the measured *FWHM* of the broad redshifted components of the emission lines may be interpreted as turbulent velocity, we compared the inferred turbulent velocities of about 80 to 90 km s<sup>-1</sup> with the sound velocity in the upper chromosphere as given by the models, which is about 10 km s<sup>-1</sup>. This indicates that the *FWHM* is not caused by microturbulence but that the broad feature may actually consist of more than one condensation moving at super sonic velocity with respect to their surroundings.

Moreover we investigated the behaviour of multiplet components of the He I D<sub>3</sub> line. The relative height both of the weaker component and the main component can be explained either by changes in the gradient of the TR or by changes in the temperature at the onset of the TR. Higher gradients and lower pressure at the onset of the TR result in a lower relative amplitude of the multiplet component at 5875.97 Å compared to the other components; therefore the He I D<sub>3</sub> line would imply that the gradient of the TR should be increased by about 1 dex for the highest pressure models. Temperature at the top

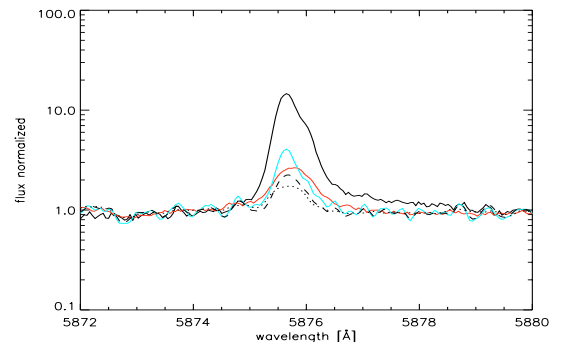


**Fig. 11.** Comparison of the He I D<sub>3</sub> line for a number of program stars. The black line denotes LHS 2034 where the asymmetry can be seen clearly. Also plotted are the flare spectrum of LHS 2076 (grey/red), the strongest CN Leo spectrum (light grey/turquoise), and the averaged spectrum of GL Vir (dotted) and of YZ Cmi (dashed). No strong wing asymmetries are found in the other spectra, except the bump that originates from the reddest line component.

of the chromosphere has less influence on the ratio of the components. Since other lines are fitted less well by these He I D<sub>3</sub> defined models we could not find models that fit many lines equally well.

## 6. Discussion and conclusions

### 6.1. Asymmetries in other program stars?

The asymmetries seen in LHS 2034 are unique in their strength for the 21 late-type M and L dwarfs of our program originally designed to search for the forbidden Fe XIII line at 3388 Å. The spectral characteristics for the mid-type M dwarfs are discussed in Fuhrmeister et al. (2004b) and for the whole sample in Fuhrmeister et al. (2004a). During the observations short duration flares also occurred on LHS 2076 and CN Leo. For CN Leo there is, in addition, a one-hour observation showing enhanced line flux, while the photometer does not show obvious flare activity. Some examples for the He I D<sub>3</sub> line can be found in Fig. 11 comparing it to LHS 2034. A similar line asymmetry could be found in none of the program stars, except LHS 2397a where very weak red asymmetries were found. For CN Leo we checked if a broad component might be present without being recognized due to low *S/N* ratio. We took the CN Leo spectrum and measured the amplitude of the (narrow) He I D<sub>3</sub> line at about 260 000 electrons. For LHS 2034 the amplitude of the broad component is about half that of the narrow component. Therefore we took about 100 000 electrons and added them to the CN Leo spectrum in a broad component with  $\sigma = 0.9$  Å and central wavelength at 5876.1 Å adding Poisson noise. The resulting feature was easily recognizable. Since all mid-type M dwarfs in the sample have *S/N* ratios similar to CN Leo, we conclude that no other star is exhibiting strong asymmetries as observed in LHS 2034.

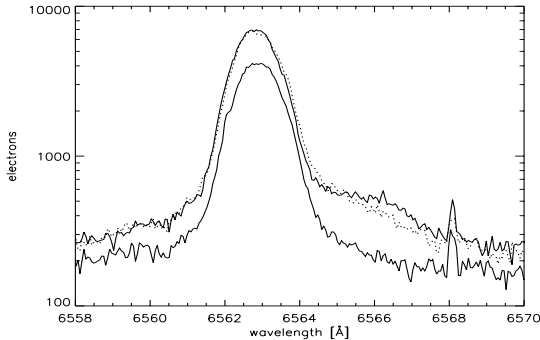


**Fig. 12.** The  $H_\alpha$  line for LHS 2397a. While the first two spectra show enhanced  $H_\alpha$  flux and some red wing asymmetries, the third spectrum fits well with only one component.

### 6.2. LHS 2397a

As mentioned above weak asymmetries were also found for LHS 2397a. LHS 2397a (GJ 3655) is a dM8 flare star that was recently discovered to have a brown dwarf companion of spectral type L7.5 (Freed et al. 2003). LHS 2397a shows a large spread in its recorded  $H_\alpha$  equivalent widths ranging from 15.3 to 47.3 Å (Tinney & Reid 1998; Gizis et al. 2000). We have three spectra of LHS 2397a resulting in one-hour total exposure. In two of the three spectra of the combined light from LHS 2397a and the L dwarf LHS 2397b, line asymmetries are seen; since no lines appear to be double we assume in the following that the signal is dominated by LHS 2397a. The photometer shows that the star was quiescent during the observations. Nevertheless, LHS 2397a shows very strong  $H_\alpha$  and  $H_\beta$  emission with an  $EW$  of about 57 Å for the  $H_\alpha$  line and 38 Å for the  $H_\beta$  line in the first two spectra. In the last spectrum the  $H_\alpha$  emission line has decreased to an  $EW$  of 33 Å. While the  $H_\alpha$   $EW$  for the first two spectra is considerably higher than the range of 15.3 to 47.3 Å found by Tinney & Reid (1998) and Gizis et al. (2000), the  $EW$  found in the last spectrum seems to be quite normal for LHS 2397a. Both the  $H_\alpha$  and  $H_\beta$  line are observed to have a broad component that is redshifted with respect to the narrow component. The line asymmetries disappear in the last spectrum. The asymmetries are shown in Fig. 12. LHS 2397a also shows a rather weak He I D<sub>3</sub> line and the Balmer series up to H<sub>11</sub> thus providing more evidence for its high activity even during apparent quiescence. Because of the fairly poor signal to noise ratios in these lines we cannot demonstrate the existence of a broad component.

The free fit parameters for the  $H_\alpha$  and  $H_\beta$  lines are given in Table 7. The ratio of amplitude between the broad and the narrow components is for LHS 2397a in the same range as for LHS 2034 at the end of the flare in the fourth, fifth, and sixth spectra. The width of the narrow line component is consistent with rotational broadening, so like LHS 2034 the line seems to originate in not just one single active region. The width of the broad component is about the same value as the largest width found for LHS 2034.

Little can be said about the relative velocities between the narrow and broad components since the measurements of the

$H_\beta$  line have large errors, and the broad line is very shallow. For the  $H_\alpha$  line the velocity is decelerated from 49 to 26 km s<sup>-1</sup>. Measurements for the  $H_\beta$  line are consistent with these measurements for  $H_\alpha$ , as well as with the hypothesis that the velocity between narrow and broad component of  $H_\beta$  does not change at all for the two spectra.

An origin of the additional emission from the secondary L dwarf can be ruled out. Since the estimated orbital period is about 25 years (Freed et al. 2003) and the separation is 2.96 AU, the expected maximum velocity shift for lines from the secondary is about 3.5 km s<sup>-1</sup> in contrast to the about 30 km s<sup>-1</sup> observed for LHS 2397a. Since the  $EW$  of the  $H_\alpha$  and  $H_\beta$  line is rather high in the first two spectra, the asymmetries may nevertheless be connected with activity. Simultaneously taken X-ray data would help to better understand the activity connection of the asymmetries, once more pointing out the need for multi-wavelength observations of flare connected phenomena. As it stands now the case of LHS 2397a is rather confusing since the photometer diagnostic contrasts with the line diagnostic of the equivalent width. Mass motions are not a likely explanation of the broad component since they are only expected in flares. Another explanation in the case of LHS 2397a is additional emission from an active region since the inferred maximum velocity is about 30 km s<sup>-1</sup>. Again considering the errors of about 10 km s<sup>-1</sup> this is in agreement with the rotational velocity of LHS 2397a. Mohanty & Basri found LHS 2397a to be a fast rotator with a  $v \sin(i)$  of 20 km s<sup>-1</sup>. As long as we lack a good template star we cannot measure its rotational velocity; however, the  $FWHM$  of the emission lines of LHS 2397a is consistent with rotational velocity of 20 to 30 km s<sup>-1</sup>. Therefore, flickering in an active region near the limb of LHS 2397a may cause the broad component without leading to a flare signature in the photometer data.

### 6.3. LHS 2034

Since we also do not see line asymmetries in any of the models, the observed asymmetries should not be an intrinsic part of the line profile. We therefore attribute the additional red wing flux in the Balmer and He lines to Doppler shifted emission from downward moving material. An alternative to emitting down-moving material would be an up-moving absorption layer. Then the Balmer and He lines would have to be symmetrically Stark broadened and the blue wing would be absorbed, leaving the red wing asymmetry. There are two arguments against that. First, we did not see symmetrically broadened lines in any of our chromospheric models. And second, the asymmetries are fitted quite well with two Gaussian emission lines. If they were instead composed of one emission and one absorption line, we would expect a poor fit with two emission lines especially in the blue wing.

Since we do see similar asymmetries in LHS 2397a without a flare, the asymmetries in LHS 2034 and the flare may be pure coincidence and not physically connected. The broad emission feature may then originate in a cloud co-rotating with the star as was proposed for transient absorption features in the K0 star AB Dor by Collier Cameron & Robinson (1989). In this case

**Table 7.** Free fitting parameters for LHS 2397a for the  $H_\alpha$  (*top*) and the  $H_\beta$  (*bottom*) line. In addition the wavelength difference  $\Delta\lambda$  between the narrow component and the broad component is given.

sp	$A_n$ [ $10^3$ electrons]	$A_b$ [ $10^3$ electrons]	$\sigma_n$ [ $\text{\AA}$ ]	$\sigma_b$ [ $\text{\AA}$ ]	$\lambda_n$ [ $\text{\AA}$ ]	$\lambda_b$ [ $\text{\AA}$ ]	$\Delta\lambda$ [ $\text{\AA}$ ]
1	$173 \pm 0.5$	$34 \pm 0.4$	$0.56 \pm 0.01$	$2.04 \pm 0.01$	$6562.80 \pm 0.01$	$6563.87 \pm 0.01$	$0.07 \pm 0.01$
2	$169 \pm 0.5$	$38 \pm 0.4$	$0.57 \pm 0.01$	1.88	$6562.85 \pm 0.01$	$6563.42 \pm 0.21$	$0.57 \pm 0.21$
3	$115 \pm 0.4$	$\pm 0.61$	0.06		$6562.88 \pm 0.33$		
1	$33 \pm 0.2$	$7 \pm 0.2$	$0.35 \pm 0.01$	$1.32 \pm 0.07$	$4861.34 \pm 0.05$	$4861.93 \pm 0.37$	$0.59 \pm 0.37$
2	$35 \pm 0.2$	$12 \pm 0.2$	0.37	$1.43 \pm 0.04$	$4861.39 \pm 0.10$	$4861.90 \pm 0.05$	$0.51 \pm 0.11$
3	$20 \pm 0.2$		$0.39 \pm 0.02$		$4861.43 \pm 0.15$		

the Doppler shift is not caused by a downward motion but by the rotation of the co-rotating cloud that is about to set behind the star. By assuming of an inclination close to  $90^\circ$  and the cloud close to the equatorial plane, one can compute the distance of the cloud from the star's surface as  $d = \frac{vP}{2\pi}$  with  $P$  the rotation period of the star and  $v$  the radial velocity of the cloud. With an estimated radius of the star of  $R_* = 0.1 R_\odot$  and measured  $v \sin i = 8 \text{ km s}^{-1}$  one obtains  $P = 15 \text{ h}$ , and with a radial velocity of the Balmer line feature of about  $30 \text{ km s}^{-1}$  one obtains a distance of  $d = 3.9 R_*$ . Variation in the cloud's radial velocity would then be due to the geometry with peak velocity reached when the cloud is besides the star and diminishing while the cloud rotates behind the star. Since the distance to the star is fairly high, the cloud need not to rotate behind the star during about 1 h of diminishing radial velocities. But if the cloud is not obscured by the star in this scenario, the monotonic decreasing line strength is hard to explain. Another problem is the large *FWHM* that leads to supersonic turbulent velocities if the cloud is at chromospheric temperatures and in hydrostatic equilibrium.

A solution to both problems may be a co-rotating cloud that has become unstable during the onset of the flare and is now expanding and cooling. But since the *FWHM* of the broad emission features seen in LHS 2397a are equivalent and no obvious flare activity was noticed there, we regard this scenario as unlikely. And since the strength of the broad emission lines is decaying even faster than the Balmer and He lines, a stronger connection between the excess emission seen in LHS 2034 and the flare is suggested.

One explanation for the asymmetries may be a magnetically confined cloud that has lost its supporting magnetic field during the flare and is falling down onto the star, with the deceleration caused by penetration of denser layers in the atmosphere of the star. The decay in amplitude would then be interpreted as cooling of the cloud; however, with an averaged velocity of about  $30 \text{ km s}^{-1}$  the cloud would be able to fall about  $2.3 R_*$  (assuming the radius of the star to be  $0.1 R_\odot$ ). This seems to be a rather odd place for the origin of a magnetically confined cloud. Moreover, such a scenario could not explain the restriction of the asymmetries to the He and H lines since a falling cloud should have a broad temperature distribution.

Another explanation of the asymmetries are mass flows similar to chromospheric downward condensations (CDC) as known for the Sun (Canfield et al. 1990). While the downflows found during a flare in AD Leo (Houdebine et al. 1993) had velocities of up to  $800 \text{ km s}^{-1}$  our downflows have peak

velocities of up to  $60 \text{ km s}^{-1}$ , which is in the velocity range of CDCs on the Sun (e.g. Fisher 1989). Fisher (1989) also shows that the peak downflow velocity is related to the total flare energy flux at the peak of the flare  $F_{\text{evap}}$  as follows:

$$v_{\text{peak}} \sim 0.4 \left( \frac{F_{\text{evap}}}{\rho} \right)^{1/3}$$

with  $\rho$  the chromospheric density. We estimate  $F_{\text{evap}}$  by totalling the flux in our first spectrum, converting to the surface flux using  $R = 0.1 R_\odot$  and  $d = 13.9 \text{ pc}$ , and dividing by the filling factor. We then obtain  $F_{\text{evap}} = 2.1 \times 10^{10} \text{ erg cm}^{-2} \text{ s}^{-1}$  and  $\rho = 3.8 \times 10^{-10} \text{ g cm}^{-3}$  from our flare model for the upper chromosphere leading to peak velocities of about  $15 \text{ km s}^{-1}$ . Our observed velocities tend to be smaller than this value except for the He I  $D_3$  line. Measured velocities for the first spectrum tend to be lower but are in agreement with this value, considering the rather large errors (see Fig. 8).

For the Sun such events can last a few minutes, whereas the asymmetries on LHS 2034 last for 1.5 h. Since the chromospheric modelling gives strong evidence that mass motions occur in the upper part of the chromosphere, a series of downward moving condensations is needed. The *FWHM* of the broad components compared to the sound velocity also indicates that there is more than one condensation present at the same time. Thus the favourite scenario of the asymmetries is a series of flare-triggered downward moving condensations in the upper chromosphere. Since our spectra have rather long integration times compared to the lifetime of condensations on the Sun, condensations occurring at the same time at different places in the flare region cannot be distinguished from condensations occurring at the same place during the integration time.

#### 6.4. Summary

In our VLT spectra of two late-type M dwarfs we find evidence for downward directed mass motions manifesting themselves in red wing asymmetries of hydrogen and helium lines. Surprisingly, both stars belong kinematically to the old disk despite their rather high level of activity during our observations. Chromospheric modeling with the atmosphere code PHOENIX suggests that the lines showing downward motions are formed in the high chromosphere. For LHS 2034, these chromospheric flare models lead to fairly high filling factors of about 20 percent for the flaring chromosphere. Furthermore, the width of the broad emission feature building up the line asymmetry is unlikely to be due to turbulent velocity. This would

require supersonic velocities in the upper chromosphere, so we prefer interpreting it as a series of downflows.

*Acknowledgements.* The model computations were performed at the Norddeutscher Verbund für Hoch- und Höchstleistungsrechnen (HLRN) and at the Hamburger Sternwarte Apple G5 cluster financially supported by HBF. We thank Dr. R. Wichmann for the computation of the space velocities. B.F. acknowledges financial support by the Deutsche Forschungsgemeinschaft under DFG SCHM 1032/16-1. P.H.H. was supported in part by the Pôle Scientifique de Modélisation Numérique at ENS-Lyon.

## References

- Canfield, R. C., Penn, M. J., Wulser, J., & Kiplinger, A. L. 1990, *ApJ*, 363, 318
- Collier Cameron, A., & Robinson, R. D. 1989, *MNRAS*, 236, 57
- Doyle, J. G., Butler, C. J., Bryne, P. B., & van den Oord, G. H. J. 1988, *A&A*, 193, 229
- Favata, F., Reale, F., Micela, G., et al. 2000, *A&A*, 353, 987
- Fisher, G. H. 1989, *ApJ*, 346, 1019
- Fleming, T. A., Giampapa, M. S., Schmitt, J. H. M. M., & Bookbinder, J. A. 1993, *ApJ*, 410, 387
- Freed, M., Close, L. M., & Siegler, N. 2003, *ApJ*, 584, 453
- Fuhrmeister, B., Schmitt, J. H. M. M., & Hauschildt, P. H. 2004a, *A&A*, submitted
- Fuhrmeister, B., Schmitt, J. H. M. M., & Wichmann, R. 2004b, *A&A*, 417, 701
- Gizis, J. E., Monet, D. G., Reid, I. N., et al. 2000, *AJ*, 120, 1085
- Gunn, A. G., Doyle, J. G., Mathioudakis, M., Houdebine, E. R., & Avgoloupis, S. 1994, *A&A*, 285, 489
- Hauschildt, P. H., Allard, F., & Baron, E. 1999, *ApJ*, 512, 377
- Houdebine, E. R. 2003, *A&A*, 397, 1019
- Houdebine, E. R., Foing, B. H., Doyle, J. G., & Rodono, M. 1993, *A&A*, 274, 245
- Kürster, M., & Schmitt, J. H. M. M. 1996, *A&A*, 311, 211
- Kurucz, R. L., & Bell, B. 1995, *Atomic line list Kurucz CD-ROM*, Cambridge, MA: Smithsonian Astrophysical Observatory, April 15, 1995
- Leggett, S. K. 1992, *ApJS*, 82, 351
- Mauas, P. J. D., & Falchi, A. 1996, *A&A*, 310, 245
- Mohanty, S., & Basri, G. 2003, *ApJ*, 583, 451
- Montes, D., Saar, S. H., Collier Cameron, A., & Unruh, Y. C. 1999, *MNRAS*, 305, 45
- Moore, C. E. 1972, *Nat. Stand. Ref. Data Ser.*, 40
- Ness, J.-U., & Wichmann, R. 2002, *Astron. Nachr.*, 323, 129
- Pagano, I., Linsky, J. L., Carkner, L., et al. 2000, *ApJ*, 532, 497
- Pettersen, B. R. 1991, *Mem. della Soc. Astron. Ital.*, 62, 217
- Preibisch, T., Neuhaeuser, R., & Alcalá, J. M. 1995, *A&A*, 304, L13
- Reid, I. N., Hawley, S. L., & Gizis, J. E. 1995, *AJ*, 110, 1838
- Schmitt, J. H. M. M., & Favata, F. 1999, *Nature*, 401, 44
- Tinney, C. G., & Reid, I. N. 1998, *MNRAS*, 301, 1031
- Young, P. R., Del Zanna, G., Landi, E., et al. 2003, *ApJS*, 144, 135

## **Chapter 6**

# **PHOENIX model chromospheres of mid-to late-type M dwarfs**

**B. Fuhrmeister, J. H. H. M. Schmitt and P. H. Hauschildt**  
accepted by A&A



## PHOENIX model chromospheres of mid- to late-type M dwarfs $\star$ , $\star\star$

B. Fuhrmeister, J. H. M. M. Schmitt and P. H. Hauschildt

Hamburger Sternwarte, University of Hamburg, Gojenbergsweg 112, D-21029 Hamburg  
e-mail: bfuhrmeister@hs.uni-hamburg.de

the date of receipt and acceptance should be inserted later

**Abstract.** We present semi-empirical model chromospheres computed with the atmosphere code PHOENIX. The models are designed to fit the observed spectra of five mid- to late-type M dwarfs. Next to hydrogen lines from the Balmer series we used various metal lines, e. g. from Fe I, for the comparison between data and models. Our computations show that an NLTE treatment of C, N, O impacts on the hydrogen line formation, while NLTE treatment of less abundant metals such as nickel influences the lines of the considered species itself. For our coolest models we investigated also the influence of dust on the chromospheres and found that dust increases the emission line flux.

Moreover we present an (electronically published) emission line list for the spectral range of 3100 to 3900 and 4700 to 6800 Å for a set of 21 M dwarfs and brown dwarfs. The line list includes the detection of the Na I D lines in emission for a L3 dwarf.

**Key words.** stars: activity – stars: late-type – stars: chromospheres

### 1. Introduction

Chromospheric activity as indicated, for example, by  $H_\alpha$  emission is frequently found in early-type M dwarfs, and ubiquitously in mid to late-type M dwarfs. There are indications that the  $H_\alpha$  emission during quiescence declines for very late-type M dwarfs and L dwarfs (Liebert et al. 2003; Gizis et al. 2000), although even brown dwarfs can show  $H_\alpha$  emission at least during flares. Since the heating mechanisms of chromospheres and coronae are poorly understood, we may hope to learn more about the observed emission lines via the construction of semi-empirical chromospheres.

Semi-empirical modelling of the chromosphere of the Sun was carried out quite successfully by Vernazza et al. (1981), determining the temperature distribution versus the column mass ( $m$ ). Early models for M dwarfs were constructed by Cram & Mullan (1979). More recently, Hawley & Fisher (1992) constructed chromosphere and transition region (TR) models of different activity level including soft X-ray emission from the corona. An ansatz using a linear temperature rise vs.  $\log m$  in the chromosphere and TR was used by Short & Doyle (1997) and related papers (e. g. Short & Doyle (1998), Andretta et al. (1997)). These investigators used the atmospheric code MULTI (Carlsson 1986), and in addition the atmospheric code PHOENIX (Hauschildt et al. 1999) to calculate background

opacities. Falchi & Mauas (1998) instead used the atmosphere code Pandora (Avrett & Loeser 1984) and a non-linear temperature versus  $\log m$  distribution. The lines under consideration were usually the  $Ly_\alpha$  line, the  $H_\alpha$  line, the Ca II H and K lines and a few other metal lines. One problem with such models lies in the uniqueness of the description. In other words: Can there be two different models producing the same line fluxes? Naturally this problem must be more severe if only few lines are used for adjusting the model.

With the advent of large telescopes like the VLT it is now possible to obtain high quality spectra in the (optical) near UV, where M dwarfs exhibit hundreds of chromospheric emission lines. Since most of these lines are Fe I and II lines, at least Fe has to be computed in NLTE in addition to H and He – an approach that has become possible in the last few years due to increasing computing power.

In this paper we present model chromospheres for mid-type M dwarfs during quiescent state adjusted via various lines in the wavelength range between 3600 and 6600 Å. Our paper is structured as follows: In sect. 2 we describe the VLT data used for our analysis and the sample of M dwarfs. In sect. 3 we deal with the model construction and describe the influence of various model parameters in sect. 4. We present our best fit models for the individual stars in sect. 5 and discuss several aspects of the models in sect. 6. In the appendix a catalog of chromospheric emission lines is presented.

Send offprint requests to: B. Fuhrmeister

\* Based on observations collected at the European Southern Observatory, Paranal, Chile, 68.D-0166A.

\*\* Table A.2 is only available in electronic form at the CDS via anonymous ftp.

## 2. Observations and data analysis

A set of 23 M dwarf spectra was taken with UVES/VLT in visitor and in service mode between winter 2000 and March 2002. The original sample was designed for a search for the forbidden Fe XIII line at 3388 Å and covers the whole M dwarf regime from M 3.5 plus a few L dwarfs known to show  $H_{\alpha}$  activity. All stars were selected for their high activity level. Two of the stars were double stars and since the spectra could not be disentangled, they were excluded from analysis, and we ended up with 21 objects.

The five objects used in the modelling were selected to cover the M dwarf temperature regime with good S/N ratios and without obvious flaring activity during the observations. The spectra were obtained in visitor mode with ESO's Kueyen telescope at Paranal equipped with the Ultraviolet-Visual Echelle Spectrograph (UVES) from March, 13th to 16th in 2002. The instrument was operated in dichroic mode, yielding 33 echelle orders in the blue arm (spectral coverage from 3030 to 3880 Å) and 39 orders in the red arm (spectral coverage from 4580 to 6680 Å). Therefore we cannot observe the lines from  $H_3$  up to  $H_8$  of the Balmer series, nor do we cover the Ca II H and K lines. The typical resolution of our spectra is  $\sim 45000$ , typical exposures lasted 5 to 20 minutes. Unfortunately the  $H_{\alpha}$  line is saturated in all of our spectra for AD Leo, CN Leo and YZ CMi. On the other hand, the blue part of the spectrum is underexposed for LHS 3003 and partly for DX Cnc, and therefore was not used for the modelling.

All data were reduced using IRAF in a standard way. The wavelength calibration was carried out using Thorium-Argon spectra with an accuracy of  $\sim 0.03\text{\AA}$  in the blue arm and  $\sim 0.05\text{\AA}$  in the red arm (i. e., more than 90 percent of the residuals of the wavelength calibration are lower than this value; the same is found for the difference between measured and laboratory wavelength in the emission line measurements presented in the appendix). In addition to the UVES spectra there are photometric data from the UVES exposure meter. These data were actually taken for engineering purposes, and are therefore not flux calibrated. Still, these data were useful to assess whether the star was observed during quiescence or during a major flare. We used the photometer data to decide which spectrum was taken during quiescence and therefore can be used for the chromospheric modelling. If no flare occurred during the whole observation and the spectra seem to be quite stable we used the averaged spectrum to obtain a better S/N (see Tab. 1).

We show two typical parts of the spectrum of CN Leo in Figs. 1 and 2 to point out the wealth of emission lines in the blue part of the spectrum. There are hundreds of emission lines originating in the chromosphere, all of which could in principle be used for the modelling. Since the lines belong to many different species we had to decide which species to use since not all of them could be calculated in NLTE if computation times are to remain reasonable (see section 3). Identifications of the emission lines show that by far most of them are Fe I lines. For more detailed informations on the emission lines seen on the different stars we provide a catalog of emission line identification in the appendix.

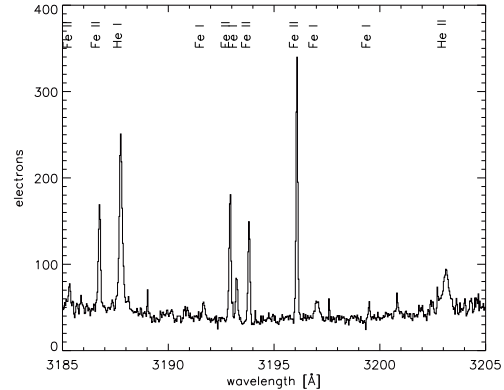


Fig. 1. A typical blue part of the spectrum of CN Leo around 3200 Å. The emission lines belong to Fe I, Fe II, He I and He II.

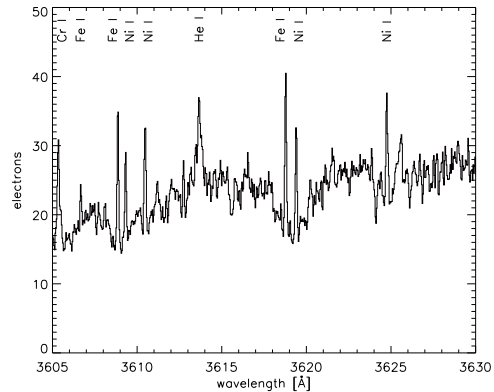


Fig. 2. Same as is Fig. 1 around 3600 Å. The emission lines belong to Ni I, Fe I, Cr I and He I.

## 3. Model construction and calculation

The model atmospheres consist of an underlying photosphere in radiative equilibrium, a chromosphere and part of the TR with a given temperature rise. All computations were carried out with the atmosphere code PHOENIX v13.7 (Hauschildt et al. 1999). For computations of M dwarfs chromosphere the proper NLTE treatment of the considered species and the background opacities are especially important (Andretta et al. 1997), both of which are provided by PHOENIX. Drawbacks in the chromospheric computations with PHOENIX are that no coronal flux is – yet – incorporated and that all lines are computed with the assumption of complete redistribution. Partial redistribution is especially important for the Ca H and K lines and for  $Ly_{\alpha}$ ; therefore none of these lines has been used in the modelling. Another assumption generally made in semi-empirical chromosphere modelling is hydrostatic and ionisation equilibrium throughout the atmosphere. This assumption has been challenged recently for the Sun (e. g. Carlsson & Stein

**Table 1.** Parameters of the underlying photospheres for the model construction. From the literature we also cite  $[A/H]$  given in brackets.

star	other name	spectrum used	$T_{\text{eff}}$ [K]	$\log g$	literature
AD Leo	GJ 388	2002-03-16 03:40:47	3200	4.5	3350, 4.5 (-0.75) <sup>1</sup>
YZ CMi	GJ 285	average	3000	4.5	2925 <sup>3</sup>
CN Leo	GJ 406	2002-03-14 03:24:38	2900	5.5	2900, 5.0 (0.0) <sup>1</sup>
DX Cnc	GJ 1111	average	2700	5.0	2850, 5.25 (+0.5) <sup>1</sup> ; 2775 <sup>3</sup>
LHS 3003	GJ 3877	average	2500	4.5	2400-2650 <sup>2</sup>

<sup>1</sup> Jones et al. (1996)<sup>2</sup> Leggett et al. (2002)<sup>3</sup> Mohanty & Basri (2003)

2002), but there are no detailed hydrodynamic chromospheric simulations for M dwarfs available.

### 3.1. The underlying photospheres

For the photospheres we used the best fit models to the red part of the UVES spectra which was determined by a  $\chi^2$  technique. The model grid for the comparison ranged from  $T_{\text{eff}} = 2300 - 3700\text{K}$  and  $\log g = 4.0 - 5.5$  in steps of  $\Delta T_{\text{eff}} = 100\text{K}$  and  $\Delta \log g = 0.5$ . The photospheric  $\log g$  and  $T_{\text{eff}}$  parameters determined in that fashion are listed in Tab. 1. We used solar chemical composition for all modelling since little is known even for the photospheric abundances in M dwarfs. In principle an abundance analysis for the chromosphere is possible using the emission lines – provided the temperature structure for the star is known. Such a technique would be especially useful for the late-type M dwarfs where atomic photospheric lines are becoming rare.

### 3.2. Construction of the chromospheres

For the chromospheres we used the same ansatz as Short & Doyle (1997), i. e., a linear temperature rise vs.  $\log m$  with different gradients in the chromosphere and TR. For some models we deviated from the linear temperature rise in two different ways. For two stars we decided to alter the temperature structure in the lower chromosphere to obtain a better fit of the Na I D lines (see Fig. 4). This can be done without altering the flux in the other diagnostic lines too much and is based on the gradient of models that fitted the Na I D line better than the model that gives the best overall fit. In the other case we tried to compose the chromosphere of two linear segments, introducing a plateau in the upper chromosphere with the second linear part. This leads to significantly more flux in the Balmer lines and these models were all inferior to a single gradient temperature rise. However, the results of our modelling suggests, that deviations from the linear temperature rise may improve the fits, since different temperature gradients fitted different lines best. For this paper we decided to stick to the linear temperature rise, though and obtain an overall best fit. The top of the chromosphere is chosen at 8000 K for all models since for higher temperatures hydrogen is no efficient cooling agent any more (Ayres 1979).

### 3.3. Construction of the TR

The TR in our models extends up to  $\log T = 5.0$ . In principle the gradient in the TR should be given by Spitzer conduction. Since conduction is balanced by the emerging flux from the TR, the gradient can be computed if the flux from the TR is known. For late type M dwarfs there are very few measurements for UV fluxes for temperatures below  $\log T = 5.0$ . Therefore we decided to model the TR temperature gradient as a function of the logarithmic column mass ( $\log m$ ) semi-empirically as well, using the parameter  $\log \frac{dT}{d \log m}$ . Balancing the conductive energy flux given by  $\kappa_0 T^{5/2} \frac{dT}{ds}$  (e. g. Mihalas 1978) with the emerging radiation one obtains

$$\frac{d}{ds} \left( \kappa_0 T^{5/2} \frac{dT}{ds} \right) = n^2 P(T)$$

with  $P(T)$  denoting the cooling function of a hot radiating plasma,  $T$  the temperature and  $\kappa_0 \approx 8.0 \cdot 10^{-7}$  in cgs units (Mihalas 1978). On neglecting the term involving second derivatives this leads to

$$\frac{dT}{d \log m} = m T^{-3/4} P(T)^{1/2} \cdot \text{const}$$

Since  $P(T) \sim T^{3/2}$  for  $20000 < T < 100000$  and  $m$  is about constant in the TR our ansatz  $\log \frac{dT}{d \log m} = \text{const}$  is in good agreement with a conduction dominated energy transport. The gradients we find in the best fit models also agree with the gradients found by Jordan et al. (1987) for G/K dwarfs in the 50000 to 100000 K regime inferred from the emission measure distribution.

### 3.4. Treatment of turbulent pressure

The chromosphere models are computed in hydrostatic equilibrium on a given column mass grid including convection and turbulent pressure. The treatment of the turbulent velocity  $\xi$  and the resulting pressure is crucial for the models. We first used  $\xi = 2\text{km s}^{-1}$  in the photosphere and a linear rise to  $10\text{km s}^{-1}$  at the top of the chromosphere continuing into the whole TR. However, the models with  $T_{\text{min}}$  at higher pressure do not converge for a linear turbulent velocity rise since it attains a significant fraction of the sound velocity or even becomes larger than the sound velocity in individual layers. Therefore the high pressure models are only possible for a description of the turbulent velocity as a fraction of the sound velocity. We chose  $\xi$  as  $0.5 v_{\text{sound}}$ . For the same model  $\xi = 0.7 v_{\text{sound}}$  produces lower emission lines than  $\xi = 0.5 v_{\text{sound}}$  in the Balmer series and lower emission cores with self absorption for the Na I D lines. This is

due to the lower electron pressure in the high turbulence velocity model as discussed by Jevremović et al. (2000). A turbulent velocity of  $2 \text{ km s}^{-1}$  is applied to all photospheric layers in all our models.

### 3.5. NLTE treatment

Moreover we took into account NLTE effects for various species. The models presented here normally treat H, He, C I - III, N I - III, O I - III, Fe I - IV, Ti I - Ti II, Na I - IV and Mg I - III in NLTE. For some tests different NLTE sets of ions are chosen, which will be pointed out for these models. All NLTE computations take into account all levels from the Kurucz database (Kurucz & Bell 1995) or from the CHIANTI database (Young et al. 2003) for C V to C VI, N VII and O V to O VIII and Fe VI to Fe VII. Since NLTE computations show that the level populations of most species and especially hydrogen are far from LTE we also took into account scattering for the LTE background lines, since not all lines can be computed in NLTE. The scattering of the background lines is treated by choosing the  $\varepsilon$  parameter in the relation  $S = \varepsilon B + (1 - \varepsilon)J$ , where  $S$  is the source function,  $B$  the Planck function and  $J$  the mean intensity. If no scattering is included, i. e.  $\varepsilon = 1.0$ , we obtain unrealistically high emission in the Balmer lines for moderate chromospheres and for stronger chromospheres even a Balmer jump and significant Balmer continuum, which is not observed in any of our spectra. Since the NLTE level population strongly deviates from the LTE level population in the chromosphere one would expect a lower value of  $\varepsilon$ . Therefore we lowered  $\varepsilon$  to 0.5 and to 0.1. The latter value gave no Balmer jump and realistic Balmer line emission. Therefore we used  $\varepsilon = 0.1$  for all the model computations. Since the  $\varepsilon$  grid is rather coarse, the uncertainties in this parameter are large. The model spectra needed clearly  $\varepsilon < 0.5$  to avoid producing a Balmer jump, but for  $\varepsilon < 0.5$  it should be possible to balance the emergent emission with a TR onset at lower column mass. For the best fit model of AD Leo we computed also a model with  $\varepsilon = 0.2$  which would lead to a lowering of the column mass at the onset of the TR of about 0.1 dex.

### 3.6. Filling factors

All models are computed in spherical geometry. This means that we assume an atmosphere with a filling factor of hot material of 100 percent. For the Sun this assumption is under debate since the discovery of cool CO in chromospheric layers which lead to thermally bifurcated atmosphere models (e. g. Ayres & Rabin 1996). For M dwarfs measured magnetic filling factors are often very high: e. g. Saar & Linsky (1985) measured that about 73 percent of the surface of AD Leo is covered with active regions. For two other very active M4.5 stars Johns-Krull & Valenti (1996) found magnetic filling factors of  $50 \pm 13$  percent. We tried to infer chromospheric filling factors a posteriori (see section 6.4).

### 3.7. Lines used for fitting

To determine the quality of the fits different lines were chosen for the hotter and brighter stars AD Leo, YZ CMi and CN Leo as compared to the cool and very faint stars DX Cnc and LHS 3003. For the three mid-type M dwarfs we used the Balmer line series higher than  $H_9$ , the Na I D lines and a number of Fe I and Mg I lines between 3650 and 3870 Å. An additional pronounced chromospheric feature is the He I line at 5875 Å, which could not be matched for any of the three stars without creating too much flux in the Balmer lines. We ascribe this to our relatively simple approach with nearly linear temperature distributions in the chromosphere and a linear temperature distribution in the TR. This problem applies not only to the He line, but to other lines as well: it is hard to match large parts of the spectrum well with the same model. Therefore our best fit models match most of the lines in principle but not perfectly.

For the two late-type M dwarfs we used the  $H_\alpha$  and the  $H_\beta$  line, the Na I D lines and the He I line at 5875 Å since the blue part of the spectra were underexposed for the two stars.

## 4. The influence of the model parameters

Before studying the five M dwarfs and their best fit model in detail a few words about the influence of the general model parameters and assumptions are in order.

### 4.1. Photospheric parameters

The influence of the underlying photospheric model and its parameters  $T_{\text{eff}}$  and  $\log g$  has been studied already by Short & Doyle (1998). They find that lowering or raising  $T_{\text{eff}}$  by 200 K or  $\log g$  by 0.5 dex leads to uncertainties in the chromospheric parameters of the column mass at the onset of the TR or at the temperature minimum of about 0.3 dex. Therefore we used individual photospheric models for each star. Nevertheless we confirm the trend they found comparing the models of AD Leo and YZ CMi (see section 5.2).

Regarding the quality of our photospheric models we estimate the error in  $T_{\text{eff}}$  to be about 100 K, since the variation of this parameter led to significant changes in  $\chi^2$ . A comparison of our  $T_{\text{eff}}$  values to those published in literature does indeed show agreement to within 100 K (see Table 1). We also estimate the error in  $\log g$  to be about 0.5 dex.

The influence of the stellar mass of the underlying model has not yet been studied to our knowledge. We computed models with 0.5 and 0.1  $M_\odot$  for our lowest mass star LHS 3003 and found only very weak dependence on this parameter (see section 5.5). Also the influence of metallicity on the chromospheric emission has not been studied so far. Fig. 7 strongly suggests, that metallicity should be included in future modelling if it uses metal lines as diagnostics.

### 4.2. Chromospheric parameters

The microturbulence has been shown by Jevremović et al. (2000) to influence the line intensity as well as line shape. The influence of NLTE computations has been found in this article

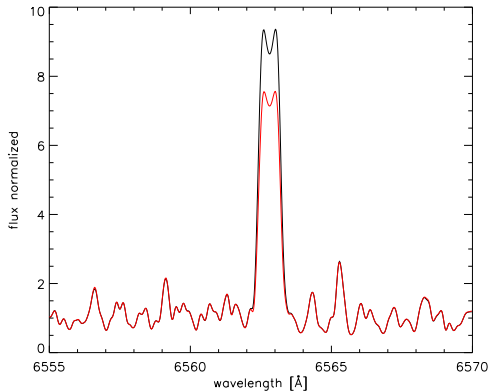


**Fig. 3.** Comparison of two models with dust (black) and without dust (red). The continuum is normalized for both models, otherwise the difference in the  $H_{\alpha}$  line would cease.

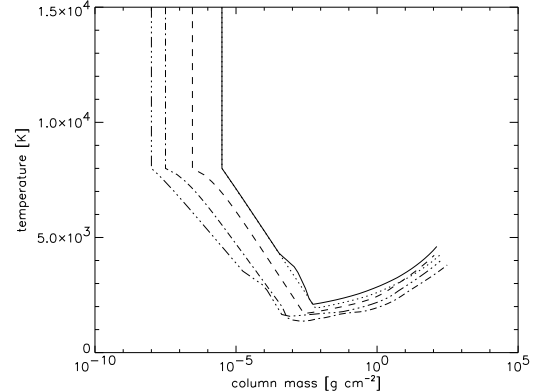


**Fig. 4.** Temperature structure for our best fit models. The solid line corresponds to AD Leo, the dotted line to YZ CMi, the dashed line to CN Leo, the dot-dashed line to LHS 3003 and the triple-dot-dashed line to DX Cnc. The models for AD Leo and YZ CMi are nearly identical.

to have not only an influence on emergent flux of the considered species itself, but on other species as well (see section 6.1).

The partial frequency redistribution approximation has not been implemented in PHOENIX so far. Falchi & Mauas (1998) studied the impact of partial compared to complete frequency redistribution (PRD/CRD) on the  $Ly_{\alpha}$  line. They found that the PRD treatment of  $Ly_{\alpha}$  also influences the Balmer lines. The CRD approximation leads to more emergent flux, therefore our models should have the onset of the TR at too low a pressure compared to a model computed in PRD.

For the cool models with  $T_{\text{eff}} = 2700$  K and 2500 K dust may play an important role since it warms the atmosphere in photospheric layers and is an efficient scatterer. For the photospheric spectra themselves the influence of dust is not significant. For the chromospheres we tried two different dust treatments usually used within PHOENIX. In the first approach the dust is treated only in the equation of state, in the second approach the dust is also included in the opacity calculations. While the first approach does not affect the emission lines, the second approach enhances most of the emission lines and lowers the continuum. A comparison can be seen in Fig. 3. Although dust has an impact on the chromosphere modelling we did not use it in the present work since it slows down the computation significantly.

As a last point the use of a linear temperature rise vs. log column mass in the chromosphere should be discussed. Alternatively one could use a non-linear temperature rise as was done by Mauas (2000) or Vernazza et al. (1981) for the Sun using several diagnostics to model different parts of the temperature rise. If there are enough diagnostic lines that correspond directly to the temperature at a certain column mass this is undoubtedly more sensitive to the temperature structure and should give better agreement between data and models. Since NLTE effects play an important role and therefore certain lines can be affected by the radiation of layers far away from their formation depth this is also a more complicated way to build

chromospheres. Therefore we refrained from a non-linear temperature rise at the moment.

## 5. Results

The temperature distribution for the best fit models is shown in Fig. 4 for all of the stars and an approximate line formation depth is given for various lines for the model of AD Leo in Fig. 5. The pronounced emission line of He I at  $5875 \text{ \AA}$  is not indicated since the model of AD Leo does not show this line. For the determination of the line formation depth we used spectra for each layer in the atmospheric model. The formation of the resulting spectrum in the outermost layer can be observed from layer to layer. One problem with this ansatz is that the net flux is tracked, i. e. the flux going inward is accounted for as well. Therefore the outer boundary of the line formation region can be determined quite well whereas the inner boundary is less certain.

Since for all our observed spectra of the mid-type M dwarfs the Na I D lines are found as absorption lines with emission cores, the minimum seen in the line profiles can serve as a diagnostic for the location of the temperature minimum in the star's atmosphere (as proposed by Andretta et al. (1997) and Mauas (2000)). We also find like Andretta et al. that the Na I D line profile is insensitive to the TR gradient. For the three early-type M dwarfs the models show pronounced self absorption in the emission core, which is not seen in the spectra, otherwise the Na I D lines are reproduced reasonably well for these stars (see e. g. Fig. 9 for YZ CMi). For the two late-type M dwarfs the Na I D lines are less well suited to diagnose the temperature minimum since the absorption profile is quite shallow; this is especially true for LHS 3003.

The best fit was determined in two ways, by eye and with a  $\chi^2$  test using a number of wavelength ranges including the diagnostic lines. For LHS 3003 and DX Cnc the used wavelength

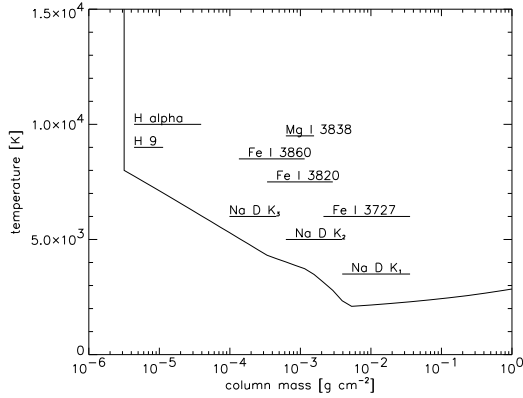


**Fig. 5.** Temperature structure for our best fit models of AD Leo. Given are the approximate line formation depths for various lines used in the fitting process.

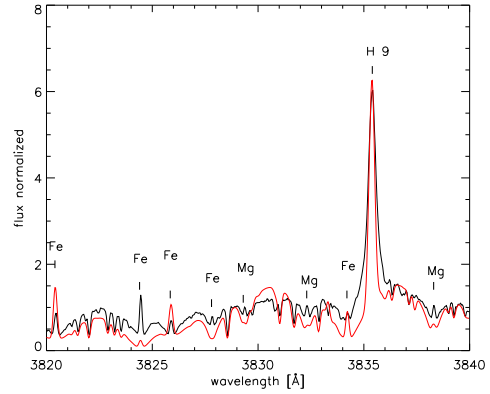


**Fig. 6.** Comparison of the observed spectrum of AD Leo (black) and the best fit model (grey/red). The emission cores/lines used for the modelling are indicated in the spectrum.

ranges are 4855 to 4865, 6550 to 6570, 5873 to 5877 and 5888 to 5900 Å. For AD Leo, YZ Cmi and CN Leo the  $H_{\alpha}$  region was omitted and, instead, some of the blue wavelength were used: 3705 to 3728, 3825 to 3840, 3780 to 3810 and 3850 to 3865. In the case of AD Leo and YZ Cmi both the eye fit as well the  $\chi^2$  fit resulted in the same best fit model. For CN Leo the  $\chi^2$  test best fit model differed by 0.1 dex in the TR gradient to the one found by eye, i. e. they are neighbouring models. Also for DX Cnc and LHS 3003 the  $\chi^2$  test preferred neighbouring models to the by eye fit. We decided to use the models found by eye since for LHS 3003 the  $\chi^2$  test was contaminated by the Na D airglow lines and for DX Cnc we preferred to describe the  $H_{\alpha}$  line more correctly than the  $H_{\beta}$  line (which is the main difference between the two models).

We stopped improving the models when the variation of the three main parameters (column mass at  $T_{\min}$ , column mass at onset of TR and grad TR) around some starting parameters did not improve the fit. However, no true grid in the parameter space was calculated, since we normally adjusted first the column mass at  $T_{\min}$  via the Na D lines, then varied the column mass at the onset of the TR, readjusted the column mass at  $T_{\min}$  and then varied the gradient of the TR.

### 5.1. AD Leo

A comparison between model and data for the blue part of the spectrum of AD Leo is shown in Figs. 6 and 7. The complex pattern of pure emission lines and absorption lines with emission cores is reproduced quite well, although the amplitude of most of the lines is not perfectly modelled. The base of the Balmer lines is somewhat broader than in the model but in general the Balmer lines fit reasonably well in amplitude and highest Balmer line seen. Iron lines can be either too strong or too faint, but normally lines from the same multiplet behave in the same way. For example, the three Fe I lines at 3820, 3826 and 3834 Å are all three from the same multiplet and too strong, while the Fe I lines at 3705.5, 3720 and 3722.5 Å from another

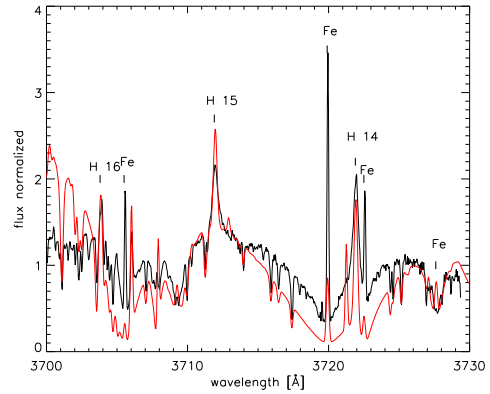


**Fig. 7.** Same as in Fig. 6. The absorption part of the Fe I line at 3720 Å, is too pronounced in the model what may be due to metallicity.

multiplet are all too faint. Since the deviation of the lines do not vary randomly it is unlikely that it is caused by a lack of reliable atomic data; but even so one should keep in mind that especially the collision rates are usually not well known. The behaviour may be caused by our simple temperature structure. While the 3720 Å line originates in layers corresponding to temperatures between 4500 and 3500 K, the 3820 Å line originates in layers corresponding to temperatures between 3800 and 2800 K. The formation depths are overlapping with the 3820 Å line forming in deeper layers. An alteration of the temperature structure in these layers should improve the fit of these lines. Nevertheless NLTE effects also play a role for these lines, since their amplitudes reacts to the gradient in the TR as well.

### 5.2. YZ CMi

For YZ CMi a comparison between model and data can be found in Figs. 8 and 9. The Balmer lines are well fitted in amplitude. Also described correctly is the highest Balmer line that is clearly seen in emission. The base width of the Balmer lines is too narrow in the model. This is worse than for AD Leo and comparable to CN Leo. Since YZ CMi is relatively stable through the observations, pronounced activity is no obvious explanation for this. Since all three stars are very active this discrepancy may be caused by spiculae-like inffws and outffws (see also sect. 5.5).

As AD Leo, YZ CMi shows a pattern of absorption lines with emission cores which is in general reproduced well. The two stars are very similar, which is reflected in the similar models that differ only by 0.1 dex in the column mass at the temperature minimum and by 0.2 dex in the gradient of the TR. Judging from the spectra (observed or modelled), YZ CMi is the more active star since it shows more emission lines with larger equivalent width. Nevertheless, AD Leo is described by the more active model judged by the temperature minimum located at higher column mass and the lower gradient in the TR. However in combination with the higher effective temperature of the photospheric model, it actually gives lower amplitudes in the emission lines. Even a temperature difference of 200 K in the effective temperature of the photosphere can significantly influence the emergent chromospheric flux. Hence a good knowledge of the parameters of the underlying photosphere is essential for chromospheric modelling.

Although the wings of the Na I D lines are fitted reasonably well, the region between the doublet lines is not. This region is sensitive to the temperature minimum and the temperature structure in the low chromosphere, but it is also sensitive to changes in the microturbulent velocity. Also there are deep self-absorption cores in the Na I D lines seen in the models. This may be caused by a wrong temperature structure in the mid chromosphere, where the flux in the line center of the Na I D lines arises (see Fig. 5), but the depth of the self-absorption core in the Na I D line is also strongly dependent on the NLTE set chosen. It may therefore be a pure NLTE effect. In this case there is no strong connection between the temperature structure of a certain part of the model and the strength of the self-absorption.

### 5.3. CN Leo

CN Leo is the most active star in the sample and has accordingly the worst fit for the individual lines. Nevertheless the disappearance of the absorption lines in favour of pure emission lines is reproduced. While the only 100 K hotter photosphere of YZ CMi produces many absorption lines with emission cores, the spectrum of CN Leo exhibits pure emission lines - which is fully reproduced by the model.

While the amplitudes of the Balmer lines and the highest Balmer line seen are fitted quite well by the model, the observed Balmer lines are much broader at the baseline than the ones in the model (see Figs. 10 and 11). Although the spectrum used for the modelling is obtained during quiescence there may

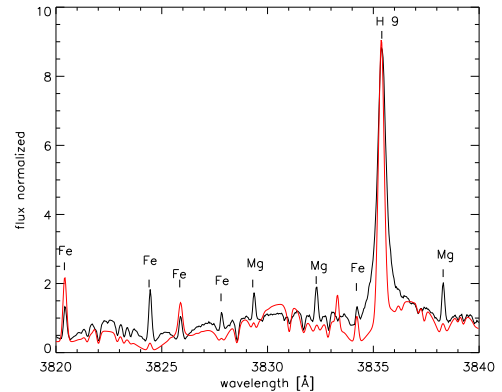


**Fig. 8.** Comparison of the observed spectrum of YZ CMi (black) and the best fit model (grey/red). The  $H_{\beta}$  is reproduced quite well. The Mg I lines show all less pronounced emission features in the model compared to the data.

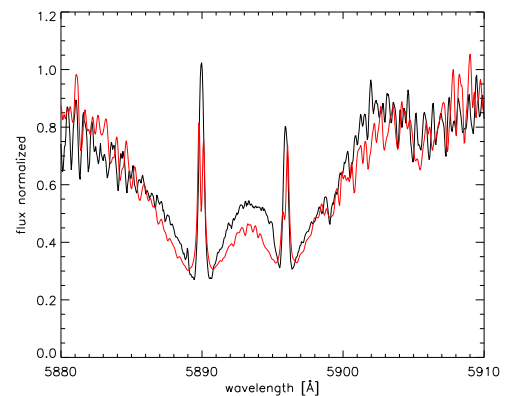


**Fig. 9.** Same as is in Fig. 8 but for the Na I D lines. While the model shows deep self-absorption this is not seen in the data.

be some activity present providing an additional broadening mechanism. Moreover most of the Fe lines in the model are too strong compared to the data if the Balmer lines are fitted well. On the other hand, models with well fitted iron lines yield too much Balmer line flux. Fig. 5 shows that the Fe lines are forming in the middle and lower chromosphere, while the Balmer lines originate from the top of the chromosphere. Therefore a non-linear temperature rise could help to solve this discrepancy. Again the model does not predict He emission lines. This incorrect modelling of the He D<sub>3</sub> line may be caused by the non-inclusion of a corona in our models as suggested by the work of Mauas et al. (2005).

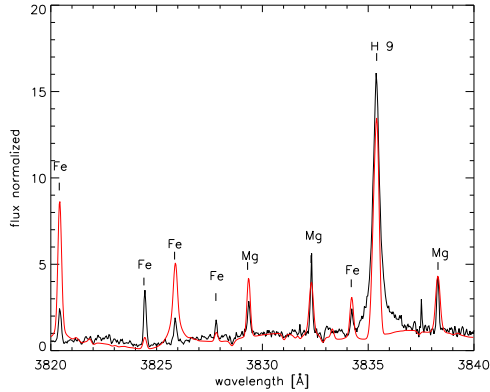


**Fig. 10.** Comparison between data (black) and model (grey/red) for CN Leo. Most of the Fe lines are too strong in the model.

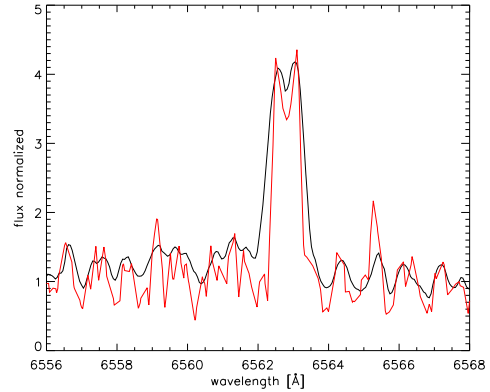


**Fig. 12.** Comparison of data of DX Cnc (black) and best fit model (grey/red) for the  $H_\alpha$  line. The model shows too deep self-absorption.

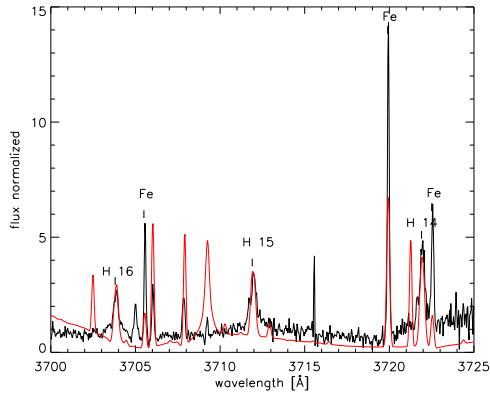


**Fig. 11.** Same as is in Fig. 10. Again the Fe lines are too strong while the three Balmer lines  $H_{14}$  to  $H_{16}$  are fitted quite well.

#### 5.4. DX Cnc

While the  $\text{He I}$  line at  $5875 \text{ \AA}$  emission line is not predicted by the models for the three mid-type M dwarfs, for the two late-type M dwarfs the line is too strong in the models. The emission cores of the  $\text{Na I D}$  doublet are far too faint for this star using the linear temperature rise that fit the Balmer lines well (see Fig. 12). Therefore we modified the lower chromosphere temperature structure and started with a higher gradient directly at the temperature minimum, but joined the original temperature rise at about  $4000 \text{ K}$  before hydrogen starts to ionize. This leaves the Balmer lines nearly unaltered and gives stronger emission cores in the  $\text{Na D}$  doublet.

#### 5.5. LHS 3003

While all other stars were computed with  $0.5 M_\odot$ , LHS 3003 was computed with  $0.1 M_\odot$  because of its low effective temperature and surface gravity and to test the influence of the mass

on the chromospheric model. While a higher mass produces a higher  $\text{Ly } \alpha$  line, the Balmer series lines are slightly lower. Therefore we conclude that the star's mass in the model has an influence on the chromospheric model but the effect is small compared to other parameters and NLTE effects.

While the amplitude of the  $\text{Na I D}$  lines is well fitted, the lines are too wide at the line base in the model (see Fig. 14). The width of the line is also not fitted well for the  $H_\gamma$ , and for the  $H_\beta$  line: These two lines are too narrow in the model as can be seen in Fig. 13 for the  $H_\alpha$  line. This may be due to the rotational velocity of the star. To test this hypothesis we spun up the model to  $20 - 30 \text{ km s}^{-1}$  to fit the line width of the  $H_\gamma$  line. On the other hand, we measured the rotational velocity of LHS 3003 in the photospheric lines using CN Leo as a template (see Fuhrmeister et al. (2004) for the method used); this procedure leads to a rotational velocity of  $6.0 \pm 1.5 \text{ km s}^{-1}$ . If one compares the photospheric features in Fig. 13 next to the  $H_\alpha$  line to the model (with no rotation at all), a slow rotational velocity seems to be very reasonable. Moreover this additional broadening is not seen in other emission lines e.g. the  $\text{Na I D}$  lines. Therefore rotational broadening can be ruled out and the chromospheric emission line must be affected by another broadening mechanism. The modelling includes Stark and van der Waals broadening approximations. The self-broadening of the Balmer lines may, however, not be described correctly (Barklem et al. 2000). Another possibility ascribes the additional broadening to a more dynamic scenario with mass motions. If the star hosts several active regions exhibiting mass motions, the overlapping of the lines would lead to an additional broadening. Also spiculae-like infbws and outfbws may contribute to Balmer line broadening as described for II Peg by Short et al. (1998). A dynamic scenario would also explain the asymmetric profile of both the  $H_\gamma$  and the  $H_\beta$  line in the star, which is not reproduced by any of our models. Since the  $H_\alpha$  line shows two prominent components we tried to fit the line with two Gaussians leading to Doppler shifts of  $-11 \text{ km s}^{-1}$  and  $16 \text{ km s}^{-1}$ , respectively, where we used  $6562.81 \text{ \AA}$  as reference central wavelength. The  $H_\beta$  line is not composed of two com-

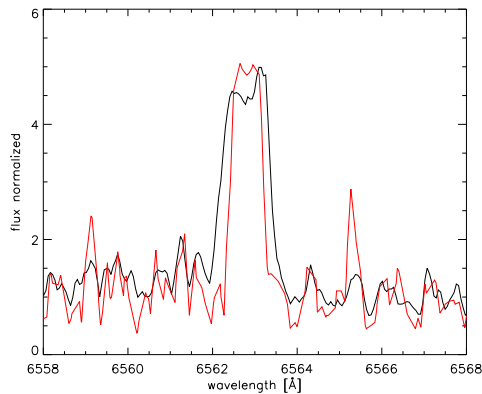


**Fig. 13.** Comparison of data of LHS 3003 (black) and the best fit model (grey/red) for the  $H_\alpha$  line. Here the self-absorption in the model is not deep enough.

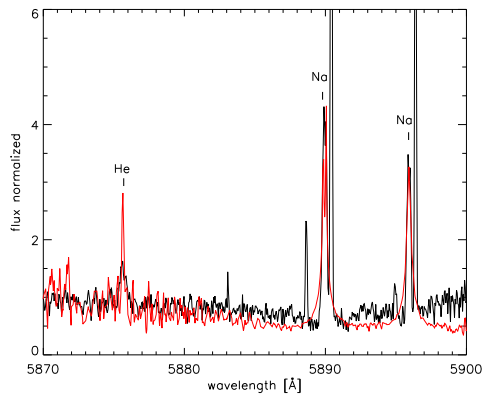


**Fig. 14.** Same as in Fig. 13 but for the Na I D lines and the He I line at 5875 Å. The narrow emission lines are known airglow lines that have not been removed (see also Fig. A.1).

ponents, but fitting it with three Gaussian components leads to one component at about rest wavelength and two components with Doppler shifts of about  $-11 \text{ km s}^{-1}$  and  $18 \text{ km s}^{-1}$  using  $4861.33 \text{ \AA}$  as rest wavelength. Moreover the three averaged spectra show some changes during the time series in the line profiles of the two Balmer lines. Since the photometer shows no major flaring activity it seems that the quiescent activity of LHS 3003 is composed of different active regions.

## 6. Discussion

### 6.1. NLTE effects

The line flux and the line profile are both sensitive to NLTE effects. Therefore it is necessary to compute at least all species in NLTE whose lines are used for the model fitting. Lines computed in LTE usually show too strong emission as in Fig. 15.

However, the lines are not only influenced by the NLTE calculations of the line forming species itself but by other species as well. For example, the Balmer lines and the Na I D lines are influenced by the NLTE computations of carbon, nitrogen and oxygen (CNO). Therefore as many species as possible should be treated in NLTE. To investigate the influence of different species on each other, we computed for YZ CMi model atmospheres and spectra with different NLTE sets. Hydrogen, helium and Na I to Na IV were always computed in NLTE. In addition we computed the same model with CNO I to CNO III in NLTE, and with C I to VI, N I to N V, O I to VI in NLTE. The latter NLTE set was chosen to cover all ions of CNO with significant partial pressures in the temperature domain below  $\log T = 5.0$ . Moreover we computed the same model with different less abundant metals in NLTE (in addition to CNO I to CNO III): One set chosen was Fe I to Fe VII, Mg I to Mg IV and Ni I to Ni III, the other one Fe I to Fe IV and Co I to Co III. The latter two models did not differ significantly in the Balmer lines nor in the Fe I lines. The difference in the Na I D lines is less than about 10 percent. The electron density for these two models are very similar except in a region around the temperature minimum, which is seen in the variation of the Na I D lines in the spectrum. The comparison of one of these two models with CNO I to CNO III in NLTE shows much larger differences both in the electron density and in the spectrum. Therefore we conclude, that it is important to treat at least Fe I to Fe IV in NLTE. The largest changes can be seen in the amplitudes of the higher Balmer lines and in the Na I D lines which is about 30 percent while for the  $H_\alpha$  and  $H_\beta$  line the difference is about 10 percent.

Even more important is the influence of the treatment of the CNO ions. Between no CNO NLTE treatment at all and the first two ions in NLTE the amplitudes of the Balmer lines change dramatically. While for the  $H_\gamma$  line the amplitude is about doubled, the amplitude of the  $H_\beta$  line is about halved, the amplitude of the Na I D lines is also about halved. For further CNO ions treated in NLTE the flux in the  $H_\alpha$  and  $H_\beta$  line decays further, while the amplitude of the Na I D lines and the higher Balmer lines stays nearly constant. The treatment of the higher CNO ions in NLTE is very problematic since these ions are in principle not present in most parts of the atmosphere and therefore the code must deal with very tiny numbers.

The compensation for the additional flux in the models with the large NLTE sets were usually done via adapting the gradient in the TR. Typically this gradient had to be increased for about 0.2 dex to compensate for the additional emergent flux in the Balmer series.

One explanation of this effect is through the direct influence of the NLTE calculations on the electron density: NLTE calculations of one species influence the electron density and therefore the level population of all other species. Another possibility is the influence of a species with a multitude of lines in the hydrogen continuum region which would influence the hydrogen ionisation equilibrium and therefore indirectly the electron density. Since cobalt and nickel have many lines in the hydrogen continuum region and these species do not influence the electron density too much, this seems to be a second order effect compared to the direct influence of the electron density via the ionisation balance of the more abundant elements (see

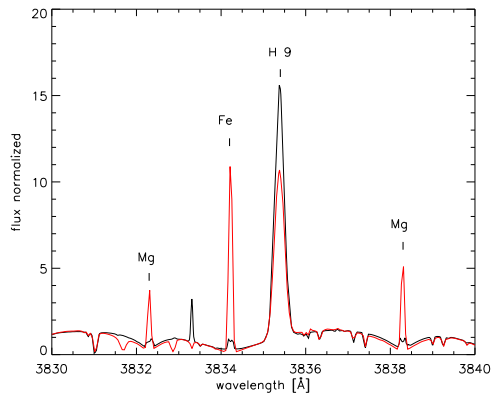


**Fig. 15.** Comparison of two computations with different NLTE sets. The line at 3835.4 Å is H<sub>9</sub>, the other lines are Fe I and Mg I. The Fe I and Mg I lines in the grey/red model often show much stronger line flux than in the black model since they are not computed in NLTE in the grey/red model. The H<sub>9</sub> line is influenced by the different NLTE sets of the two models, though hydrogen is computed in NLTE for both models. Further computations show that this is caused mainly by the different treatment of CNO in the two models.

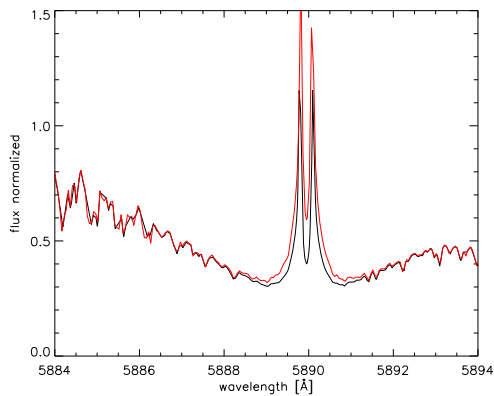


**Fig. 16.** Same comparison as in Fig. 15 for the Na I D line. The NLTE set that also includes Fe, Mg and CNO show shallower Na emission (black line) than the one that treats only H, He and Na in NLTE (grey/red line).

Fig. 17). On the other hand, the NLTE computation of the Fe ion levels influence the electron density in large parts of the atmosphere.

To gain some further insight in the NLTE behaviour of chromospheres we built a simple chromosphere model for the Sun that is supposed to be closer to LTE than M dwarfs. We computed a model with H, He and Ca I - v and a model with H, He, Ca I - III, CNO I - III, and Fe I - III in NLTE. The two models show very little differences in the Balmer lines and in the Ca II H and K line. The largest variation seen in these lines is about 10 percent which is indeed much less than in the M dwarfs.

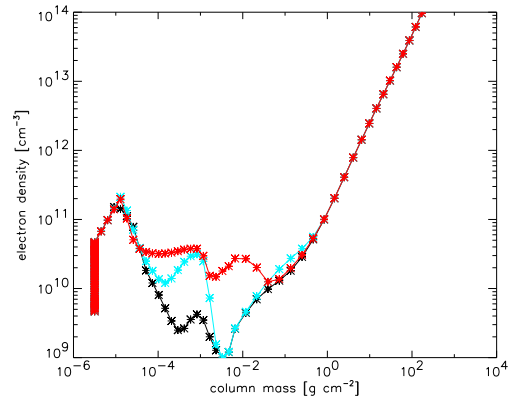


**Fig. 17.** Comparison of the influence of different NLTE sets on the electron density. The black line is the basic model with H, He and Na in NLTE. Grey/red is the model with Fe/Ni in NLTE and light grey/turquoise is the model with CNO I to CNO III in NLTE. All three models differ significantly in large parts of the atmosphere.

Therefore the strong variations due to the set of NLTE species chosen is characteristic of the M dwarf models. Although this does not rule out computational artefacts it strengthens our confidence in the reliability of the variations in the electron pressure and the spectral lines in our M dwarfs.

## 6.2. Uniqueness of the models

During our chromospheric modelling we encountered the problem of non-uniqueness of the models in several ways, but it could be resolved each time. Since the Na D lines are known to be only sensitive to changes in the lower chromosphere, clearly an additional diagnostic is needed. The Balmer lines are sensitive to changes in the upper chromosphere and the gradient in the TR. Nevertheless we found models with nearly identical Balmer lines either in the lines higher than H<sub>9</sub> or in H<sub>β</sub> and H<sub>α</sub> but normally not both. Therefore the very high Balmer lines seems to be an important diagnostic tool. Only for different NLTE sets the whole Balmer series can be nearly identical for different model parameters. Since e. g. the Fe lines are not reproduced correctly by a LTE treatment, the models can be distinguished by these lines.

Since we used only H<sub>α</sub>, H<sub>β</sub> and the Na D lines for the model construction of LHS 3003 and DX Cnc, these models may be affected by non-uniqueness. However since the emission lines react more sensitively to all chromospheric parameters when lowering T<sub>eff</sub> we do not regard this as a serious problem.

Another interesting point is to test if the photospheric parameters used may introduce some kind of non-uniqueness. Since AD Leo and YZ CMi have the most similar photospheric spectra in the sample, we tested if the spectrum of YZ CMi could be fitted with one of the model spectra created for AD Leo that has a hotter underlying photosphere than YZ CMi and the same log g. We found that the models with the hotter photosphere give poorer fits since a stronger chro-

mosphere was needed to match the Balmer lines, which led to too much flux in the metal lines. Since the chromospheric parameter space is designed for AD Leo, though, we may miss a well fitting model with a hotter photosphere for YZ Cmi.

### 6.3. Comparison to other models

Our hottest sample star AD Leo is the only one in our sample for which chromosphere models have been computed by other authors. Mauas & Falchi (1994) derived a semi-empirical model of the photosphere and chromosphere of the quiescent state of AD Leo fitting the continuum as well as some chromospheric lines. Hawley & Fisher (1992) constructed a grid of flare models for AD Leo including a quiescent one. These models were constructed on a photospheric base by using X-ray heating from a model for the overlying corona. Short & Doyle (1998) constructed chromospheric and TR models in a very similar way as our approach, using a linear temperature vs.  $\log m$  distribution. Moreover, all these authors used very different underlying photospheres. While Mauas & Falchi (1994) fitted both photosphere and chromosphere at the same time semi-empirically and no  $T_{\text{eff}}$  or  $\log g$  values were given, Hawley & Fisher used a model by Mould (1976) with  $T_{\text{eff}} = 3500$  K and  $\log g = 4.75$ , and Short & Doyle used a PHOENIX photosphere with  $T_{\text{eff}} = 3700$  K and  $\log g = 4.7$ . All authors used solar chemical composition as we did. Since the emission lines are sensitive to the underlying photospheres as mentioned above and discussed in Short & Doyle (1998), and due to the different construction all these models are difficult to compare. The models of Short & Doyle (1998) are very similar to our own models, although they used a photosphere considerably hotter. Accordingly they found a TR onset at higher pressure than we did.

### 6.4. Filling factors

Our one dimensional model atmospheres correspond to a 100 percent filling factor of chromospheric material. Nevertheless one can estimate the filling factor a posteriori. With distance and radius of the star known, the theoretical scaling factor between flux at the stars surface and flux at earth atmosphere can be calculated. This can be compared to the scaling factor between the model and the flux calibrated spectrum; the ratio of the two gives the filling factor of the chromosphere. We calculated the radius of the stars from the measured luminosity and the temperature of the photospheric model via  $L_{\text{bol}} = 4\pi R^2 \sigma T_{\text{eff}}$ . The largest uncertainty is caused by the flux calibrations since the standard star was observed only once per night. We estimate the error in the absolute fluxes to be as large as a factor of two. The calculated filling factors can be found in Table 2. Due to the possibly big errors in flux calibration the filling factors should be considered only as estimates, nevertheless, the three early and mid-type M dwarfs seem to have higher filling factors than the two late-type dwarfs.

The low chromospheric filling factors of the two late-type M dwarfs imply that one-dimensional model calculations may be a poor approximation, since a significant portion of the en-

ergy in the active regions will be radiated away horizontally. Therefore stronger chromospheres than we have inferred here may be embedded in cool material. For proper simulations of such a chromosphere three-dimensional hydrodynamical simulations would be needed, as is done for the Sun, e. g. by Wedemeyer et al. (2004).

## 7. Summary and conclusion

We have presented the first semi-empirical models for mid- and late-type M dwarfs accounting for Fe I lines. We found that the models are able to fit the transition from absorption lines with emission cores to pure emission lines at about 3000/2900 K effective temperature. Moreover we found models for five individual stars with effective temperature between 3200 and 2500 K that fit many spectral features reasonably well. We found for Fe I lines from the same multiplet that they normally behave the same way: The model predicts too high or too shallow amplitudes for all of them. Therefore some of the multiplets may be used to obtain more complex temperature distributions that are able to fit the spectral lines even better.

Moreover we investigated the behaviour of the emerging spectrum under NLTE calculations of different species and found a large influence especially of CNO, that may alter the Balmer and Na I D lines significantly. There is far less NLTE crosstalk caused by species like Co, Ni and Ti.

For the two late-type M dwarfs DX Cnc and LHS 3003 we studied the behaviour of the models if dust is considered and found that dust can affect the emerging emission lines if it is considered not only in the equation of state but also in the opacity calculations.

These very late type objects can be described by the same type of chromospheric model atmosphere as the earlier M dwarfs except that the onsets of the chromosphere as well as the TR move to lower pressure. Thus, there seem to be no principal differences in the heating mechanisms of the chromospheres down to M7. This is relevant in the context of the ongoing discussion about the decreasing activity of the very late-type objects and in particular whether they have possibly only transient chromospheres and coronae. Since the decrease in activity starts at around M7, even more late-type objects than hitherto investigated should be included in chromospheric modelling attempts.

We therefore conclude that modelling of chromospheres with semi-empirical deduced temperature distributions relies heavily on correct input parameters and model assumptions such as effective temperature of the photosphere,  $\log g$ , NLTE treatment of important lines and dust treatment for the coolest stars. Another parameter probably as important as the others is the metallicity which is normally not considered in chromospheric modelling.

*Acknowledgements.* Most of the model computations were performed at the Norddeutscher Verbund für Hoch- und Höchstleistungsrechnen (HLRN) and at the Hamburger Sternwarte Apple G5 cluster financially supported by a HBFUG grant.

B. Fuhrmeister acknowledges financial support by the Deutsche Forschungsgemeinschaft under DFG SCHM 1032/16-3, and thanks A. Schweitzer for numerous discussions that contributed to this work.

**Table 2.** Filling factors of the chromospheres for the modelled stars and the parameters used to calculate the filling factors. The measured scaling factor  $f_m$  between model and flux calibrated spectrum is given as well as the theoretical scaling factor  $f_{th} = R^2/d^2$ .

star	$\log L_{bol}$	radius [cm]	distance [pc]	$f_m$	$f_{th}$	filling factor
AD Leo	31.94 <sup>1</sup>	3.4 10 <sup>10</sup>	4.9 <sup>1</sup>	3.0 10 <sup>-26</sup>	5.3 10 <sup>-26</sup>	0.57
YZ CMi	31.69 <sup>1</sup>	2.9 10 <sup>10</sup>	6.1 <sup>1</sup>	1.7 10 <sup>-26</sup>	2.5 10 <sup>-26</sup>	0.68
CN Leo	30.55 <sup>1</sup>	8.4 10 <sup>9</sup>	2.4 <sup>1</sup>	0.7 10 <sup>-26</sup>	1.4 10 <sup>-26</sup>	0.50
DX Cnc	30.48 <sup>1</sup>	8.9 10 <sup>9</sup>	3.6 <sup>1</sup>	1.7 10 <sup>-27</sup>	6.6 10 <sup>-27</sup>	0.26
LHS 3003	30.31 <sup>2</sup>	8.5 10 <sup>10</sup>	6.4 <sup>3</sup>	0.5 10 <sup>-27</sup>	1.9 10 <sup>-27</sup>	0.26

<sup>1</sup> Delfosse et al. (1998)<sup>2</sup> Leggett et al. (2002)<sup>3</sup> Dahn et al. (2002)

PHH was supported in part by the Pôle Scientifique de Modélisation Numérique at ENS-Lyon.

## Appendix A: Identification of chromospheric emission lines

Chromospheres of M dwarfs exhibit hundreds of emission lines especially in the near UV between 3000 and 4000 Å. These lines can even be multiplied during flares. Deciding which lines to use for the chromospheric modelling made us produce an extensive emission line list for the near UV and optical. We restricted that list not to the 5 modelled M dwarfs but used the whole sample of 21 late-type stars and brown dwarfs. 506 different emission lines of the elements H, He, Na, Mg, Al, Si, K, Ca, Sc, Ti, Cr, Mn, Fe, Co, Ni could be identified, revealing the different levels of activity in the stars.

The observation parameters can be found in Tab. A.1. For further information about the observations and the data analysis see the article above or Fuhrmeister et al. (2004).

IRAF was used to measure the central wavelength, FWHM and the equivalent width (EW) of the emission lines. We decided to fit the background by eye since otherwise emission cores could not be treated and there are wavelength ranges where the lines are so crowded that it is hard to find appropriate pseudo-continuum points. Therefore the EW measurements are affected by a rather large error. For single lines in spectral wavelength ranges with an ill defined continuum this error may be as big as a factor of two, but for most lines it is less than 40 percent.

We identified the emission lines with the help of the Moore catalog (Moore 1972). Few lines were identified via the NIST database<sup>1</sup>. Moreover we re-identified a random sample of about 5 percent of the lines with the help of the PHOENIX atmosphere models and found full agreement. Of the identified lines 358 are in the blue arm and 148 are in the red arm of the spectra. In the electronically published Tab. A.2 the central wavelength of the lines as well as the FWHM and the EW can be found.

All spectra besides the brown dwarfs were shifted to rest wavelength before the measurements of the lines. Therefore the main problem was the recognition what is an emission line or emission core. This suffers from the low signal to noise ratio especially in the blue end of the spectra where the count rates are very low. In addition in some wavelength ranges the continuum is not well defined and in these regions it is sometimes

<sup>1</sup> available online under [http://physics.nist.gov/cgi-bin/AtData/main\\_asd](http://physics.nist.gov/cgi-bin/AtData/main_asd)

hard to decide whether a particular feature is an emission line or barely left over continuum between consecutive absorption lines. Since we excluded doubtful features from our line list, the list cannot be claimed to be complete for weaker lines.

We provide some remarks on individual stars:

### A.1. GJ 229A

This is the earliest star in the sample and rather inactive. It shows only Fe I and Fe II emission cores and no pure emission lines at all.

### A.2. AD Leo, YZ Cmi, Prox Cen and LHS 292

The activity level from AD Leo can be compared to YZ CMi, Prox Cen and LHS 292. All three stars exhibit about the same number of Fe I, Fe II and other metal lines, but AD Leo and LHS 292 show very few Ni I emission lines compared to the other two stars. LHS 292 also shows a reduced number of Ti II lines.

### A.3. AT Mic, FN Vir and GL Vir

The reduced number of emission lines in these stars is at least partly due to the much lower S/N ratio compared to AD Leo, YZ Cmi and Prox Cen.

### A.4. UV Cet

UV Cet is a fast rotator with  $v \sin i = 32.5 \text{ km s}^{-1}$  (Mohanty & Basri 2003). Superimposed on the broad emission lines is a set of slightly redshifted, narrow emission lines. We tentatively interpret this as emission from a chromospheric active region (Fuhrmeister et al. 2004).

### A.5. CN Leo

Besides the line list for the averaged spectrum of CN Leo we produced line-lists for a one hour averaged time series on 2002 March, 16th containing a short duration flare and a line list for an one hour averaged time series on 2002 March, 15th showing enhanced emission line flux but no pronounced variability in the light curve. Since the flare was only a short duration flare this line list is showing actually less emission lines than the averaged one, since CN Leo showed less emission lines directly before and after the flare.

**Table A.1.** Basic observations parameters of the observed stars.

name	other name	spectral type	observations	number of identified lines
LHS 1827	GJ 229A	M1	2002-03-15 4 spectra 1200s	11
LHS 5167	AD Leo	M3.5	2002-03-13 3 spectra 1800s 2002-03-16 2 spectra 1200s	142
HD 196982	AT Mic	M4.5	2002-03-16 2 spectra 2400s	91
LHS 1943	YZ CMi	M4.5e	2002-03-13 3 spectra 3600s	178
LHS 2664	FN Vir	M4.5	2002-03-13 3 spectra 3600s	74
LHS 324	GL Vir	M5	2002-03-13 3 spectra 3600s 2002-03-16 2 spectra 2400s	72
LHS 36	CN Leo	M5.5	2002-03-13 6 spectra 7200s 2002-03-14 4 spectra 4800s 2002-03-15 6 spectra 7200s 2002-03-16 6 spectra 7200s 2001-01-06 1 spectrum 3120s	244
LHS 2076	EI Cnc	M5.5	2002-03-15 4 spectra 4800s 2002-03-16 1 spectrum 1200s	80
LHS 49	Prox Cen	M5.5	2001-02-02 1 spectrum 3120s	147
LHS 10	UV Cet	M5.5	2000-12-17 1 spectrum 3120s	109
LHS 248	DX Cnc	M6	2002-03-16 3 spectra 3600s	17
LHS 2034	AZ Cnc	M6	2002-03-14 6 spectra 6000s 2002-03-16 2 spectra 2400s	251
LHS 292		M6.5	2001-02-02 1 spectrum 3120s	103
LHS 429	vB 8	M7	2002-03-13 3 spectra 3600s 2002-03-15 3 spectra 3600s	23
LHS 3003		M7	2002-03-14 3 spectra 3600s	7
LHS 2397a		M8	2002-03-14 3 spectra 3600s	9
LHS 2065		M9	2002-03-13 3 spectra 3600s	7
DENIS-P J104814.7-395606		M9	2002-03-14 4 spectra 4800s	4
DENIS-P J1058.7-1548		L3	2002-03-15 4 spectra 4800s	-
2MASS J1315309-264951		L3	2002-03-15 3 spectra 3600s	4
Kelu-1	CE 298	L3	2002-03-14 3 spectra 3600s 2002-03-16 3 spectra 3600s	2

#### A.6. LHS 2076

The star exhibited a short duration flare during the observations and for the single flare spectrum an additional line list was created. While the number of the Fe I lines remain nearly unchanged during the flare, the number of Ti II lines increases from 2 to 11 and the number of Ni I from 4 to 13 lines revealing temperature changes in the chromosphere during the flare. During the flare the lines are statistically redshifted by an amount of about 0.05 Å.

#### A.7. LHS 2034

The star underwent a long duration flare during the observation. We created an additional line list for the first spectrum taken containing the flare peak. This flare spectrum shows particularly many emission lines in the red part of the spectrum – where the other stars show only very few lines. No line shifts could be found for the flare spectrum. Since the flare decays very slowly the averaged spectrum is affected by the flare spectrum.

#### A.8. LHS 3003, LHS 2397a, LHS 2065, vB-8, DX Cnc and DENIS-P J104814.7-395606

Though the blue part of the spectrum is underexposed for these stars we could identify some emission lines. Moreover DENIS-P J104814.7-395606 showed flaring activity during the observations which led to blueshifts in the spectral lines. This star is discussed in detail by Fuhrmeister & Schmitt (2004).

#### A.9. DENIS-P J1058.7-1548, 2MASS J1315309-264951 and Kelu-1

No radial velocity correction was applied to these very late-type objects, since we had no appropriate template spectrum. Therefore the central wavelength given for these objects is not corrected for radial velocity.

For the L3 dwarf 2MASS J1315309-264951 we report besides the detection of H $\alpha$  and H $\beta$  weak Na I D emission lines (see Fig. A.1). This is to our knowledge the first detection of the Na I D lines in emission in an L dwarf. These are heavily blended with airglow lines known for the UVES instrument (Hanuschik 2003). The EW for H $\alpha$  of 24.1 Å seems to imply that the brown dwarf is in a rather quiescent state since Hall (2002) found EW of 121 Å and of 25 Å half a year later.

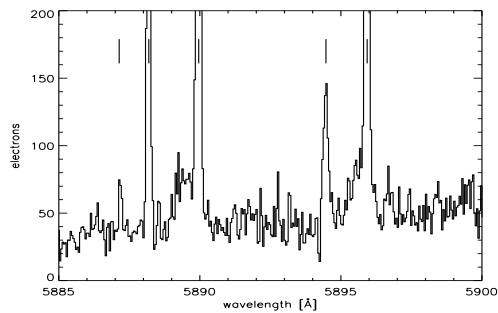


**Fig. A.1.** Spectrum of 2MASS J1315309-264951 around the Na I D lines. Known airglow lines for the UVES instrument are marked with a vertical line.

## References

- Andretta, V., Doyle, J. G., & Byrne, P. B. 1997, *A&A*, 322, 266  
 Avrett, E. H. & Loeser, R. 1984, in *Methods in Radiative Transfer*, 341–379  
 Ayres, T. R. 1979, *ApJ*, 228, 509  
 Ayres, T. R. & Rabin, D. 1996, *ApJ*, 460, 1042  
 Barklem, P. S., Piskunov, N., & O’Mara, B. J. 2000, *A&A*, 363, 1091  
 Carlsson, M. 1986, Uppsala Observatory Internal Report no. 33  
 Carlsson, M. & Stein, R. F. 2002, *ApJ*, 572, 626  
 Cram, L. E. & Mullan, D. J. 1979, *ApJ*, 234, 579  
 Dahn, C. C., Harris, H. C., Vrba, F. J., et al. 2002, *AJ*, 124, 1170  
 Delfosse, X., Forveille, T., Perrier, C., & Mayor, M. 1998, *A&A*, 331, 581  
 Falchi, A. & Mauas, P. J. D. 1998, *A&A*, 336, 281  
 Fuhrmeister, B. & Schmitt, J. H. M. M. 2004, *A&A*, 420, 1079  
 Fuhrmeister, B., Schmitt, J. H. M. M., & Wichmann, R. 2004, *A&A*, 417, 701  
 Gizis, J. E., Monet, D. G., Reid, I. N., et al. 2000, *AJ*, 120, 1085  
 Hall, P. B. 2002, *ApJ*, 580, L77  
 Hauschik, R. W. 2003, *A&A*, 407, 1157  
 Hauschildt, P. H., Allard, F., & Baron, E. 1999, *ApJ*, 512, 377  
 Hawley, S. L. & Fisher, G. H. 1992, *ApJS*, 78, 565  
 Jevremović, D., Doyle, J. G., & Short, C. I. 2000, *A&A*, 358, 575  
 Johns-Krull, C. M. & Valenti, J. A. 1996, *ApJ*, 459, L95+  
 Jones, H. R. A., Longmore, A. J., Allard, F., & Hauschildt, P. H. 1996, *MNRAS*, 280, 77  
 Jordan, C., Ayres, T. R., Brown, A., Linsky, J. L., & Simon, T. 1987, *MNRAS*, 225, 903  
 Kurucz, R. L. & Bell, B. 1995, *Atomic line list* (Kurucz CD-ROM, Cambridge, MA: Smithsonian Astrophysical Observatory, —c1995, April 15, 1995)  
 Leggett, S. K., Golimowski, D. A., Fan, X., et al. 2002, *ApJ*, 564, 452  
 Liebert, J., Kirkpatrick, J. D., Cruz, K. L., et al. 2003, *AJ*, 125, 343  
 Mauas, P. J. D. 2000, *ApJ*, 539, 858  
 Mauas, P. J. D., Andretta, V., Falchi, A., et al. 2005, *ApJ*, 619, 604  
 Mauas, P. J. D. & Falchi, A. 1994, *A&A*, 281, 129  
 Mihalas, D. 1978, *Stellar atmospheres* /2nd edition/ (San Francisco, W. H. Freeman and Co., 1978. 650 p.)  
 Mohanty, S. & Basri, G. 2003, *ApJ*, 583, 451  
 Moore, C. E. 1972, *Nat. Stand. Ref. Data Ser.*, 40  
 Mould, J. R. 1976, *A&A*, 48, 443  
 Saar, S. H. & Linsky, J. L. 1985, *ApJ*, 299, L47  
 Short, C. I., Byrne, P. B., & Panagi, P. M. 1998, *A&A*, 338, 191  
 Short, C. I. & Doyle, J. G. 1997, *A&A*, 326, 287  
 Short, C. I. & Doyle, J. G. 1998, *A&A*, 336, 613  
 Vernazza, J. E., Avrett, E. H., & Loeser, R. 1981, *ApJS*, 45, 635  
 Wedemeyer, S., Freytag, B., Steffen, M., Ludwig, H.-G., & Holweger, H. 2004, *A&A*, 414, 1121  
 Young, P. R., Del Zanna, G., Landi, E., et al. 2003, *ApJS*, 144, 135

## **Chapter 7**

# **Influence of NLTE calculation on the hydrogen lines in chromospheric models**

**B. Fuhrmeister, C. I. Short and P. H. Hauschildt**  
submitted to A&A



## Influence of NLTE calculation on the hydrogen lines in chromospheric models

B. Fuhrmeister<sup>1</sup>, C. I. Short<sup>2</sup> and P. H. Hauschildt<sup>1</sup>

<sup>1</sup> Hamburger Sternwarte, University of Hamburg, Gojenbergsweg 112, D-21029 Hamburg, Germany

<sup>2</sup> St. Mary's University, Halifax, NS B3H 3C3, Canada  
 e-mail: bfuhrmeister@hs.uni-hamburg.de

the date of receipt and acceptance should be inserted later

**Abstract.** We present extensive NLTE calculations for semi-empirical solar 1D chromosphere models. We report on a significant influence of nitrogen, oxygen, and sulfur on the emergent hydrogen emission with respect to LTE vs. NLTE calculations for these elements. This is due to the veil of strong lines of these species in the Ly continuum which is influencing the hydrogen ionisation rate. Moreover, we present a model spectrum with 20 light and iron group elements computed in NLTE. We compare this to an observed solar spectrum and to a photospheric model spectrum.

**Key words.** Line: formation – Sun: chromosphere

### 1. Introduction

The chromosphere is a thin layer in the outer atmosphere of late-type stars. In the classical picture the chromosphere is the place where the temperature of the atmosphere starts to rise outwards steepening in the transition region (TR) until it finally reaches coronal temperatures. This temperature rise induce chromospheric and TR emission which can be used to model the temperature distribution semi-empirically which was done for the Sun by Vernazza et al. (e. g. 1981); Fontenla et al. (e. g. 1990), for other active dwarf stars (e. g. Short & Doyle 1998; Mauas & Falchi 1994), and for red giants (e. g. Harper 1992). This picture of a spatially uniform temperature rise has been challenged by the discovery of CO molecules in the Sun's and other stars' chromospheres (Wiedemann et al. 1994). A more dynamical scenario pictures the chromosphere as a place where heating takes place in acoustic shock waves that are embedded in a cool plasma. However, in both cases the conditions in the chromosphere are more extreme than in the photosphere and therefore NLTE effects gain in importance. Very few extensive NLTE chromospheric studies have been carried out, though. Even for the Sun's photosphere, extensive NLTE line calculations have been carried out only recently (Short & Hauschildt 2005). Fuhrmeister et al. (2005) found for M dwarfs that the NLTE treatment of C, N, O has a significant influence on the amplitude of the hydrogen emission lines. The hydrogen spectrum is important not only as spectral diagnostic, but because the hydrogen ionization balance significantly influences the electron pressure in large parts of the atmosphere. It is also known, that hydrogen pumps certain oxygen lines via

an overlapping transition with Ly $\beta$ . Interactions between Ly $\beta$  and O I were investigated by e. g. Athay & Judge (1995) and Carlsson & Judge (1993). They found that the O I resonance lines at 1302.17, 1304.86 and 1306.03 Å are excited dominantly by fluorescence with the Ly $\beta$  line through the O I triplet at 1025.76 Å (with Ly $\beta$  located at 1025.72 Å). Also there are pumping effects between Ly $\alpha$  and various Fe II, Ca II and H $_2$  lines (McMurry et al. 1999).

The goal of this paper is to further investigate such pumping effects between lines, but more important between the veil of emission lines and the Ly continuum. We compute our models with the general purpose atmosphere code PHOENIX (Hauschildt et al. 1999) which is well suited for this purpose, because it is capable of allowing for millions of atomic and molecular background lines in LTE as well as for multi-level NLTE calculations for many species at the same time. We will investigate the influence of the LTE background lines that have been computed for the first time with high resolution under consideration of the chromospheric and TR temperature rise. Background line opacity was formerly taken into account with 2 Å resolution only in the photosphere by Andretta et al. (1997) or using a harmonic mean in 100 Å intervals for the chromosphere and TR (Short & Doyle 1997). We will take a special interest in the influence of nitrogen, oxygen, and sulfur on the line formation of hydrogen. We also present extensive multi-level NLTE chromospheric calculations on the basis of the VAL C model (Vernazza et al. 1981). Our paper is structured as follows: We describe the assumptions made for the computations in sect. 2 and present the comparison between various different LTE vs. NLTE models in sect. 3. We discuss several aspects of the influence of the NLTE calculations in sect. 4.

Send offprint requests to: B. Fuhrmeister

## 2. Computational method

The models calculated here are 1D chromospheric models with a chromospheric and TR temperature rise attached to the photosphere. All computations are done using the atmosphere code PHOENIX (Hauschildt et al. 1999), which enables us to include extensive multi-level NLTE calculations and the proper treatment of background opacity while holding the temperature vs. column mass distribution fixed. For solving the radiative equilibrium equations in PHOENIX an approximate  $\Lambda$ -operator iteration scheme is applied, which can solve the equations for many species simultaneously (Hauschildt 1993).

One drawback in PHOENIX regarding chromospheric calculations is that presently no partial frequency redistribution (PRD) is included in the code; all calculations are done assuming complete frequency redistribution (CRD). This affects the line shapes and intensities of e. g. Ly  $\alpha$  and Ly  $\beta$  as well as some metal lines like Mg II h and k. While the metal lines should not influence any of our results, the shape of the Ly  $\alpha$  and Ly  $\beta$  line can turn out to be important, since the PRD influences the width of these lines and therefore the overlapping with other lines. Moreover the flux in the Ly  $\alpha$  line may be altered significantly for PRD treatment. The influence of PRD vs. CRD on the Lyman lines has been studied for the Sun by e. g. (Hubeny & Lites 1995). Sim (2001) showed that the influence of PRD ceases for higher surface gravity but was significant for all stars he studied. Since CRD overestimates the line width, we included calculations where the whole Lyman series is treated only with a Gaussian core, which will underestimate the line width.

### 2.1. Atmospheric models

As solar model we used the classical VAL C model (Vernazza et al. 1981). We used the temperature vs. column mass structure with the original turbulent velocity distribution of this model and recomputed the model properties such as  $p_{\text{gas}}$ ,  $p_e$ , and the NLTE departure coefficients self-consistently in PHOENIX. The different models we investigated here are distinguished mainly by the treatment of the atomic background lines, the different sets of species treated in NLTE, the calculation of the Ly series in the CRD or Gaussian approximation, and the spacing of the wavelength grid on which the opacity is computed. These parameters are explained further on. Table 1 gives an overview over the different models used here.

### 2.2. NLTE calculations

All solar models are computed with hydrogen, helium and Ca I - III in NLTE, since hydrogen and helium are the most abundant species in most parts of the considered atmosphere and the Ca II H and K line are important diagnostic lines. Some of the models include in addition other elements calculated in NLTE for different ionization stages. The used data are taken from the Kurucz database (Kurucz & Bell 1995) or from the CHIANTI database (Young et al. 2003) in the case of He I, II, O VI - VIII, N VII, C V, VI, and Ne II - X. These NLTE calculations take into account *all* available levels for each considered ionization stage.

We also computed the VAL C model treating most of the light elements up to Ca as well as the iron group elements in NLTE. In this model 82 different ionization stages and hundred thousands of lines are treated in NLTE. Specifically we have computed in NLTE all ionisation stages of H, He, N, O and Ne, the ionisation stages I and II of Li, Ti, and Mn, the ionisation stages I to III of Ca and Co, the ionisation stages I to IV of C, Na, Mg, Al, Si, K, P, Ni, and Fe, and the ionisation stages I to VI of S. This ensures that the most important species in each layer of the model atmosphere are computed in NLTE with the exception of the high ionisation stages of carbon (see sect. 4).

### 2.3. Background line opacity

Our calculations take into account the veil of atomic background lines throughout the atmosphere, i. e. including the chromospheric and TR temperatures. Our wavelength resolution for these LTE lines regarding the radiative transfer in the models is 2 Å for wavelengths shorter than 30000 Å. NLTE calculations lead to the insertion of additional wavelength points for every NLTE line leading to a non-regularly spaced wavelength grid. We also computed models on a finer wavelength grid with 0.02 Å resolution for the LTE lines shortward of 2000 Å. This will sample especially every LTE line in the Ly continuum. The calculations with the large NLTE set add so many NLTE wavelength points that the mean spacing is 0.01 Å in the Ly continuum with about 15 percent of the spaces larger than 0.02 Å but only 3 percent of the spaces larger than 0.04 Å. These models therefore sample nearly all LTE lines and have to be compared to the models computed on the fine wavelength grid.

### 2.4. Flux contribution functions

As a further diagnostic tool we incorporated the output of a disc integrated intensity contribution function in PHOENIX. The intensity contribution function  $\mathcal{C}_I$  is normally defined on a  $\log \tau_0$  scale, but since our chromospheric models are computed on a column mass scale, we computed also

$$\mathcal{C}_I(\log m) = \mu^{-1} \ln 10 m \kappa S e^{-\tau/\mu}$$

with S being the source function, m the column mass,  $\kappa$  the absorption coefficient,  $\tau$  the optical depth and  $\mu = \cos \theta$  the angle between the considered direction and the normal to the surface. This intensity contribution function is dependent on the considered direction and can be computed for any angle  $\theta$ . Additionally, we calculate the disc integrated value  $\mathcal{C}_F$ . Since we regard only models of the average quiet Sun here the disc integrated value is appropriate. The usage of the flux contribution function instead of the line depression contribution function as introduced by Magain (1986) is a legitimate approximation, since the considered lines are strong.

**Table 1.** Important parameters of the chromospheric models used. Besides the model name it is indicated if LTE background lines are included in the model. The third column indicates which elements are treated in NLTE besides hydrogen, helium and calcium, with 'large' meaning the NLTE set with 82 species as described in sect. 2.2. The fourth column states whether the Ly series is treated in the CRD or the Gauss core approximation. The fifth column indicates whether the opacity shortward of 2000 Å is calculated on the 2 or 0.02 Å wavelength grid.

model name	LTE background	NLTE species	Ly treatment	gridding
NOL	no	-	CRD	2
ATL	yes	-	CRD	2
ATLF	yes	-	CRD	0.02
NOS	yes	N,O,S	CRD	0.02
ANO	yes	N,O	CRD	0.02
OXY	yes	O	CRD	2
OXYF	yes	O	CRD	0.02
OXYL	yes	O	Gauss	2
ATLL	yes	-	Gauss	2
LAR	yes	large	CRD	~0.02
LARN	no	large	CRD	~0.02
LAS	yes	large w/o S	CRD	~0.02
LASN	no	large w/o S	CRD	~0.02
LAF	yes	large w/o secondary lines	CRD	~0.02
LAFN	no	large w/o secondary lines	CRD	~0.02
LAA	yes	large with Ar IV	CRD	~0.02
LAAN	no	large with Ar IV	CRD	~0.02

### 3. Results

#### 3.1. Influence of NLTE calculations

The VAL C model recomputed with PHOENIX with hydrogen, helium and Ca I - III in NLTE and no background lines at all (our NOL model) gave for the H $\alpha$  line very similar results as the original VAL C model and reproduced the observed H $\alpha$  line quite well (see Fig. 1). An inclusion of all available atomic LTE background lines in the model calculations (our ATL model) led to H $\alpha$  in emission, though. We found that this is due to the very strong dependence of the line flux in H $\alpha$  on the treatment of oxygen, nitrogen, and sulfur while the influence of carbon and other elements is less important. To investigate which elements cause this discrepancy we started to switch the elements on one by one for our NOL model, excluding the switched off elements totally from the calculations by turning down their abundance to zero. This shows that the inclusion of nitrogen raises the level of H $\alpha$  line flux significantly, but the major influence is that of oxygen, driving H $\alpha$  into emission. A comparison of two models with zero oxygen abundance versus normal oxygen abundance can be found in Fig. 2. All other elements are treated with their normal abundance. These computations were carried out with the opacity computed on the 2 Å wavelength grid and missed the influence of the sulfur lines totally. If one switches on the elements one by one using the 0.02 Å wavelength grid (our ATLF model) then the influence of sulfur becomes obvious producing emission in the wings of the H $\alpha$  line. In these computations on the fine wavelength grid the largest influence was again that of oxygen, followed by sulfur and nitrogen and some weaker influence of argon.

After having identified oxygen as the main source of interference with hydrogen, we computed a series of NLTE models on the coarse wavelength grid, where we successively included the oxygen ions in the NLTE computations. This shows that the inclusion of only O I in NLTE gives even more flux in the H $\alpha$

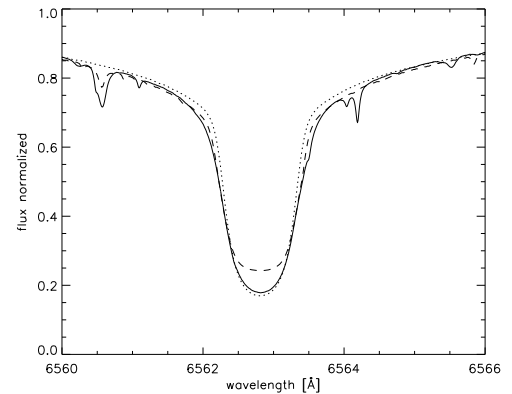


**Fig. 1.** Comparison of observed flux in H $\alpha$  from the Kurucz atlas (Kurucz et al. 1984) with our NOS model (dashed line). In addition we compare it to our NOL model (dotted).

line, while inclusions of progressively more oxygen ions leads to an absorption line when O IV is in NLTE. The inclusion of O V - O VIII leads to only minor changes with the line deepening further. We also computed an additional model including all nitrogen ionization stages in NLTE, which leads to a pronounced absorption line. Nevertheless the line does not reach the depth of the model with no atomic background lines and therefore describes the data less accurate. If one computes the same model with all ionisation stages of oxygen and nitrogen in NLTE on the 0.02 Å wavelength grid (our ANO model), one obtains instead of an pronounced absorption line a line with emission in the wings as can be seen in Fig. 3. Only the inclusion of sulfur in NLTE brings the line back into absorption (our NOS model).

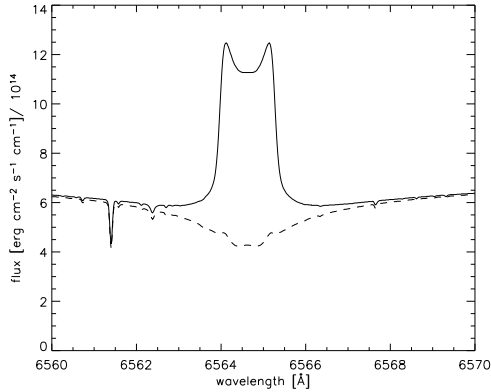


**Fig. 2.**  $H\alpha$  line for our ATL model, one time with normal oxygen abundance (solid line), and one time with the oxygen abundance turned down to zero (dashed line).

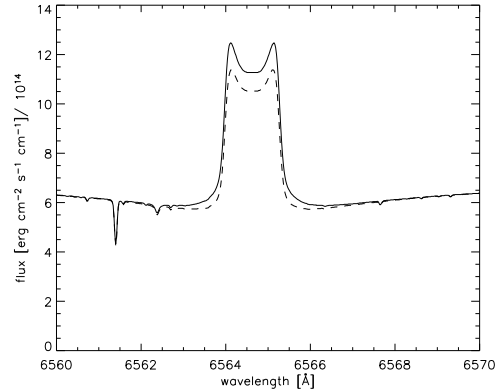


**Fig. 4.** Comparison of the  $H\alpha$  for a treatment of the Ly series in CRD or with a Gaussian core approximation. Our ATL model is the solid line and the ATLL model is the dashed line.

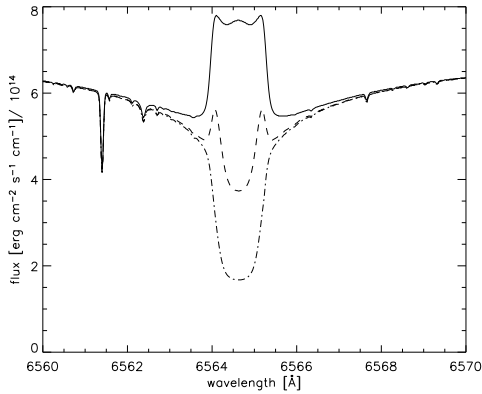


**Fig. 3.** Changes in the  $H\alpha$  line for different NLTE sets. The solid line marks the spectrum for our ATLF model. The dashed line marks the ANO model. The dot-dashed spectrum is our NOS model.

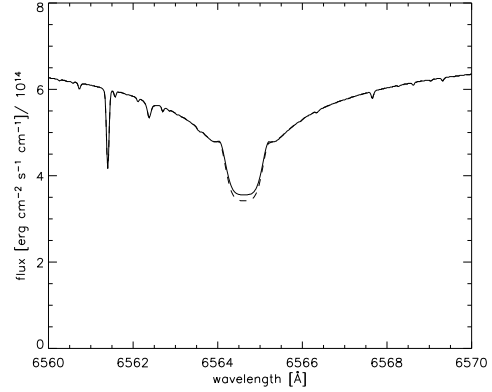


**Fig. 5.** Same as in Fig. 4 but for O I - O VIII calculated in NLTE. The solid line is our OXY model, while the dashed line is our OXYL model.

We investigated also how the treatment of the Lyman series in the CRD approximation does influence the emission behaviour of the  $H\alpha$  line. Since oxygen is the most important perturber, we regard it in these calculations as a representative example. We compare the same calculations with oxygen computed in LTE vs. NLTE and the Lyman series treated as Gaussian cores vs. CRD. It can be seen from Figs. 4 and 5 that the Gaussian core treatment leads to less severe emission for the oxygen LTE case and to only minor changes for all oxygen ions treated in NLTE. Therefore the width of the Lyman lines does influence the other hydrogen lines, but is only a minor effect. This minor effect may be caused by the overlap with strong oxygen lines that get debled in the Gaussian core treatment. Since the overlap between the  $Ly\beta$  line and the O I line is not debled by a Gaussian core approximation this cannot be responsible for the differences. Instead we identified

two strong O IV lines and one O I in the vicinity of the  $Ly\alpha$  line that become debled by a Gaussian core treatment. These lines are located at 1213.20 Å and 1217.72 Å in case of O IV and at 1217.65 Å in case of O I. We also checked that the lowering of the oxygen abundance to the value of 8.66 found by Asplund et al. (2004) has only a minor influence on the predicted strength and shape of the  $H\alpha$  line.

### 3.2. Comparison to solar data

We compared our LAR and LARN models to the NLTE photospheric model of Short & Hauschildt (2005) and to solar data from Kurucz et al. (1984). We rescaled the observed irradiance by  $d^2/R^2$  to compare it to our model fluxes. Redwards of 7000 Å the photospheric model flux has to be increased by about four percent to match the data and the chromospheric model for about seven percent. This lower flux in the IR for the chro-

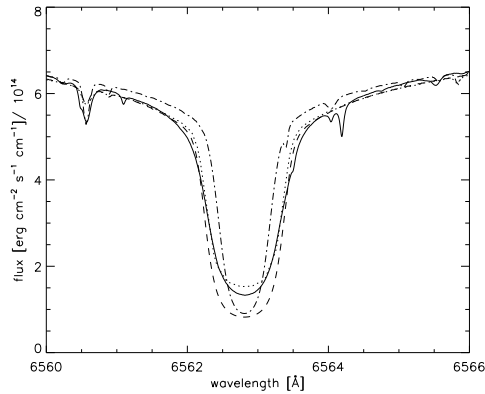


**Fig. 6.** Comparison of solar data (solid line) to the photospheric model from Short & Hauschildt (2005) (dot-dashed) and to our LAR model (dotted) and our LARN model (dashed) for the  $H\alpha$  line.

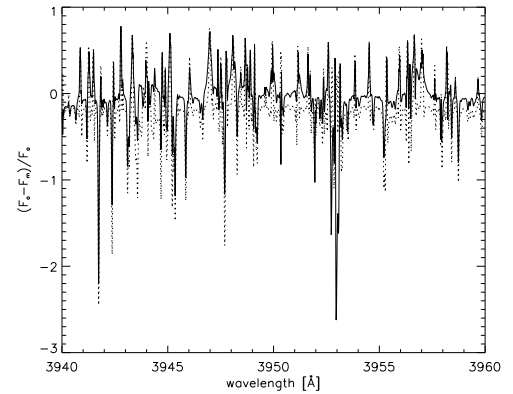


**Fig. 7.** Relative difference between the observed Flux ( $F_o$ ) and the model flux ( $F_m$ ) as a percentage of  $F_o$  for a wavelength range between the Ca II H and K lines. The solid line denotes our LAR model, while the dotted line denotes the photospheric model from Short & Hauschildt (2005). It can be seen that the photospheric model in average is about 10 percent too strong.

mospheric models is due to a slightly reduced luminosity since these models were calculated with  $\log g=4.5$ . For the  $H\alpha$  line the comparison between models and data can be found in Fig. 6. Both models are scaled according to their IR additional offset. Our LAR model is in good agreement with the data, though it produces slightly too much flux in the  $H\alpha$  line, while the chromospheric model not including the LTE background lines produces not enough flux. However, the inclusion of additional NLTE species besides oxygen, nitrogen and sulfur causes only minor changes in the  $H\alpha$ , as can be seen by a comparison of Fig. 6 and 1 for the case of LTE background lines included. Note, that the chromospheric models provide a better fit of the width of the  $H\alpha$  line, since additional broadening by microturbulence is included in these models.

Another wavelength range, where the chromospheric models give a significant better overall fit, is the region around the Ca II H and K line (see Fig. 7). While the photospheric model do not provide a good fit for the wavelength region between the Ca II H and K line without degrading the model for about 10 percent, our LAR model does without rescaling.

As another representative example of chromospheric influence, we present a wavelength range around  $H_9$  at  $3835.39 \text{ \AA}$ . It includes further a strong Fe I line at  $3834.23 \text{ \AA}$  and a Mg I line at  $3832.31 \text{ \AA}$ . The comparison can be found in Fig. 8. We plotted only our LAR model, since our LARN model without LTE background lines is very similar, but again weaker in the  $H_9$  line as well as in the Fe and Mg lines. Note that the photospheric model had to be decreased by about 20 percent to match the wings of the strong lines with the data. On the other hand the chromospheric model was increased by about 10 percent. The chromospheric model is significantly weaker than the photospheric model in the wavelength range between 2000 and 5000  $\text{\AA}$ . Many of the weak absorption lines that have been modeled quite well by the photospheric model have vanished in the chromospheric model since they are filled in by chromospheric emission due to LTE treatment and broadened by the applied turbulent velocity.

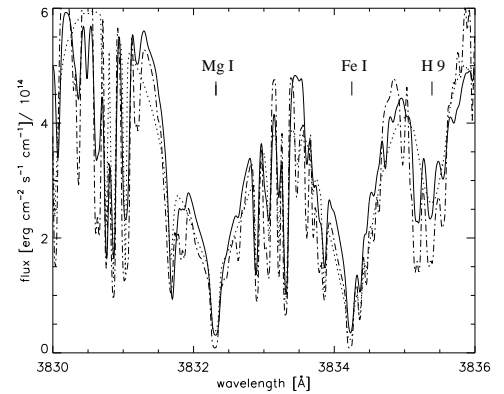


**Fig. 8.** Same as in Fig. 6 but for a wavelength range in the very blue part of the optical range, where the chromosphere also influences the continuum.

## 4. Discussion

### 4.1. Influence on hydrogen

We regard line pumping mechanisms between strong oxygen lines and  $Ly\alpha$  and  $Ly\beta$  as a minor effect in the influence on the hydrogen spectrum. Also the treatment of the Lyman series in CRD approximation does not influence our results in a fundamental way. Instead we regard the veil of strong oxygen, nitrogen and sulfur lines in the Ly continuum as the most important influence. If the level populations of these strong transitions are calculated in LTE the source function of these lines must follow the Planck function. NLTE calculations show that the source function is totally overpredicted by this treatment and so is the line flux. This additional flux leads to more photoion-

isation events of hydrogen and therefore to a higher electron pressure. This in turn leads to a significant contribution of the Planck function to the source function of the hydrogen lines (see also next section for discussion of the radiative transfer).

Using NIST (available under [http://physics.nist.gov/cgi-bin/AtData/lines\\_form](http://physics.nist.gov/cgi-bin/AtData/lines_form)) we found that O IV alone has 112 lines in the Ly continuum (710 to 910 Å) with  $A_{ij}$  larger than  $1 \cdot 10^8 \text{s}^{-1}$ . All oxygen ions together have 189 of these very strong transitions, while nitrogen has 110 and sulfur has 21. The carbon ionization stages also have 43 of these very strong lines, but redwards of 800 Å they are almost all due to C II. It turns out that these low ionisation stages that are found in the chromosphere have less influence on the hydrogen ionisation balance than the higher ionisation stages like O IV and S V. Since the densities in the chromosphere are much higher than in the TR, the photons of these species cannot reach the higher chromosphere, where the hydrogen lines are formed, while the photons of the TR species can. Other elements like iron have no influence, since e. g. non-coronal iron ionisation stages have no transitions in the Lyman continuum at all.

To show the direct influence of the line flux in LTE vs. NLTE calculations with the opacity computed on the fine wavelength grid, we investigated the radiative absorption rates of the ground level of hydrogen to the ionization state and found that in the TR and high chromosphere they are a factor of 10 higher for oxygen and nitrogen calculated in LTE than for oxygen and nitrogen in NLTE. Therefore these lines pump the hydrogen ionization unrealistically, if they are calculated in LTE. This unrealistic high ionization of hydrogen should lead to an increase of the electron pressure which is indeed about 10 percent higher for the LTE model. The unrealistic high electron pressure then drives the H $\alpha$  line into emission.

Since carbon is a highly abundant species we originally tried to include all ionisation stages in our NLTE calculations, but it turned out, that models that include C VI are not converging but varying randomly from iteration to iteration. This destabilization of the model is due to the coarse temperature sampling in the outermost layers of the model where C VI is very abundant only in the second outermost layer. The partial pressures undergo an increase of seven magnitudes for this layer. We conclude that for a proper NLTE treatment of C VI a finer temperature spacing in the TR is needed, which would guarantee that there are no jumps in the partial pressures. Since C V has no impact on the H $\alpha$  line we decided to compute the large NLTE set only with C I to IV.

#### 4.2. Models with large NLTE sets

Even for the set with 82 NLTE species the two models with and without inclusion of the LTE background lines (LAR/LARN) are not identical at all in strong chromospheric lines, though the difference ceases with increasingly larger NLTE sets. Therefore there must be still background lines being present which disturb the hydrogen ionisation balance. Since we found in the LTE calculations that also argon has an influence on the hydrogen lines, argon should be treated in NLTE, but unfortunately there is a lack of atomic data for argon among both the Kurucz

and CHIANTI data. For the lower ionisation stages of argon only Ar IV is found in the CHIANTI database. For the additional computation of Ar IV in NLTE the difference between our LAA and LAAN model is about 30 percent in the H $\alpha$  line. For our LAR and LARN model the difference is about 80 percent in the H $\alpha$  line. Since there are also strong Ar III lines found in the Ly continuum in our models, an inclusion of Ar III should improve the situation even more.

Moreover there are even for our LAR model still many of strong emission lines occurring in the Lyman continuum for the inclusion of LTE background lines. Qualitative comparison to SUMER spectra of a quiet region near disc center (Curd et al. 2001) shows that this is totally unrealistic. Our NLTE calculations sampled most of the strong observed lines in this wavelength region and therefore the treatment without LTE background lines gives the more realistic description of this region. For wavelength redwards of Ly $\alpha$  the differences between the LAR and the LARN model spectrum ceases, though.

PHOENIX treats very weak lines of species computed in NLTE, nevertheless, in LTE. For a detailed description, how these secondary lines are treated see Hauschildt & Baron (1995). Though the secondary lines are not expected to alter our results, since they are weak lines, we checked their influence. A comparison of our models LAF and LAR and our models LAFN and LARN showed no significant differences for the H $\alpha$  or Ly $\alpha$  line or the Ly continuum besides in single metal lines.

To show the influence of the LTE treatment of certain species on properties of the radiative transfer we calculated the flux contribution function for a model identical to our large NLTE set but without S IV to VI. The spectrum of this LAS model looks similar to the model with only oxygen and nitrogen as additional NLTE species (as seen in Fig. 3) and is not shown here. In Figs. 9 and 10 we show the monochromatic source function  $S_\nu$ , the Planck function  $B_\nu$ , the intensity  $J_\nu$ , and the flux contribution function  $C_F$  for our LAS and LASN models. Here  $S_\nu$  is the total source function, i. e.  $S_\nu$  is the ratio of the continuous plus line emission coefficient and the continuous plus line absorption coefficient. Both  $S_\nu$  and  $C_F$  change dramatically. In the case without background line blanketing (our LASN model)  $S_\nu$  follows  $J_\nu$  and is only increased by the contribution of  $B_\nu$  for layers in the transition region - which is above the peak of  $C_F$ . This explains why H $\alpha$  in this case is nearly identical to the photospheric model. In the case with LTE line opacity (our LAS model), however,  $C_F$  peaks not only in slightly deeper layers of the atmosphere, but also has  $S_\nu$  a contribution from  $B_\nu$  in these layers. The H $\alpha$  appears only slightly in absorption in the core and with emission in the wings.

From this example of the H $\alpha$  line it can be seen that treating many background lines in LTE causes an unrealistic coupling between  $S_\nu$  and  $B_\nu$ . Therefore,  $S_\nu$  is too large in the outer atmosphere with the result that the H $\alpha$  line is too strong in emission. To prevent the LTE lines from being over-thermalized, one can turn them artificially into scattering lines. This can be done in PHOENIX by choosing the parameter  $\varepsilon$  in the relation  $S = \varepsilon B + (1 - \varepsilon)J$ . Fuhrmeister et al. (2004) used  $\varepsilon = 0.1$  to achieve better agreement in the Balmer lines for M dwarf models. This treatment of the LTE lines applies to the whole atmo-

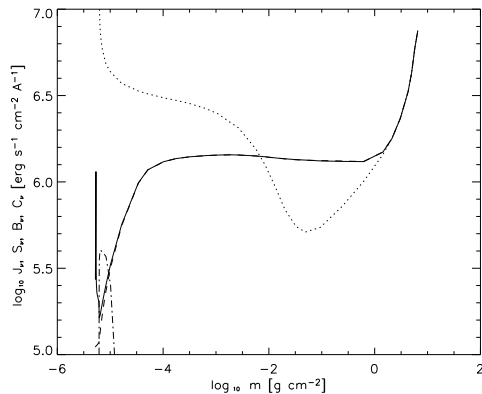


**Fig. 9.** Various radiative transfer quantities for the central wavelength of  $H\alpha$  for our LASN model. The solid line is  $S_n$ , the dotted line is  $B_n$ , the dashed line is  $J_n$ , and the dash-dotted line the scaled  $C_F$ .

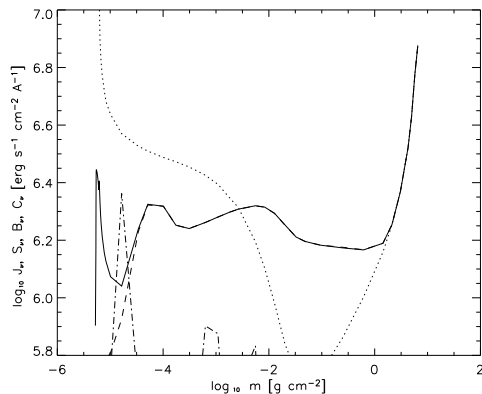


**Fig. 10.** Same as in Fig. 9 but for our LAS model. Compared to Fig. 9 the peak of the contribution function moved to deeper layers in the atmosphere.

sphere, though, and results therefore in an unrealistic treatment of the photospheric part.

## 5. Conclusions

Using the VAL model as an example of a classical 1D chromospheric model we found that the inclusion of LTE background lines does not lead necessarily to better i. e. more realistic results. The LTE emission lines are always overpredicted in strength in chromospheric models, which can lead to unrealistic high pumping effects between LTE lines and the hydrogen ionisation rate and therefore gives a wrong hydrogen ionisation balance. These pumping effects are very sensitive to the number of LTE lines sampled in the Lyman continuum. Therefore the wavelength grid on which the LTE background opacity is computed can influence the outcome of the simulations. Sampling of  $0.02 \text{ \AA}$  in this region showed that oxygen,

nitrogen and sulfur have the most important influence on the hydrogen lines, while argon shows some minor influence.

Moreover, our calculations of the model with 82 species computed in NLTE showed that the hydrogen spectra including LTE background opacity is still not identical to the same model without LTE background lines. While the model including the LTE lines opacity produces too much flux in  $H\alpha$  compared to solar data, the same model without LTE line opacity produces not enough flux in  $H\alpha$ . Therefore the inclusion of a large NLTE set would suggest a model with a stronger chromosphere than the VAL model in case of no LTE background lines vs. a weaker chromosphere for inclusion of LTE background lines. For additional treatment of  $\text{Ar IV}$  in NLTE the difference between models with LTE background lines and without ceases. Unfortunately we are not able to include other ionisation stages of argon in the NLTE calculations due to a lack of atomic data and hence the question, if an inclusion of argon in the NLTE calculations would remove the differences remains unsettled at the moment. The changes in the hydrogen spectrum due to different NLTE sets are rather small for no inclusion of LTE background lines, though. The difference between the NOL and the LAAN model are less than 50 percent in the  $H\alpha$  line. Therefore we conclude that it is better not to include LTE background lines in any chromospheric model, especially not if only small NLTE sets are used.

In general our calculations show the high impact of TR lines on the hydrogen emission lines for solar 1D chromospheric models and stress the necessity of a NLTE treatment especially for oxygen, nitrogen and sulfur lines. This impact of the highly ionized species – present only in the TR – has not been accounted for in previous chromospheric models. It clearly shows the need for a more realistic inclusion of the transition region in chromospheric models.

*Acknowledgements.* The model computations were performed at the Norddeutscher Verbund für Hoch- und Höchstleistungsrechnen (HLRN), at the Hamburger Sternwarte Apple G5 cluster financially supported by HBFfG and at St. Mary's University, Halifax, Canada. B. Fuhrmeister acknowledges financial support by the Deutsche Forschungsgemeinschaft under DFG SCHM 1032/16-1 and from Deutscher Akademischer Austauschdienst (DAAD).

## References

- Andretta, V., Doyle, J. G., & Byrne, P. B. 1997, *A&A*, 322, 266
- Asplund, M., Grevesse, N., Sauval, A. J., Allende Prieto, C., & Kiselman, D. 2004, *A&A*, 417, 751
- Athay, R. G. & Judge, P. G. 1995, *ApJ*, 438, 491
- Carlsson, M. & Judge, P. G. 1993, *ApJ*, 402, 344
- Curdt, W., Brekke, P., Feldman, U., et al. 2001, *A&A*, 375, 591
- Fontenla, J. M., Avrett, E. H., & Loeser, R. 1990, *ApJ*, 355, 700
- Fuhrmeister, B., Schmitt, J. H. M. M., & Hauschildt, P. H. 2005, *A&A*
- Fuhrmeister, B., Schmitt, J. H. M. M., & Wichmann, R. 2004, *A&A*, 417, 701
- Harper, G. M. 1992, *MNRAS*, 256, 37
- Hauschildt, P. H. 1993, *JQSRT*, 50, 301
- Hauschildt, P. H., Allard, F., & Baron, E. 1999, *ApJ*, 512, 377

- Hauschildt, P. H. & Baron, E. 1995, *JQSRT*, 54, 987
- Hubeny, I. & Lites, B. W. 1995, *ApJ*, 455, 376
- Kurucz, R. L. & Bell, B. 1995, Atomic line list (Kurucz CD-ROM, Cambridge, MA: Smithsonian Astrophysical Observatory, —c1995, April 15, 1995)
- Kurucz, R. L., Furenlid, I., & Brault, J. T. L. 1984, Solar flux atlas from 296 to 1300 nm (National Solar Observatory Atlas, Sunspot, New Mexico: National Solar Observatory, 1984)
- Magain, P. 1986, *A&A*, 163, 135
- Mauas, P. J. D. & Falchi, A. 1994, *A&A*, 281, 129
- McMurry, A. D., Jordan, C., & Carpenter, K. G. 1999, *MNRAS*, 302, 48
- Short, C. I. & Doyle, J. G. 1997, *A&A*, 326, 287
- Short, C. I. & Doyle, J. G. 1998, *A&A*, 336, 613
- Short, C. I. & Hauschildt, P. H. 2005, *ApJ*, 618, 926
- Sim, S. A. 2001, *MNRAS*, 326, 821
- Vernazza, J. E., Avrett, E. H., & Loeser, R. 1981, *ApJS*, 45, 635
- Wiedemann, G., Ayres, T. R., Jennings, D. E., & Saar, S. H. 1994, *ApJ*, 423, 806
- Young, P. R., Del Zanna, G., Landi, E., et al. 2003, *ApJS*, 144, 135

# Chapter 8

## Summary and outlook

### 8.1 Summary

In this thesis the activity of 24 mid to late-type stars was investigated. Using high resolution echelle spectra taken with the UVES spectrograph different aspects of activity have been examined. Two main aspects were (i) coronal activity and (ii) chromospheric activity.

#### Coronal activity (i) :

A search for forbidden coronal lines in the optical was carried out in the subsample which contains the dwarfs earlier than M7. In these 15 stars the main focus was on the search for the Fe XIII forbidden coronal line at 3388.1 Å. Specifically, the results can be summarised as follows:

1. In two cases the Fe XIII line was clearly detected: During a short duration flare on LHS 2076, and in the data of for CN Leo, where the line has been discovered before (Schmitt & Wichmann 2001). Two more stars, namely GL Vir and UV Cet, show ambiguous line profiles that may indicate some Fe XIII flux in these stars.
2. For CN Leo a spectral time series reveals a high variability in the strength of the Fe XIII line even on the timescale of hours with no major flare activity associated. This indicates a microflare heating for the quiescent emission of CN Leo. The line was shifted bluewards during a short duration flare, indicating outward mass motions.
3. For CN Leo neither the Ca XII line at 3327 Å nor the Fe XIV line at 5303 Å could be detected. Also another survey for the Fe XIII line in eight active M dwarfs carried out by Wallerstein & Tyagi (2004) resulted in no further detections. This discouraging result

may find its explanation in the coronal temperature structure of very active M dwarfs, that differ significantly from the Sun and peak at much higher temperatures around  $\log T = 7$  (Sanz-Forcada et al. 2003; Robrade & Schmitt 2005).

#### Chromospheric activity (ii) :

Since most of the chromospheric emission lines in the blue spectral range of M dwarfs had not been identified so far, an identification campaign was initiated with the following results:

1. Measurements of the equivalent width as well as central wavelength and FWHM has been carried out for more than 500 emission lines, many of which are found throughout the whole sample.
2. First detection of the Na D lines in emission for an L3 dwarf, i. e. 2MASSI J1315309-264951.

Several spectra exhibit variations in their emission lines. Besides a short duration flare on CN Leo and LHS 2076 and some other smaller events, two major flare events have been recorded in the time series spectra and have been analysed:

1. Detection of a huge flare on the old M9 dwarf DENIS 104814.7-395606.1, which led to line shifts for  $H\alpha$ ,  $H\beta$  and the Na D lines. Additional brightening on the blue side for the  $H\alpha$  and the  $H\beta$  line was observed in the last spectrum in the time series indicating velocities of about  $100 \text{ km s}^{-1}$ . This may be interpreted as a rising cloud. Since DENIS 104814.7-395606.1 exhibits at least temporally strong chromospheric activity, it is another example of chromospheric activity directly at the hydrogen burning border.

2. For LHS 2034 pronounced asymmetries have been found during the decay phase of a long duration flare. All Balmer lines and the strong He I lines exhibit enhancement of the *red* side of the line wings, while the metal lines do not. This can be interpreted with the help of PHOENIX chromospheric flare models, that predict a line formation depth in the lower and middle chromosphere for the metal lines, but a formation depth in the upper chromosphere for the hydrogen and helium lines. The line asymmetry itself is interpreted as a series of downflows similar to chromospheric downward condensations known from the Sun.
3. Similar but much weaker line asymmetries during apparently quiescent state have also been found for LHS 2397a. Since the velocity shift in the asymmetries is about the same value as the rotational velocity, an interpretation as a flickering in an active region rotating out of sight is more suggestive than downflows like for LHS 2034.

For further interpretation of the data, the stellar atmosphere code PHOENIX has been used to compute classical one-dimensional chromospheric models. The following results have been obtained:

1. For the stars AD Leo, YZ Cmi, CN Leo, DX Cnc and LHS 3003 semi-empirical chromospheric models have been built using various metal lines besides the Balmer line series.
2. Since the very late-type star LHS 3003 could in principle be described with the same type of temperature distribution as AD Leo, it is suggestive that the heating mechanisms for the chromosphere are the same down to at least M7.
3. LTE treatment of transitions in chromospheric models is not appropriate and can disturb the whole ionisation balance. This is caused mainly by transitions of oxygen, nitrogen and sulfur, which are located in the Lyman continuum.

## 8.2 Outlook

As an essential part of this thesis, chromospheric models with the stellar atmosphere code

PHOENIX have been developed. These models help to better understand the complicated processes in the chromosphere and to interpret spectral data. The here presented models can be improved in several ways.

### Coronal influence

The chromosphere is a layer embedded between the photosphere and the corona. Up to now only the photosphere is part of the chromospheric models. The influence of the corona on the chromosphere should take place exclusively through the downward propagating radiation, since the coronal density is so low. A treatment of the coronal gas with PHOENIX is not necessary, since the coronal approximation holds and is much easier to compute. Therefore, a simple coronal model could treat the back-warming of the corona as an infalling irradiation, if the spectral distribution of the coronal radiation is known. Such spectral distributions of the coronal radiation can be gained from X-ray observations or from coronal models. Since it is already clear that NLTE effects play a major role in the chromosphere, an influence of the X-ray and XUV radiation that can penetrate deep into the transition region and chromosphere is expected.

### Influence of dust

For the very cool dwarfs at the hydrogen burning limit dust in their atmosphere may play an important role. Since it is an efficient scatterer and warms the photospheric layers it influences the electron pressure in important regions of the atmosphere. This issue was only very briefly addressed in this work, since the treated objects are at the border, where dust is becoming important. For an extension of chromospheric models to even cooler dwarfs an extensive analysis of the influence of dust will be mandatory.

### Metallicity

For some of the strong metal lines and especially iron lines it turned out that even the absorption part of the line is not modelled correctly. This discrepancy may be caused by an incorrect microturbulent pressure in the line forming region. Since the microturbulent velocity is fixed to half the value of the sound velocity, a detailed analysis of its influence in different layers should be carried out. Another possibility for the disturbance of the strong metal

lines is a metallicity different from the solar metallicity, which was applied here.

### Models for giants

Since PHOENIX is capable of computing stellar atmospheres throughout the Hertzsprung-Russel diagram it is a straightforward approach to extend the chromospheric modelling to other types of stars. A very interesting group of stars for chromospheric modelling are giants. Giants are known to have either cool dense winds or transition regions and coronae besides very few so called hybrid stars that exhibit both. Classical semi-empirical modelling of these stars has been done for giants for example by Harper (1992). Unfortunately an extension of the chromospheric models presented here to this type of star is not as straightforward as it may seem. Especially a more correct treatment of scattering is needed, due to the very low densities in the atmospheres of giants, i. e. for chromospheres of giants partial frequency redistribution becomes extremely important (see also next point).

### Partial frequency redistribution

Normally the numerical treatment of scattering is realised by using either the assumption of coherent scattering or complete frequency redistribution over the line profile, with the latter being used in PHOENIX. Neither of these limiting cases is usually found in stellar atmospheres. Due to the high densities found in stellar photospheres the atom will be perturbed by collisions during the scattering process making complete redistribution (CRD) a good approximation. However, this approximation is not valid any more in the lower densities of stellar chromospheres and transition regions. This is especially true for the low gravity environment in chromospheres of giant stars, but also in dwarf stars - which was shown by e. g. Sim (2001). To account for the coherent scattering in the wings of the affected lines they have to be computed using partial frequency redistribution (PRD). Affected lines are normally  $Ly\alpha$ ,  $Ly\beta$  (which also can exhibit cross redistribution with  $H\alpha$ ), Ca II H and K lines, and Mg II lines. Since all these lines are often used for temperature diagnostics their line profile synthesis should be treated with care. Moreover the PRD treatment can affect the flux in the  $Ly\alpha$  line which in turn can influence the whole atmospheric structure via the ionisation balance. Therefore the inclusion of the PRD treatment in PHOENIX will be a

crucial step for more realistic chromospheric models. A robust and rapidly converging approximate iteration scheme for PRD was developed for example by Hubeny & Lites (1995) or Gayley (2002).

### Three dimensional models

All the previously mentioned extensions to this thesis can be realised for one-dimensional, classical semi-empirical models computed with PHOENIX. Since PHOENIX is in the process of becoming capable of computing three-dimensional radiative transfer, another very interesting approach is to recalculate existing hydrodynamic chromospheric calculations. Such calculations exist for example for the Sun, but are computed only with grey opacities and therefore do not produce model spectra. PHOENIX could recalculate the radiative transfer for such hydrodynamic models under much more realistic assumptions and compute model spectra, which then can be compared to data. This is especially important, even for the Sun, since the theory that the non-magnetic chromosphere is heated by acoustic waves has been challenged recently (Fossum & Carlsson 2005). On the other hand, three dimensional radiative transfer calculations with at least hydrogen in NLTE are clearly a challenge to present supercomputers, both in memory capacity and computing time.

## References

- Fossum, A. & Carlsson, M. 2005, *Nature*, 435, 919
- Gayley, K. G. 2002, *ApJ*, 565, 545
- Harper, G. M. 1992, *MNRAS*, 256, 37
- Hubeny, I. & Lites, B. W. 1995, *ApJ*, 455, 376
- Robrade, J. & Schmitt, J. H. M. M. 2005, *A&A*, 435, 1073
- Sanz-Forcada, J., Brickhouse, N. S., & Dupree, A. K. 2003, *ApJS*, 145, 147
- Schmitt, J. H. M. M. & Wichmann, R. 2001, *Nature*, 412, 508
- Sim, S. A. 2001, *MNRAS*, 326, 821
- Wallerstein, G. & Tyagi, S. 2004, *PASP*, 116, 554



## Appendix A

# How to compute a PHOENIX chromosphere

The stellar atmosphere model code PHOENIX incorporates the possibility to compute semi-empirical chromospheres, i.e. an arbitrary temperature rise can be attached to an existing atmospheric structure. This chapter is neither thought to be a general introduction to the use of PHOENIX, nor as a replacement of the PHOENIX manual. It is intended to help to avoid certain known problems in computing chromospheres. Moreover the following text will give a short introduction to the use of the chromospheric mode of PHOENIX. This mode is still experimental and therefore the user has to check for certain inconsistencies or hardcode certain parameters. This will be mentioned in the following text as well. Some of such more specific comments may become obsolete in the future. The actual `phoenix.f` version to which most of the comments refer is 13.08.05A and the `make_chromos.f` version is `make_chromos_vers12.f`.

Besides an executable of `phoenix` an executable of `make_chromos` is needed. The procedure `make_chromos.f` presents an example for an input file, which must be named *chromos.dat*. The scheduler script (dqs file) used for `phoenix` also contains some namelist parameters regarding chromospheres. In the following, PHOENIX input parameters will be printed in *italic*, while the names of procedures and executables will be printed in `typewriter style`.

The general procedure is, to first compute a photospheric model in thermal equilibrium. In a second step, `make_chromos` is used to attach an arbitrary chromospheric temperature rise. Third, `phoenix` is used to recompute the properties of the combined photospheric and chromospheric model.

### A.1 Starting with a photosphere

A converged photospheric model atmosphere in thermal equilibrium is used as a starting point for computing chromospheres. It is extremely important that the photosphere fits the star well, since the underlying photosphere influences the emerging spectrum of the combined photospheric and chromospheric model. When fitting model chromospheres to a stars spectrum, even an alteration of  $T_{eff}$  of about 200 K will alter the best fitting chromosphere. To explain a certain amplitude in the emission lines the usage of a lower effective temperature in the photospheric model will lead to a weaker chromosphere, while the usage of a higher effective temperature would favour a stronger chromosphere. A stronger chromosphere implies that it is located deeper in the stars atmosphere, i.e. has a temperature minimum and onset of the transition region at higher pressure. To find the best fitting photospheric model use only the red part (from about 4500 Å) of the stars spectrum for the fitting process, since any blue part may be chromospherically influenced.

Moreover  $\log g$  and the metallicity will have an influence on the best fitting chromospheric model. So far only solar photospheric metallicity has been used. For very cool stars there will also be an influence of dust. One should also keep in mind that uniform abundancies in the whole atmosphere may be not too realistic, however, up to now PHOENIX can handle only the same abundancies for every layer. For the Sun it was found that the abundance of certain elementes differ with height. This is the so called FIP-effect (First Ionisation Potential), where elements with low first ionisation potential are predominantly carried to coronal heights due to their increased coupling to the magnetic field. In other stars also an inverse FIP-effect is observed.

On the other hand, the mass in the stellar model does not play an important role. For M dwarfs a usage of 0.5 or 0.1 solar masses does not lead to significant changes in the emission lines.

Since the model will cover the chromosphere and part of the transition region (TR) and thus outer parts of the star's atmosphere, the underlying photospheric model should cover this part of the atmosphere - which is normally not the case. Therefore the outer optical standard depth parameter has to be altered. This is done via the parameter *tapp* and *tminlg* in the namelist of the scheduler script (dqs file). Try *tapp*=1d-12, *tminlg*=-12.0 for M dwarfs or *tapp*=1d-10, *tminlg*=-10.0. for solar like stars.

## A.2 Attaching the chromospheric temperature rise

The chromospheric temperature rise is attached by the program `make_chromos.f` which is part of the PHOENIX package. The normal version of `make_chromos.f` will create a linear temperature rise vs. column mass in the chromosphere and a linear temperature rise vs. log column mass in the transition region. The column mass is defined as  $\int \rho ds$ , where  $\rho$  is the density and  $s$  is the distance increasing inwards. `make_chromos.f` is also capable of only computing the column mass grid for a photosphere. Use the parameter *only\_cm* to activate this function. The column mass is normally not given in the .20 file for a photospheric model (the .20 file contains the atmospheric structure). Computing the column mass for a photospheric model is useful to compare atmospheric parameters like electron density for a truly photospheric and a chromospheric model. There also exists a version of `make_chromos.f` that will create two linear segments in the chromospheric part (useful for plateaus). An example of an input file to `make_chromos.f` is found at the end of the program. In the following the more important parameters will be discussed.

Since PHOENIX photospheres are usually computed with 50 depth layers and for chromospheric atmospheres at least 100 depth points are desirable, there is a switch that tells the program to use a 50 layer input photosphere and create as output a 100 layer atmosphere. If `make_chromos.f` is used in this way it must be compiled using a PHOENIX version with 50 layers. After that PHOENIX can be compiled again with 100 layers to compute the actual models. The script `mk100`

will alter the complete code from 50 to 100 layers. In this mode `make_chromos` must also be told how many additional layers should be put into the chromosphere and how many into the transition region (it will check for the sum being 100). The transition region should be sampled not too coarsely in temperature especially up to 20 000 K, since He is formed in that temperature region.

Besides the linear temperature rise the program will create a linear rise of the turbulent velocity throughout the chromosphere. This part will be overwritten, if in the model iteration the parameter *chvtb\_fac* is used, which will give a rise of the turbulent velocity treated as a fixed fraction of the sound velocity. Since the linear rise of the turbulent velocity can lead to larger values than the sound velocity in single layers the use of *chvtb\_fac* is strongly recommended. Otherwise the atmosphere may not converge but stop with an error while solving the hydrostatic equations. If the turbulent velocity exceeds the sound velocity a typical error will be *pgas* lower zero.

The strength of the emergent emission lines is controlled mainly by the position of the onset of the transition region. Transition region at higher column mass (corresponding to higher pressure) will lead to larger amplitudes in the emission lines. Also, a higher temperature of the top of the transition region will usually give a more active model due to the backwarming. A value of *tmax\_top*=100 000 K is recommended. Typical values of the onset of the transition region for M dwarfs during quiescent state are about  $10^{-5}$  to  $10^{-7}$  in column mass. It is important that the *lm\_top* value is in agreement with the chosen *pout* i.e. check if  $\log g - \log pout = lm\_top$ , where *pout* is the outer pressure of the atmosphere. This problem arises, since the outer layer in the model is defined by *pout* as well as by the given *lm\_top*. *lm\_top* is needed to define the column mass grid, but *pout* is traditionally used to define the outer layer for `phoenix`. For future versions of `make_chromos` *lm\_top* should be computed to avoid this possible source of error. Also one has to check carefully, that the *pout* chosen for the construction of the chromosphere is the same as in the namelist of the dqs file for the main iterations with `phoenix`. At the moment `phoenix` does not check the consistency of *pout* in the .20 file created by `make_chromos` and *pout* in the namelist for the main iterations. This will be included in a future version of `phoenix`.

### A.3 Model iteration

There are two different chromospheric modes incorporated in PHOENIX. Use *ichrom=t* or *ichrom2=t*. Only *ichrom2=t* will be described here. The main alterations in the model computations are in the hydrostatic solver, line selection is done for regularly spaced depth points and temperature correction is switched off.

There are some parameters especially interesting for chromospheric model calculations:

- *chvtb\_fac* (see also above) will fix the turbulent velocity to the given fraction of the sound velocity.
  - *epslin* gives for LTE lines the fraction which is treated as thermal emission, while (1-*epslin*) gives the fraction which is treated as scattering. To get reasonable emission for M dwarfs *epslin*=0.1 is recommended. This is presumably wrong in the photosphere. It gives evidence to the problem, that pure thermal lines of oxygen and other elements are able to over-photoionise hydrogen. One way of diminishing the photoionising flux in these lines is to turn them into scattering lines, which are not coupled to the Planck function any more. The better way would be to compute only NLTE lines and no LTE lines at all (see also next point).
  - An alternative to the usage of *epslin* is not to include the atomic LTE background lines at all. If the computation time is available, try large NLTE sets and switch off the atomic LTE lines. This is most easily done by *touch fort.2* in the *dqs* file instead of linking the datafile with the atomic lines. Then an empty file is linked as atomic data file and no atomic lines are read, therefore any atomic line not computed in NLTE will be missing in the calculations and accordingly in the spectrum. Further on in the text NLTE sets will be recommended. The LTE molecular data is linked to *fort.1*. This should be unchanged if the star is cool enough to exhibit molecular lines.
  - *iter* should be at least 10. Although the temperature distribution is fixed and need not be converged, the NLTE level population does. Check the convergence of the resulting spectra (by printing out the spectra for each iteration) or at least of the departure coefficients.
  - *taulin* is recommended to be chosen very high (e. g. 1d300)
- Also, there are several useful atmospheric diagnostics possible in PHOENIX. These are not specific to chromospheric modelling, but have proven to be very useful for this topic. Some of them can be activated by PHOENIX parameters, others are contained in additional subroutines, that are not part of the normal PHOENIX package.
- *layerspec=t* will lead to an additional output file *.75* with the spectrum for every layer. This can be read with the IDL routine *read\_phoenix\_multi\_layer.pro*. Note that the given flux there is a net flux, i.e. the flux can be negative in the intermediate layers when the net flux is directed inwards.
  - The partial pressures will be printed out for *laus=2*. Since this produces a lot of output it can be used in conjunction with *hydstop=1*, which stops the computation after solving the hydrostatic equations.
  - Instead of the departure coefficients, the absolute population numbers can be printed out using the procedure *write\_ni.f*. This must be called in *MISC/restart\_file.f* instead of *write\_bi*. Do not forget to include *write\_ni.f* in the Makefile.
  - The *fort.19* file contains the atmospheric structure like the *fort.20* file, but for every iteration. This can be read by the IDL routine *read-fort19.pro*, which allows to look at the evolution during the iteration of the atmosphere. The hydrostatic variables normally converge very fast (typically two to three iterations), but the departure coefficients may not or may even oscillate.
- As mentioned above, the departure from NLTE is normally strong for M dwarfs and much less severe for solar like stars. For M dwarfs, calculating elements like C, N, and O in NLTE can alter the electron pressure and therefore influence the whole atmospheric structure (and the emergent spectrum). To get a rough impression of the resulting spectrum (and to spare computation time!) computing H, He and Na (if interested in the Na D lines) is normally sufficient. For a large NLTE set, the following species are additionally recommended: C I-IV,

O I-VIII, N I-VII, Fe I-IV, Ti I-II, and Mg I-III or Ni I-III. If the atmosphere is computed without the LTE background lines additionally also Si I-IV and S I-VI should be computed in NLTE (for chromospheric structures with *tmax\_top* less than 300000). If there is an interest in any He line shape always use the CHIANTI (or APED) database for He data, since the normal treatment in *phoenix* of He does not contain any multiplet structure. Any amplitude of a chromospheric emission line not computed in NLTE is most probably much too strong.

#### A.4 Output of various radiative transfer variables

Though the contribution function output is not directly related to chromospheric modelling, the line formation depth is an interesting parameter for chromospheric lines. Moreover, the output of the contribution functions and other useful radiative transfer variables has been programmed in the course of this work and is therefore described here.

The parameter *lfdo=t* will lead to additional line contribution function output using *fort.76*. The parameter *cntwl1* and *cntwl2* define the wavelength range for the output. The output contains the (monochromatic) source function, the Planck function and the intensity, as well as the intensity contribution function for the whole disc (flux contribution function) and for disc center ( $\mu = 1$ ) for different independent variables (standard optical depth, column mass and monochromatic optical depth). For each variable the *fort.76* file will give its name and then two blocks containing the wavelength followed by the values of the variable for each depth point up to layer 50 for the first block and from layer 50 to layer 100 for the second block. For computations where the number of layers differ from 100 the code has to be altered for  $50 > \textit{layer} > 150$ , since for  $\textit{layer} < 50$  the second output block is empty and for  $\textit{layer} > 150$  a third block is needed. The output cannot be written in one block for  $\textit{layer} > 50$  normally, due to the available memory capacity.

Source Monochromatic source function

Planck Monochromatic Planck function

J Monochromatic intensity

cntrbi Flux contribution function to be plotted vs log tstd

cntrbi1 Intensity contribution function for  $\mu = 1$  to be plotted vs log tstd

cntrbl Same as cntrbi1, but computed in a logarithmic way (useful for checking for numerical instabilities)

cntrcm Flux contribution function to be plotted vs log column mass

cntrcm1 Like cntrbi1, but to be plotted vs log column mass

cntrbt Flux contribution function to be plotted vs log tsum (see later) must be multiplied with  $tsum \cdot \ln(10)$

cntrbt1 Like cntrbi1, but to be plotted vs log tsum. To be multiplied with  $tsum \cdot \ln(10)$

tsum Monochromatic tau computed along the core intersecting ray with  $\mu = 1$  on the basis of extinction coefficients rather than absorption coefficients

cntrbi2 Intensity contribution function along a tangential ray. The ray should be located in the lower chromosphere. The depth point is addressed by the variable *cnti* in *S3R2T/cntrb.f*. This is hardcoded at the moment.

## Acknowledgements

I would like to thank a number of people for their contributions to this work and for making the time of my PhD unforgettable.

First of all I want to thank my supervisor Prof. Jürgen Schmitt who provided me with the subject and guided me throughout this work. With his readiness for discussions, his enthusiasm, and his ideas he was a constant source of motivation. Also I want to thank my second supervisor Prof. Peter Hauschildt who came in touch with me during the course of this thesis and inspired some essential parts of it. Of course I also want to thank him for the atmosphere code PHOENIX that taught me a lot about “real” programming.

The speciality of this thesis perhaps has been that I was in a way part of two work groups - which sometimes caused additional difficulties, but normally gave me a lot of pleasure. Therefore I am indebted to a lot of colleges. I thank my room-mates Marc Hempel and Christian Schröder for the many teatimes they shared with me. I owe Andreas Schweitzer for the introduction to the art of using PHOENIX and his patience, which he exercised to all my computer problems. To Jan Robrade, Uwe Wolter, and Alexander Petz I am grateful for the many discussions and help with all kind of problems. Sebastian Knop I thank for answering all my morning telephone calls for help with PHOENIX. Moreover I thank all my lunch mates and especially Matthias Dehn and Christine Johnas for their pleasant company. And if it were a person I would also thank Seneca for the reliable computation of my models.

I also thank all the other people from the Hamburger Sternwarte who made this work possible or helped to make the observatory such a special place. Moreover the Hamburger Sternwarte gave me the possibility to work for the Astronomie-Werkstatt, which made me interested and learn something about other astronomical subjects than related to this thesis.

I also would like to acknowledge the DAAD for funding my stay at the St. Mary’s University, Halifax, Canada. My work there was supervised by Prof. Ian Short, who managed to find time for numerous discussions and together with his wife, Katrin Jacob, helped me to settle down quickly in Halifax. I am expressing my gratitude to Julee Adams for finding me an accommodation and for her everlasting cheerfulness.

I thank Uwe Wolter, Marc Hempel, Jan Robrade, and Sebastian Knop for proof-reading parts of this thesis.

I am also indebted to all my friends, my parents and to my husband Lars.

I acknowledge financial support by the Deutsche Forschungsgemeinschaft under DFG SCHM 1032/16-1.